UNRAVELING MAGMATIC HISTORIES AT MULTIPLE SCALES

By

Blake Marshall Wallrich

Thesis

Submitted to the Faculty of the

Graduate School of Vanderbilt University

in partial fulfillment of the requirements

for the degree of

MASTERS OF SCIENCE

in

Earth and Environmental Science

August 09, 2019

Nashville, Tennessee

Approved

Calvin F. Miller, Ph.D.

Guilherme A.R. Gualda Ph.D.

DEDICATION

To Irene, for showing me that geology rocks and giving me the confidence and support to return to school and finish my undergraduate degree. Without you I would not be where I am today.

To William, for teaching me balance in my scientific endeavors. Without you (and Irene) I would be lost in a lab.

ACKNOWLEDGMENTS

I would like to thank my undergraduate advisor, Dr. Michael Zieg, for providing me with the tools, techniques, and advice I needed to become a the researcher I am today. I also have to thank Lily Claiborne for giving me the opportunity to participate in the Vanderbilt REU: Before and After a Supereruption, it was EPIC and greatly reinforced my decision to apply to graduate school. I would also like to thank Calvin Miller, you were a Rockstar in my mind prior to attending the REU and working with you has only reinforced that. I am eternally grateful for the guidance, life lessons, jokes, compassion, and research discussions you have provided over the past few years. You (and Molly) continue to set a standard for change in academia, from sharing a faculty position early on so that one of you could stay home with your children to supporting and mentoring your graduate students. I would also like to thank Guilherme Gualda for the research guidance, knowledge, push to get research published, and positive attitude! I thank all of the MESSY! group members for insightful and riveting paper discussions and Ramble sessions! I thank Vanderbilt University and the National Science Foundation for funding the research.

Lastly, I thank my family for being AWESOME!

TABLE OF CONTENTS

Page

LIST OF TABLES

LIST OF FIGURES

General Overview

To study volcanic-plutonic systems we must address the inherent problems with studying active volcanic systems. For example, sampling can be hazardous and limited to the surface leaving the plutonic component unaccounted for. Attempts to use geophysical methods to map plutonic systems is limited by resolution and thus the plutonic aspects of magmatic systems have been intensely debated for over a hundred years, largely from a petrologic/dynamics standpoint (Daly, 1911; Kaiser et al., 2017; Hildreth, 2004). At present, there is general agreement that most magmas are produced from partial melting of the mantle and crust, in varying proportions. During magma ascent, assimilation and crystallization processes modify the composition of the magma. This evolution is recorded in crystals, as compositional zoning and melt and mineral inclusions, and glass. However, few phases, taken alone, record all aspects of how late stage, near-eutectic-eutectic melts evolve and glass chemistry only records the final snapshot into the entire differentiation history.

In this study, we take a multi-faceted approach to better understand silicic magmatism. The broad questions that we were aiming to address include:

(1) How do magmatic systems and silicic magmas evolve through time?

(2) Can core to rim profiles in crystals provide insight into how late stage silicic melts evolve during the waning stages of magmatism?

To do this we investigated the post-supereruption silicic magmas within the epicenter of the giant Peach Spring Tuff supereruption and elemental partitioning in titanite.

1: TRACE ELEMENT PARTITIONING BETWEEN TITANITE (SPHENE) AND MELT

1.1 Introduction

Numerous investigations (Kohn, 2017 and references therein) have worked to constrain the conditions favorable for titanite crystallization (**Figure 1**). These studies clearly show that titanite saturation is favored in melts where the oxygen fugacity (fO_2) is relatively high (>Fayalite-Quartz-Magnetite (FMQ) buffer) and melt compositions are metaluminous to very slightly peraluminous. These conditions can generally be attained in two ways (1) through the generation of melts through processes such as flux (addition of water) melting such that oxidizing conditions are present, common in calc-alkaline magmas or (2) progressive crystallization of a low fO_2 magma causing a systematic increase in fO_2 with the crystallization of anhydrous phases such as feldspar, pyroxene, and olivine. This suggests that titanite saturation will become increasingly more favorable during late stage, near-eutectic conditions where the fO_2 is high, conditions are more oxidizing and melt compositions are metaluminous to very slightly peraluminous.

Investigations of silicic plutonic and volcanic rocks have demonstrated substantial effects of titanite on trace element geochemistry during melt evolution (e.g. Glazner and Coleman, 2008; Miller et al., 2009; Colombini et al., 2011; Colombini, 2009). Therefore, to better understand silicic melt geochemistry and the conditions and processes that it reveals we must better understand the influence of titanite crystallization on melt composition. To accomplish this we investigate titanite /melt elemental partitioning by collecting geochemical analyses of the titanite rims and coexisting glasses from a variety of different high silica rhyolite samples from

volcanic units within the Colorado River Extensional Corridor (CREC).

Titanite is an orthosilicate that occurs as a late–stage mineral in felsic calc–alkaline volcanics and plutons (Colombini et al., 2011; Frost et al., 2000). Its mineral structure consists of 3 distinct sites, a tetrahedral site with Si^{4+} as the main cation, an octahedral site with Ti^{4+} as the main cation, and a 7-fold decahedral site primarily occupied by Ca^{2+} (Deer et al., 1982; Kohn, 2017). In most titanite crystals, Si fills the tetrahedral site, but a variety of chemical substitutions can occur in the octahedral and decahedral sites. The chemical substitutions into the decahedral (Rare Earth Elements (REE's) U^{4+}, Th^{4+}, Pb^{4+} and other large ion lithophile element (LILE) substitutions) and octahedral sites (Al^{3+}, Fe^{3+}, Nb^{3+} and other high field strength elements) are controlled by the crystallization environment, notably temperature (Green and Pearson, 1986), and can provide a unique fingerprint of the crystallization process.

Previous research (e.g. Claiborne et al., 2017) has shown the important influence of temperature dependence on mineral/melt partition coefficients. Models for temperature dependence are based on calculated mineral/glass partition coefficients from a variety of magmatic environments. These models may allow the user to determine appropriate partition coefficients (Kd's) if an element or elements within the mineral phase of interest can provide a proxy for temperature (e.g. Ti-in-zircon). Application of these modeled Kd's permits estimation of the compositions of the evolving melts from which analyzed crystals grew. The modeled melt compositions are especially useful for elucidating the dispersed (trace) element abundances of late-stage, near-eutectic silicic melts, in which the essential (major) element compositions vary only slightly (Miller and Mittlefehldt, 1984), and for samples where direct evidence of melt compositions is no longer present (plutonic and detrital samples).

Titanite partition coefficients determined for multiple samples vary subtly, factor of ~2, in near-eutectic melts. However, previous research has demonstrated the correlation between elemental partitioning in titanite and temperature (Hayden et al., 2008; Green and Pearson, 1986). Therefore, regardless of the magnitude of Kd variability, titanite is an ideal candidate for testing the application of a temperature-based partition coefficient model. A titanite partition coefficient model would help to further elucidate the geochemical evolution of the melt, recorded within zoning profiles, over the narrow temperature window in which titanite crystallizes in near-invariant melts (Colombini et al., 2011).

In addition to small changes in temperature, parameters such as pressure, oxygen fugacity, and melt composition will be reflected in the modal abundance and composition of titanite (Frost et al., 2000). For example, igneous titanite is likely to be richer in REEs than secondary titanite, because REEs will be sequestered into accessory phases in the melt during igneous crystallization and are not likely to be remobilized during subsequent metamorphic reactions (Kowallis et al., 1997, 2018). Therefore, titanite grown in metamorphic and igneous temperature conditions is readily distinguishable for model calibration. Regardless of growth conditions, trace element concentrations within igneous titanite obey Henry's law and their concentrations are expected to vary in direct relation to melt composition. For these reasons, we attempt to show the applicability of titanite ($CaTiSiO_5$) as an additional, important recording device for a narrow, yet critically important, temperature window. When paired with other minerals-based models that allow equilibrium model melt to be determined, such as zircon and melt inclusions, these models help to further constrain the large geochemical changes occurring during near–eutectic magma evolution.

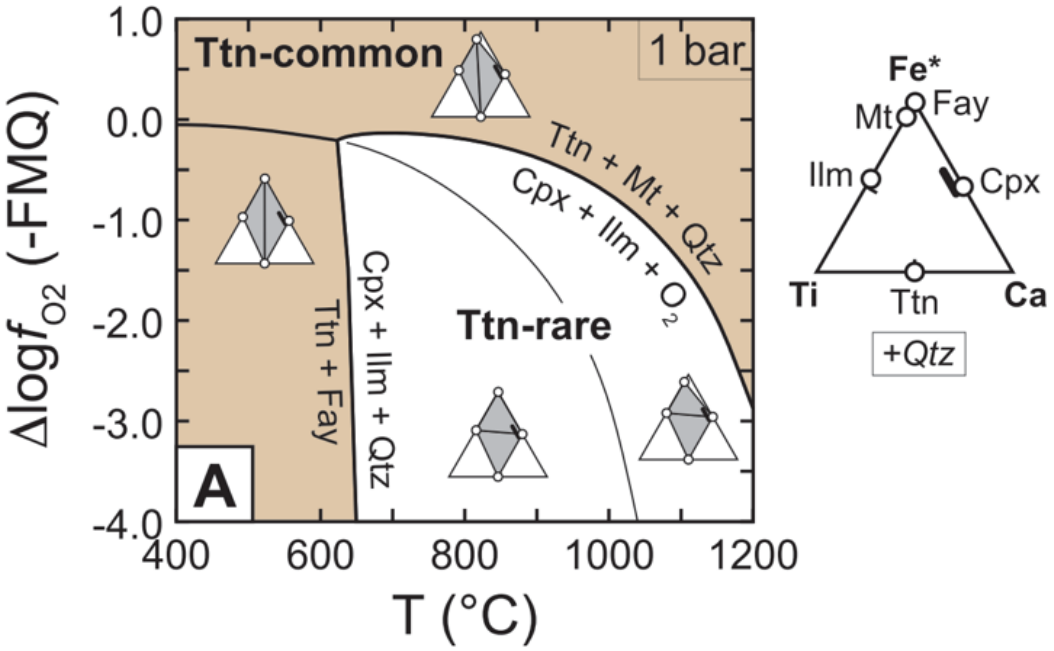

Figure 1: Phase equilibrium constraints on igneous titanite stability. (A) fO2 relative to fayalite–magnetite–quartz equilibrium vs. Temperature (ºC). Cpx = clinopyroxene, Fay = fayalite, Ilm = ilmenite, Mt = magnetite, Qtz = quartz, Ttn = titanite, Usp = ulvöspinel. The composition diagrams are projected from quartz and combine Fe^{2+} and Fe^{3+}. Small black bar spans typical igneous rock compositions. Modified from (Xirouchakis et al., 2001) Figure From Kohn (2017).

1.2 Background & Methods

Samples Used

We used titanite separates from and thin sections of high silica rhyolite (HSR) pumice and obsidian from four units from the Colorado River Extensional Corridor (CREC), AZ-NV (Peach Spring Tuff; Highland Range Lava (HRL-21); Sitgreaves Tuff unit 1 and Sitgreaves Tuff

unit 2). All samples contain HSR glass of metaluminous to slightly peraluminous composition (A/CNK= ~0.9-1.1). The Peach Spring Tuff (PST) sample (WSB-Fo-1) was collected from the uppermost unit (Tp5) of the PST section at Warm Springs Butte, AZ (Foley et al. in resivion). It includes two black, vitrophyric fiamme, one high silica rhyolite glass and the other with mingled low silica rhyolite and trachyte glasses; for this study, we focused on the titanite-bearing high silica glass fiamma. This sample, collected by Foley (2017), is interpreted to represent some of the last material erupted during the cataclysmic eruption. The phase assemblage of the PST high silica rhyolite includes sanidine, plagioclase, quartz, titanite, biotite, amphibole, Fe-Ti oxides, apatite, allanite, chevkinite, and zircon (Foley, 2017).

The Highland Range sample (HRL-21) is from an obsidian flow interbedded with high-silica rhyolite (HSR) tuffs within the Highland Range, northwest of Searchlight NV (Colombini et al., 2011). It is composed of green-gray color, glassy, crystal-poor obsidian and contains a phase assemblage of sanidine, plagioclase, quartz, titanite, biotite, Fe-Ti oxides, apatite, and zircon (Colombini et al., 2011). This sample was collected by Colombini et al. (2011) and has been interpreted, along with the upper silicic volcanic sequence at this locality, to represent late-stage, near eutectic melt generated during the waning stages of magmatism within the Searchlight Pluton (Padilla, 2011; Colombini, 2009; Colombini et al., 2011; Bachl et al., 2001; Bazar et al., 2006).

The two samples from the Sitgreaves Tuff (SGT-1 and SGT-2) are from stacked paleo-valley fill ignimbrites to the north of Oatman AZ in the Southern Black Mountains. SGT-1 samples are composed of high-silica rhyolite (HSR) pumice glass and contain a phase assemblage of sanidine, plagioclase, quartz, biotite, amphibole, apatite, zircon, titanite, and Fe-Ti

oxides. SGT-2 samples are composed of crystal-poor HSR pumice and contain sanidine, quartz, amphibole, biotite (trace), Fe-Ti oxides, titanite, zircon, apatite, and chevkinite. SGT-2 glass is the most chemically evolved sample in this study. These two samples were collected and used in two previous studies (Wallrich et al., 2016, 2018) and are interpreted to represent a dynamic, constantly changing magmatic system during the waning stages of magmatism within the Southern Black Mountain Volcanic Center (Wallrich et al., 2018; Foley, 2017; Pamukcu et al., 2013; Frazier, 2013).

Previous studies (Pamukcu et al., 2015; Foley, 2017; Colombini et al., 2011; Wallrich et al., 2016, 2018) have noted that phenocrysts within the HSR samples used in this study are typically euhedral, and show few signs of resorption, making these samples ideal choices to study elemental partitioning between titanite and melt. For all samples, glass analyses were re-collected using the methods detailed below.

Sample Preparation

Crystal separates were obtained for the pumiceous samples (SGT-1 and SGT-2) by extracting individual pumice from the tuffaceous host rock followed by lightly crushing, with a baseball bat, and sieving. The crystals were separated using different size sieves. Each size fraction was then winnowed by water to concentrate the minerals relative to ash. The crystal separates were then hand-picked under a stereomicroscope. Crystals with adhering glass, suggesting crystal-melt equilibrium, were mounted in epoxy for further analysis. All mounts were polished using a Buehler EcoMet polisher and checked for a smooth surface and cross sectional grain exposure using a Leica petrographic microscope equipped with reflected light

capabilities at Vanderbilt University.

For all samples, thin sections were also used for glass and titanite analysis. This served two purposes: (1) preserving whole-euhedral titanite phenocrysts and (2) providing more context of the phase relations within each sample (clumping or no clumping of accessory minerals) (Pamukcu et al., 2013). Grains that did not appear to be oriented parallel to the {111} face were not considered for use in this project due to the anomalous affinity of titanite for trace elements outside of the {111} sector (**Figure 2**)(Hayden et al., 2008; Kohn, 2017).

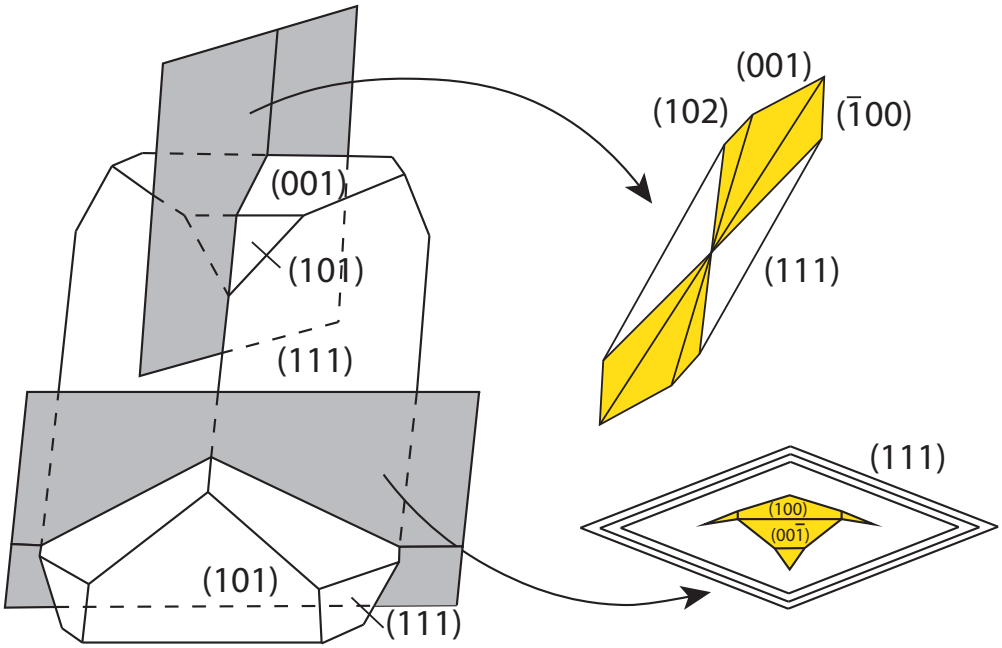

Figure 2: Titanite crystal schematic. Typical crystal showing dominant {111} faces with minor faces along other directions. Expected patterns of sector zoning (darker vs. lighter shading) are illustrated for transverse {111} vs. longitudinal sections {1̄00}. Transverse sections were targeted for the calibration of the partition coefficient model developed in this study. Modified from Patterson et al. 1992

Scanning Electron Microscope (SEM)

Energy dispersive spectroscopy (EDS) analysis using a LaB_6 filament in a Tescan Vega 3

LM variable pressure SEM equipped with an Oxford X-max 50 mm^2 EDS system was conducted at Vanderbilt University. HSR glass fused from USGS standard RGM-1 was run daily to check the analytical consistency of the SEM. An SPI #02753-AB mineral standard was run periodically to check the accuracy of the results on various minerals. Quantitative EDS analyses were collected for major elements within the rim, intermediate and core zones of crystals. During these analyses the sample working distance was maintained at 15 mm, an electron beam acceleration of 15 kV and maximum beam intensity of 19 were used, resulting in absorbed currents of ~10 nA. Aztec processing software, developed by Oxford, was used for data acquisition and processing. Precision and accuracy of SEM-EDS measurements are discussed by Pamukcu et al. (2015). Grain characteristics such as zoning, crystal shape, and orientation in each grain were documented for LA-ICPMS analysis.

Laser Ablation-Inductively Coupled Plasma Mass Spectrometry

Analysis

We determined concentrations of dispersed elements in glass and minerals by LA-ICPMS using a Photon Machines Excite Laser Ablation unit connected to a Thermo iCAP Q ICPMS installed at Vanderbilt University. A minimum number of analytes was chosen for data collection to increase the counting time per element. BSE images were used to check for proper ablation profile orientation. We set the laser settings to yield a fluence of 4.8-5.0 $\frac{J}{cm^2}$, at a repetition rate of 15 Hz, with He (0.9 min−1) as the carrier gas. Each analysis (individual spot and line of spots) began with 30 s of blank acquisition, followed by 60 s of ablation and 30 s of wash-out time to

allow the measured values to return to blank levels.

We measured a total of 36 analytes during each analysis. For every 15 measurements of

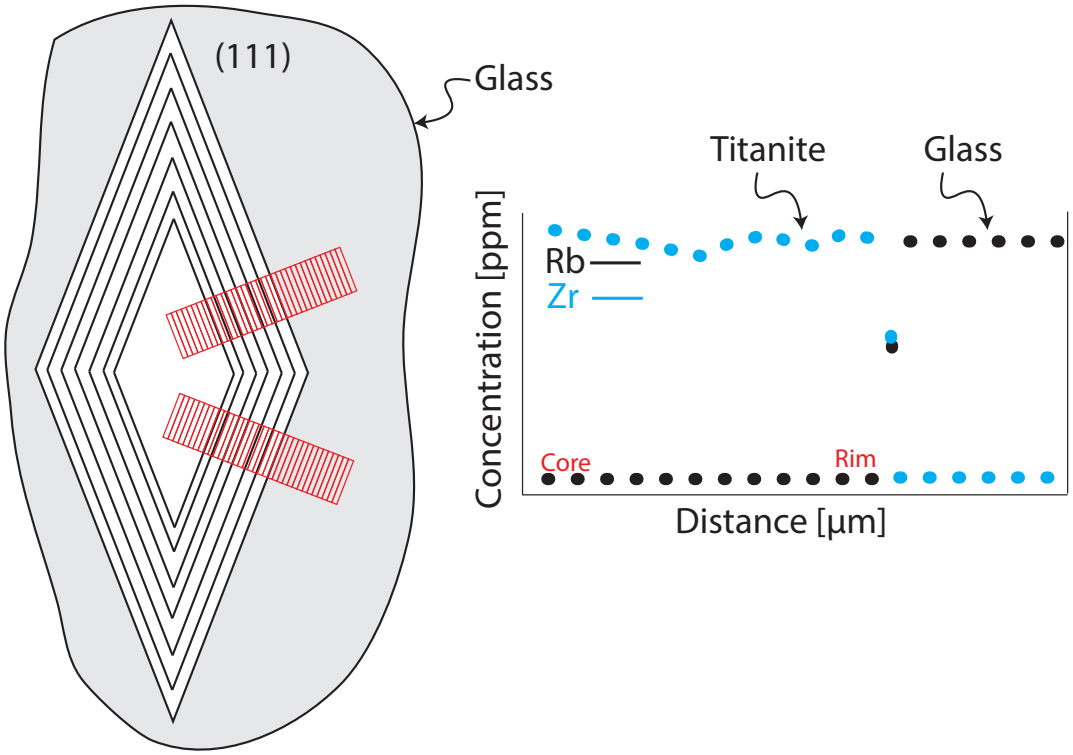

Figure 3: Schematic diagram illustrating the ablation method used to determine partition coefficients. Ablation method in a chemically zoned titanite section {111} in glass (gray) with ablation profiles using a 7 x 50 µm spot starting in matrix glass and proceeding to the core of the crystal. Sharp change in elemental concentration mark the transition from glass to crystal rim. In some instances there are intermediate concentrations (as shown) which we interpret to be a mixture of glass and titanite. If present we choose the next spot as the titanite rim value.

unknowns for individual spots and every individual line of spots, we analyzed primary (for calibration) and secondary (treated as unknowns) standards to evaluate the precision and accuracy of the results. We used NIST 610 as the primary standard and NIST 612, NIST 614 (Pearce et al., 1997), and USGS reference material RGM-1 glasses as the secondary standards. We chose ^{28}Si as the internal standard for glass and minerals.

For individual spot analysis in glass, we used a spot size of 50 x 50 µm. For all mineral

phases a line of spots, each spot 7 x 50 µm, was initiated within the glass and run to the core of the phenocryst (**Figure 3** and **Figure 4**). This method allowed for higher spatial resolution and

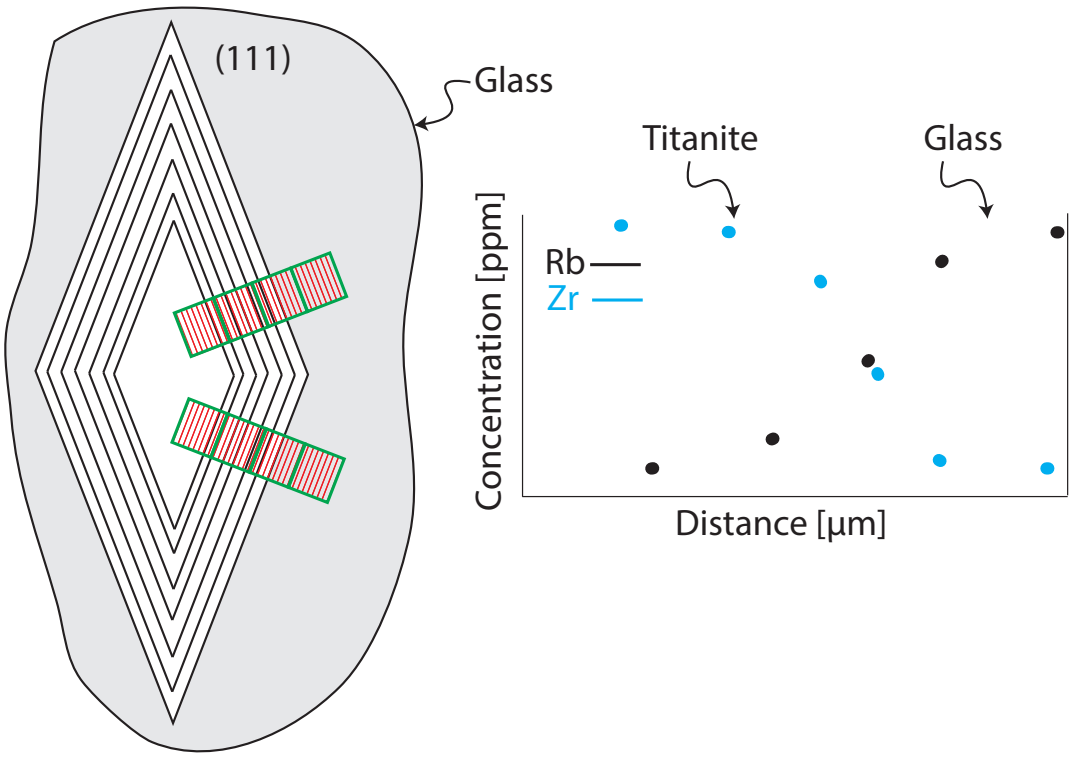

Figure 4: Schematic diagram illustrating the use of square ablation spots. Ablation using equant (i.e. squares or circles) through a chemically zoned titanite section {111} in glass (gray) with ablation profiles using a 50 x 50 µm line of spots (Green boxes) starting in matrix glass and proceeding to the core of the crystal. Smaller red rectangles are 7 x 50 µm spots for comparison (Fig. 2).

analysis much closer to the rim to be collected as the concentrations of characteristic elements (e.g. Zr, Middle-REE, Y) are elevated in titanite with respect to glass. This procedure was performed over multiple grains and rims from each sample to produce an average value. This increased resolution also yields a more detailed record of melt evolution stored within the titanite phenocrysts to be resolved on a core to rim transect.

Data Reduction

We used Glitter (Griffin, 2008) to reduce the LA-ICPMS spot data and LaserTRAM

(Loewen and Kent, 2012) to reduce the line of spots data. Each analysis was checked for the possibility of contamination (e.g. mineral or melt inclusion) by using a combination of essential and dispersed structural constituents (**Figure 3**). The majority of elements in the glass were much lower than the concentrations measured in titanite; this facilitated identification of the first laser spot to intersect the titanite rim, thus allowing for compositions at, or very near the rim (+/- 7 um), to be identified (**Figure 3**). All rim data for each analyte were reviewed to identify and remove individual outlier analyses that deviated from the average by 2σ or greater (which typically modified the relative error by >5%). We then averaged remaining values to yield our best value for the concentration of each trace element in each sample population to produce the Onuma diagrams and partition coefficient values listed below.

Average partition coefficients (Kd, equation 1) were calculated for each element by dividing the average element concentration in titanite rims (**Table 2**) by the average concentration of that element in the glass (**Table 1**). The Kd model regressions (**Figure 10**, **Figure 11, Figure 12**) include all average Kd value plotted against the average value of Zr within the titanite rims. The concentrations used for partition coefficient calculation correspond to average rim compositions of 9 to 13 total analyses (See **Table 1** and **Table 2**).

$$Kd = \frac{Concentration_{Solid}}{Concentration_{Liquid}} \quad (1)$$

1.3 Results

We compare REE data from this study to the previously published values for PST and HRL-21 high silica rhyolite samples (Padilla and Gualda, 2016; Colombini et al., 2011) (**Figure 5**). The elemental concentrations in glass and titanite, compiled in this study are consistent with

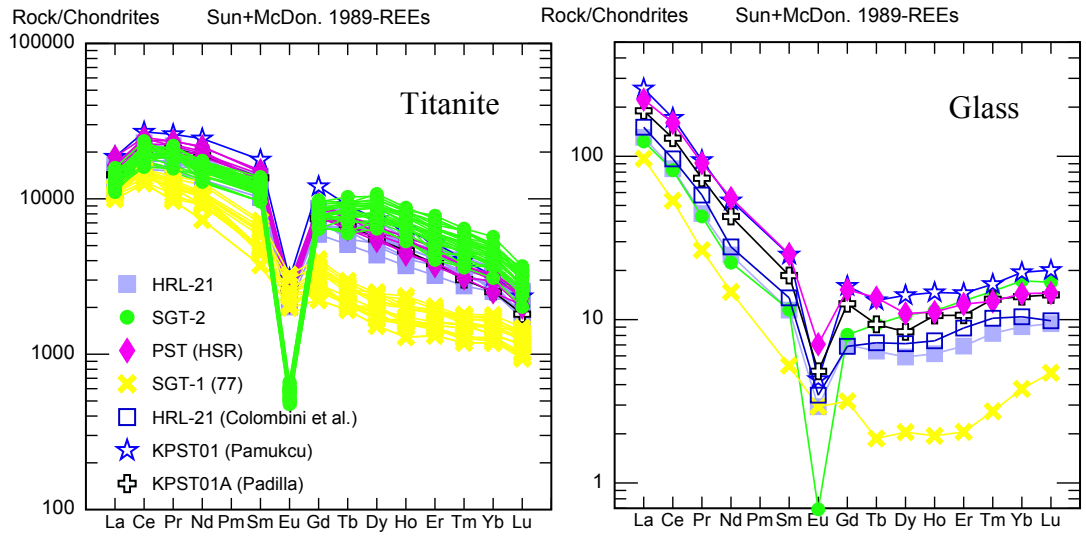

Figure 5: REE plots for coexisting glass and titanite rims. (Left) Titanite rim REE patterns from this study and those reported by Colombini et al. (2011) and Padilla & Gualda (2016). (Right) Measured REE in glass from all four high-silica, titanite-bearing rhyolites, including the glass REE values published by Colombini et al. 2011 and Padilla & Gualda (2016).

the previously published data (**Figure 5**). The middle REE's (MREE) are highly concentrated in titanite with respect to the heavy and light REE's. Values for europium (Eu) are typically much lower than the adjacent MREE. Al^{3+} and Fe^{T} cations per formula unit are consistent with the titanite being igneous in origin (**Figure 6**, Kowallis et al., 1997, 2018).

Although the values are comparable with previous studies we have chosen to use only values produced using the strict collection protocol described above.

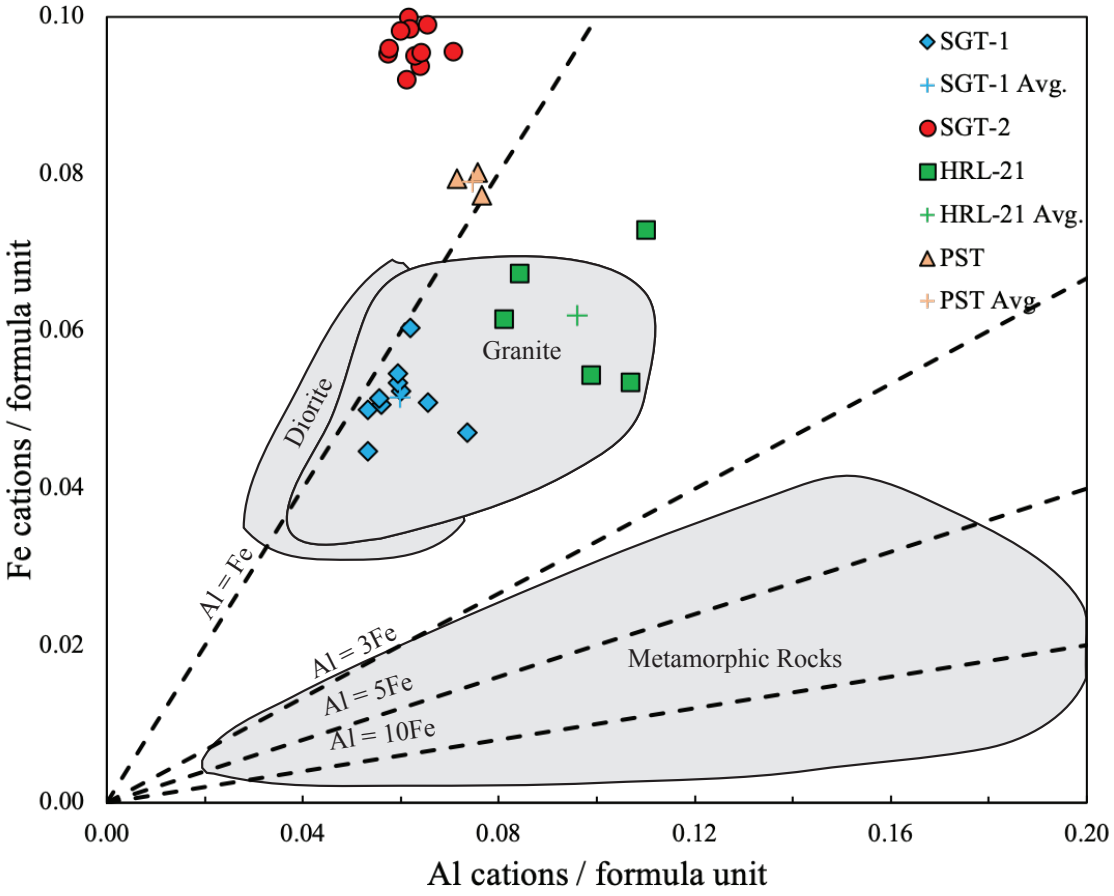

Figure 6: Plot of Fe vs Al (CPFU) in titanite rims. Discrimination diagram showing the variation in chemical composition between metamorphic and igneous titanite using the fields from Kowallis et al. (1997). All titanite from this study plot within the igneous region. Formula recalculation was done using data obtained via SEM-EDS, 3 cation sum.

Table 1: Average composition of glass from the four sampled units. Major oxides were collected using SEM-EDS. Trace elements were collected using LA-ICPMS. 8 to 46 analyses per sample. Trace elements obtained via LA-ICPMS. SD = Standard deviation, RD = Relative deviation.

	HRL-21			**SGT-1**		
Element	Average	SD	RD	Average	SD	RD
SiO_2	77.02	0.15	0.00	77.57	0.77	0.01
TiO_2	0.10	0.06	0.59	0.10	0.07	0.72
Al_2O_3	12.75	0.08	0.01	12.74	0.53	0.04
FeO	0.62	0.07	0.11	0.71	0.30	0.42
MnO	0.05	0.05	1.09	0.01	0.03	2.44
MgO	0.06	0.03	0.53	0.07	0.06	0.80
CaO	0.52	0.06	0.11	0.65	0.22	0.35
Na_2O	3.47	0.39	0.11	2.66	0.19	0.07
K_2O	5.40	0.49	0.09	5.49	0.32	0.06
Total	100.00	–	–	100.00	–	–
Rb	174.63	10.26	0.06	203.10	20.37	0.10
Sr	11.68	0.45	0.04	102.67	23.22	0.23
Y	11.49	0.43	0.04	4.07	1.50	0.37
Zr	73.76	2.15	0.03	69.86	14.91	0.21
Nb	23.28	0.69	0.03	10.36	1.38	0.13
Ba	16.74	0.59	0.04	215.99	58.74	0.27
La	30.95	0.89	0.03	23.23	5.74	0.25
Ce	51.35	1.67	0.03	33.13	10.14	0.31
Pr	4.24	0.17	0.04	2.65	1.04	0.39
Nd	11.62	0.70	0.06	7.52	3.49	0.46
Sm	1.75	0.28	0.16	0.84	0.47	0.56
Eu	0.17	0.05	0.27	0.18	0.06	0.35
Gd	1.44	0.27	0.19	0.68	0.35	0.52
Tb	0.24	0.04	0.17	0.07	0.03	0.45
Gd	1.30	0.16	0.12	0.54	0.25	0.46
Dy	1.50	0.18	0.12	0.53	0.24	0.44
Ho	0.35	0.05	0.14	0.11	0.06	0.53
Er	1.14	0.13	0.11	0.36	0.12	0.34
Tm	0.21	0.03	0.16	0.07	0.03	0.35
Yb	1.54	0.19	0.12	0.67	0.19	0.29

Lu	0.24	0.04	0.16	0.12	0.03	0.25
Hf	3.01	0.33	0.11	2.43	0.47	0.19
Th	21.21	0.64	0.03	19.60	2.79	0.14
U	4.76	0.18	0.04	4.22	0.59	0.14

Table 1 Continued:

	SGT-2			**PST (HSR)**		
Element	Average	SD	RD	Average	SD	RD
SiO_2	77.37	0.25	0.00	76.30	0.21	0.00
TiO_2	0.08	0.05	0.68	0.30	0.12	0.39
Al_2O_3	12.45	0.14	0.01	12.94	0.04	0.00
FeO	0.69	0.10	0.14	0.31	0.06	0.20
MnO	0.07	0.06	0.84	0.03	0.05	1.51
MgO	0.03	0.03	0.87	0.03	0.02	0.89
CaO	0.36	0.05	0.14	0.34	0.08	0.23
Na_2O	2.80	0.23	0.08	2.56	0.15	0.06
K_2O	6.14	0.23	0.04	7.18	0.10	0.01
Total	100.00	–	–	100.00	–	–
Rb	396.54	70.84	0.18	192.27	6.81	0.04
Sr	3.51	5.65	1.61	31.76	4.67	0.15
Y	23.20	1.20	0.05	20.03	1.29	0.06
Zr	117.34	5.52	0.05	152.78	32.43	0.21
Nb	47.86	2.20	0.05	32.19	1.03	0.03
Ba	1.82	2.57	1.41	271.51	34.03	0.13
La	29.64	1.29	0.04	52.67	9.61	0.18
Ce	51.44	2.20	0.04	98.14	19.1	0.19
Pr	4.18	0.28	0.07	8.63	2.1	0.24
Nd	10.49	0.87	0.08	25.92	6.87	0.27
Sm	1.83	0.22	0.12	3.85	1.18	0.31
Eu	0.04	0.02	0.43	0.41	0.2	0.47
Gd	1.76	0.30	0.17	3.13	0.74	0.24
Tb	0.36	0.04	0.12	0.51	0.09	0.19
Gd	1.70	0.18	0.10	2.61	0.68	0.26
Dy	2.59	0.22	0.08	2.77	0.42	0.15
Ho	0.65	0.08	0.12	0.63	0.1	0.16
Er	2.21	0.16	0.07	2.06	0.27	0.13
Tm	0.37	0.05	0.12	0.33	0.05	0.14
Yb	2.96	0.28	0.10	2.45	0.27	0.11

Lu	0.45	0.05	0.11	0.37	0.06	0.16
Hf	5.80	0.42	0.07	5.64	0.63	0.11
Th	30.76	1.55	0.05	28.59	0.96	0.03
U	6.04	0.26	0.04	6.1	0.34	0.06

Table 2: Average composition of titanite rim from the four sampled units. N = 9 to 13 analyses per sample. Major elements obtained via SEM-EDS. Trace elements obtained via LA-ICPMS. SD = Standard deviation, RD = Relative deviation.

	HRL-21			**SGT-1**		
Element	Average	SD	RD	Average	SD	RD
SiO_2	34.65	–	–	32.24	–	–
TiO_2	34.04	–	–	36.88	–	–
Al_2O_3	2.74	–	–	1.60	–	–
FeO	2.51	–	–	1.80	–	–
MnO	0.13	–	–	0.14	–	–
MgO	0.02	–	–	0.04	–	–
CaO	25.33	–	–	27.10	–	–
Na_2O	0.19	–	–	0.06	–	–
K_2O	0.38	–	–	0.14	–	–
Rb	5.34	4.60	0.86	1.94	1.02	0.52
Sr	9.94	1.92	0.19	36.31	3.89	0.11
Y	579.16	74.47	0.13	243.11	33.58	0.14
Zr	782.65	71.44	0.09	491.20	28.64	0.06
Nb	2472.75	419.60	0.17	1483.81	138.55	0.09
Ba	38.10	5.48	0.14	36.17	4.82	0.13
La	3821.86	461.56	0.12	2657.86	171.58	0.06
Ce	12962.47	1653.01	0.13	9089.90	637.80	0.07
Pr	1922.93	244.80	0.13	1132.10	130.65	0.12
Nd	8315.87	864.92	0.10	4785.68	708.09	0.15
Sm	1994.02	197.45	0.10	808.34	174.48	0.22
Eu	151.64	18.83	0.12	142.68	26.49	0.19
Gd	1658.07	203.24	0.12	616.12	129.55	0.21
Tb	271.45	39.87	0.15	86.72	13.68	0.16
Gd	1658.07	203.24	0.12	616.12	129.55	0.21
Dy	1580.30	221.12	0.14	499.93	88.58	0.18
Ho	297.63	31.77	0.11	98.30	19.38	0.20
Er	754.49	92.75	0.12	274.42	40.05	0.15

Tm	97.25	13.54	0.14	38.06	5.23	0.14
Yb	579.16	74.47	0.13	243.11	33.58	0.14
Lu	58.97	8.53	0.14	29.72	3.79	0.13
Hf	69.00	10.21	0.15	34.69	3.63	0.10
Th	–	–	–	351.25	23.27	0.07
U	–	–	–	34.49	3.21	0.09

Table 2 Continued:

	SGT-2			**PST (HSR)**		
Element	Average	SD	RD	Average	SD	RD
SiO_2	31.48	–	–	32.46	–	–
TiO_2	36.08	–	–	35.57	–	–
Al_2O_3	1.51	–	–	2.17	–	–
FeO	3.35	–	–	2.93	–	–
MnO	0.43	–	–	0.27	–	–
MgO	0.04	–	–	0.11	–	–
CaO	27.02	–	–	26.07	–	–
Na_2O	0.08	–	–	0.16	–	–
K_2O	0	–	–	0.25	–	–
Rb	1.06	0.55	0.52	0.93	0.53	0.57
Sr	0.54	0.34	0.63	3.46	1.11	0.32
Y	747.94	100.39	0.13	521.55	66.26	0.13
Zr	827.48	108.95	0.13	1095.46	121.59	0.11
Nb	4151.98	562.82	0.14	2268.38	416.78	0.18
Ba	40.87	2.87	0.07	49.30	3.54	0.07
La	3142.57	310.19	0.10	3746.71	424.21	0.11
Ce	12057.11	1067.98	0.09	13707.95	917.63	0.07
Pr	1836.65	130.71	0.07	2113.34	206.98	0.10
Nd	7286.94	619.43	0.09	9718.50	1358.34	0.14
Sm	1808.95	170.27	0.09	2413.95	783.61	0.32
Eu	33.11	3.04	0.09	149.39	23.62	0.16
Gd	1655.73	195.65	0.12	2021.32	775.96	0.38
Tb	315.85	40.44	0.13	312.81	132.30	0.42
Gd	1655.73	195.65	0.12	2021.32	775.96	0.38
Dy	2160.19	308.18	0.14	1814.01	724.06	0.40
Ho	409.83	54.49	0.13	332.10	108.81	0.33
Er	983.92	164.82	0.17	802.19	218.06	0.27
Tm	130.39	20.49	0.16	94.96	19.55	0.21

Yb	747.94	100.39	0.13	521.55	66.26	0.13
Lu	76.30	10.95	0.14	57.44	5.22	0.09
Hf	76.86	13.03	0.17	78.07	7.78	0.10
Th	276.29	38.13	0.14	291.72	60.41	0.21
U	18.45	1.96	0.11	22.78	4.48	0.20

Table 3: Average partition coefficients (Kd) for the four samples used in this study

	HRL-21			**SGT-1**		
Element	Average	SD	RD	Average	SD	RD
SiO_2	0.43	0.02	0.04	0.41	0.01	0.02
TiO_2	377.89	40.45	0.11	425.24	39.41	0.09
Al_2O_3	0.20	0.03	0.16	0.13	0.01	0.11
FeO	5.25	0.42	0.08	3.04	0.25	0.08
MgO	1.01	0.10	0.10	0.14	0.02	0.18
CaO	70.41	7.67	0.11	33.03	4.25	0.13
Rb	0.03	0.03	0.86	0.01	0.01	0.52
Sr	0.85	0.16	0.19	0.35	0.04	0.11
Y	663.89	76.89	0.12	597.22	110.18	0.18
Zr	10.61	0.97	0.09	7.03	0.41	0.06
Nb	106.23	18.03	0.17	143.17	13.37	0.09
Ba	2.28	0.33	0.14	0.17	0.02	0.13
La	123.47	14.91	0.12	114.43	7.39	0.06
Ce	252.45	32.19	0.13	274.37	19.25	0.07
Pr	453.88	57.78	0.13	426.64	49.24	0.12
Nd	715.42	74.41	0.10	636.64	94.20	0.15
Sm	1140.02	112.89	0.10	964.33	208.15	0.22
Eu	910.34	113.04	0.12	799.05	148.38	0.19
Gd	1148.25	140.75	0.12	906.14	190.53	0.21
Tb	1121.79	164.77	0.15	1324.63	208.97	0.16
Dy	1051.82	147.17	0.14	938.38	166.27	0.18
Ho	839.14	89.56	0.11	935.68	184.49	0.20
Er	664.30	81.67	0.12	763.03	111.35	0.15
Tm	473.73	65.95	0.14	508.71	69.88	0.14
Yb	375.10	48.23	0.13	362.54	50.07	0.14
Lu	247.52	35.79	0.14	247.17	31.52	0.13
Hf	22.89	3.39	0.15	14.26	1.49	0.10
Th	–	–	–	17.92	1.19	0.07

U	–	–	–	8.17	0.76	0.09

Table 3 Continued.

	SGT-2			PST (HSR)		
Element	Average	SD	RD	Average	SD	RD
SiO_2	0.40	0.00	0.00	0.40	0.00	0.01
TiO_2	460.62	37.42	0.08	218.82	17.92	0.08
Al_2O_3	0.16	0.02	0.10	0.16	0.01	0.07
FeO	4.59	0.57	0.12	4.76	0.33	0.07
MgO	0.81	0.08	0.10	–	–	–
CaO	84.18	7.45	0.09	80.86	5.86	0.07
Rb	0.00	0.00	0.52	0.00	0.00	0.57
Sr	0.15	0.10	0.63	0.11	0.03	0.32
Y	484.06	65.14	0.13	389.73	93.53	0.24
Zr	7.05	0.93	0.13	7.17	0.80	0.11
Nb	86.75	11.76	0.14	70.47	12.95	0.18
Ba	22.41	1.57	0.07	0.18	0.01	0.07
La	106.01	10.46	0.10	71.14	8.05	0.11
Ce	234.39	20.76	0.09	139.68	9.35	0.07
Pr	439.20	31.26	0.07	244.88	23.98	0.10
Nd	694.52	59.04	0.09	374.94	52.41	0.14
Sm	990.30	93.21	0.09	627.00	203.53	0.32
Eu	856.55	78.61	0.09	364.38	57.60	0.16
Gd	938.98	110.96	0.12	645.79	247.91	0.38
Tb	868.01	111.13	0.13	613.35	259.41	0.42
Dy	834.83	119.10	0.14	654.88	261.39	0.40
Ho	627.39	83.42	0.13	527.15	172.71	0.33
Er	445.76	74.67	0.17	389.41	105.85	0.27
Tm	353.79	55.60	0.16	287.75	59.24	0.21
Yb	253.10	33.97	0.13	212.88	27.04	0.13
Lu	167.86	24.10	0.14	155.25	14.12	0.09
Hf	13.25	2.25	0.17	13.84	1.38	0.10
Th	8.98	1.24	0.14	10.20	2.11	0.21
U	3.06	0.32	0.11	3.73	0.73	0.20

Crystallographic Controls on Elemental Partitioning

We interpret the partition coefficients for titanite in light of the theoretical considerations of crystal lattice strain theory described by Brice (1975) and Blundy and Wood (1994, 2003). These studies have shown that the exchange of cations at particular sites within a crystal will conform to a parabola-like function due to the mismatch in size and valence state between the cations and the site. Using the method of (Padilla and Gualda, 2016), we fit our data to a function in the form of $y = ax^3 + bx^2 + c$, where y represents Kd in log space (e.g. ln[Kd]) and x is a term that includes the ionic radius (using values of Shannon (1976)); we use a least squares difference method in Microsoft Excel to perform the fitting. The results are plotted on Onuma diagrams (Onuma et al., 1968) in order to assess how groups of elements partition into various sites within each mineral **(Figure 7**). This type of analysis clearly demonstrates the crystallographic controls on elemental partitioning in titanite, and it constitutes an effective test of the quality of the Kd values presented here.

We focus on the REE elements because of their importance in petrochemical studies and their generally similar and monotonically varying characteristics (generally trivalent with ionic radii that decrease continuously increasing with atomic number). All REE's in titanite except for Eu conform to the Onuma curve well (**Figure 7**). Eu shows a notably lower Kd value than that predicted by the Onuma curve because, unlike the other REE, a substantial fraction is not trivalent, and Eu^{2+} is much less compatible with titanite than trivalent MREE. For this reason Eu was not included in the calculation of the Kd model fit (Padilla and Gualda, 2016; Colombini et

al., 2011).

The results also demonstrate the limited range in titanite Kds for each REE (approximately a factor of two) among our four metaluminous-peraluminous HSR samples. The limited range means that, even though the Zr (~temperature) correction is significant, it is quite modest, and over the range of conditions assessed here uncertainty in the correction will not

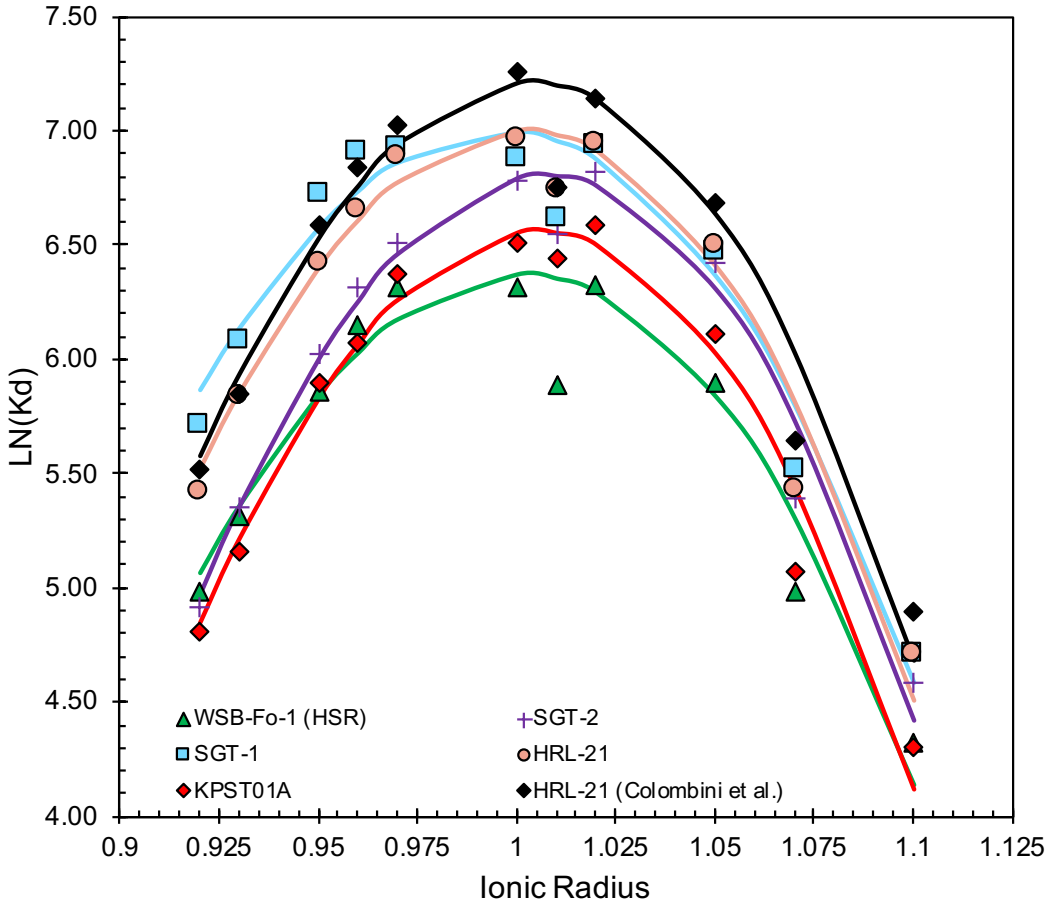

Figure 7: Onuma Curves for all four high-silica, titanite-bearing rhyolites used in this study, along with the model fits derived in the Colombini et al. (2011) and Padilla & Gualda (2016). Symbols represent measured values; all REE elements (La through Lu) except Eu were used in the fitting procedure.

preclude effective use of our Kds.

1.4 Discussion

Zr-in-Titanite Partitioning

Previous studies (e.g. Colombini et al., 2011; Bachmann et al., 2005a) have shown that the REE's and some other trace elements have a high affinity to partition into titanite. The results of this study further solidify this observation. Mechanisms for substitutions into titanite have been proposed by multiple studies and include those in **Table 4**.

Table 4: Site specific and coupled substitutions in titanite (Sahama, 1946; Jaffe, 1947; Kohn, 2017; Paterson and Stephens, 1992; Smith, 1970; Coombs et al., 1976; Higgins, John B., Ribbe, 1976; Deer et al., 1982; Piccoli et al., 2000; Hayden et al. 2008).

Site	Substituting Elements
Ti^{4+}	Zr^{4+}, Mg^{2+}, Al^{3+}, Fe^{3+}, Fe^{2+}, V^{5+}, Cr^{3+}, Nb^{5+}, Ta^{5+}
Ca^{2+}	Na^{+}, Sr^{2+}, Mn^{2+}, Ba^{2+}, REE^{3+}
Si^{4+}	Al^{3+}
O^{2-}	OH^{-}, F^{-}, Cl^{-}
$2Ti^{4+}$	$(Al^{3+}, Fe^{3+}) + (Nb^{5+}, Ta^{5+})$
$Ti^{4+} + O^{2-}$	$(Al^{3+}, Fe^{3+}) + (OH^{-},F^{-})$
$Ca^{2+} + Ti^{4+}$	$Na^{+} + (Nb^{5+}, Ta^{5+})$ $(REE^{3+}, Y^{3+}) + (Al^{3+}, Fe^{3+})$

Hayden et al. (2008) demonstrated that the temperature of a magma during growth of titanite is related to the amount of Zr^{4+} that substitutes into the mineral structure for Ti^{4+}. This temperature-Zr relationship was calibrated using the {111} zone chemistry; thus, the analyses from this study are ideal for application of the Zr-in-titanite thermometer, allowing for the investigation of the relationship of partitioning and temperature in titanite. The temperature dependence of titanite and Zr^{4+} concentration takes the form of (Hayden et al., 2008):

$$\mathrm{T(°C)} = \frac{7708 + 960P}{10.52 - \log(\alpha \mathrm{TiO_2}) - \log(\alpha \mathrm{SiO_2}) - \log(\mathrm{ppm}\ Zr^{titanite})} - 273 \qquad \mathbf{2}$$

where the elemental substitution is dependent on the activities of TiO_2 and SiO_2, pressure, and temperature. Therefore, if we can constrain the pressure of crystallization we can estimate the temperature of crystallization.

Table 5: Results of Zr-in-titanite thermometry and zircon saturation thermometry (Watson and Harrison, 1983; Boehnke et al., 2013). Pressures are the average values from published literature. Zircon saturation temperatures were determined using glass data compiled in this study.

	HRL-21			**SGT-1**		
	Average	SD	RD	Average	SD	RD
Zr-Glass	74	2	0.03	70	15	0.21
Zr-Ttn-Rim	783	71	0.09	491	29	0.06
$T_{Zr\text{-}Ttn}$ (ºC)	736	5	0.007	716	3	0.004
$T_{Zr\text{-}Sat}$ (W&H)	729	–	–	733	–	–
$T_{Zr\text{-}Sat}$ (B)	670	–	–	678	–	–
Pressure (MPa)		150			200	
Reference		Bachl et al. 2001, this study			Wallrich et al. 2018, chapter 2 this thesis	

Table 5 continued.

	SGT-2			**PST (HSR)**		
Element	Average	SD	RD	Average	SD	RD
Zr-Glass	117	6	0.05	153	32	0.21
Zr-Ttn-Rim	827	109	0.13	1095	122	0.11
$T_{Zr\text{-}Ttn}$ (ºC)	745	8	0.01	763	7	0.01
$T_{Zr\text{-}Sat}$ (W&H)	769	–	–	789	–	–
$T_{Zr\text{-}Sat}$ (B)	717	–	–	738	–	–
Pressure (MPa)		200			212	
Reference		Wallrich et al. 2018, chapter 2 this thesis			Pamukcu et al. (2015)	

Crystallization pressures of the samples used in this study have been constrained by

previous studies (Bachl et al., 2001; Pamukcu et al., 2015; Wallrich et al., 2018). The estimated pressures were constrained by applying multiple geobarometric methods, including, multiple different Al-in-amphibole calibrations (Mutch et al., 2016) and Rhyolite MELTS geobarometer (Gualda and Ghiorso, 2014; Gualda et al., 2012). The use of multiple methods for constraining pressure has resulted in tightly constrained estimates of ≤50 MPa for each sample.

Using the published best estimate pressure values, we applied the Hayden et al., (2008) Zr-in-titanite geothermometer to estimate the temperature of crystallization recorded by titanite rim growth (**Table 5**). A value of 1 was used for the activity of SiO_2, due to the presence of euhedral quartz phenocrysts in the glass, and a value of 0.7 was used for the activity of TiO_2, consistent with Colombini et al. (2011). Using these constraints, we believe the temperature recorded within each titanite crystal rim is, at present, the best estimate using the Hayden et al. (2008) thermometer.

The temperatures for the four samples used in this study span a range of ~100°C (~700-800°C, **Figure 8**). This limited temperature range is unsurprising for titanite, a late crystallizing accessory phase, as compared to the larger temperature ranges recorded by earlier saturating phases such as zircon (Colombini, 2009; Claiborne et al., 2017). Thermodynamic models and phase equilibria clearly show that complete crystallization of high-silica rhyolite melts, such as those used in this study, can occur over small temperature ranges (~5-20°C) (Gualda et al., 2012; Tuttle and Bowen, 1958). The results of Zr-in-titanite geothermometry are compared to temperatures using the Zr-saturation geothermometer (Watson and Harrison, 1983), as an independent check on temperature; the two are in close agreement (**Figure 8**).

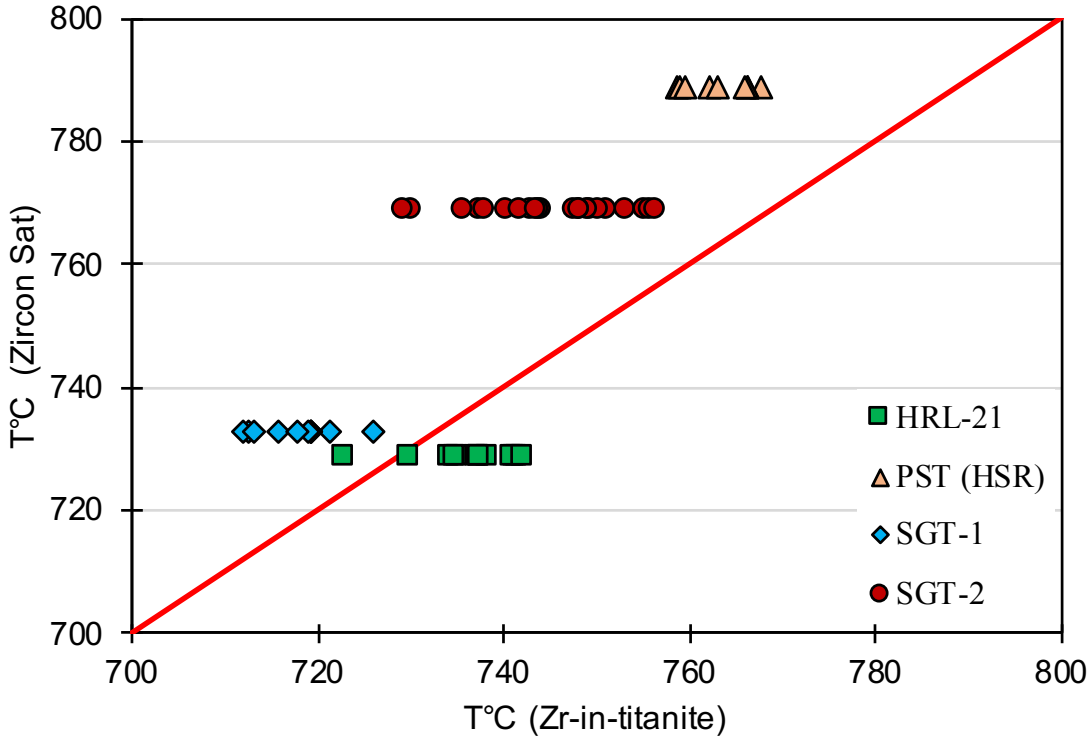

Figure 8: Comparison of the zircon saturation and Zr-in-titanite temperatures (Hayden et al., 2008; Watson & Harrison, 1983) show good agreement for the samples used in this study (temperature range of 700-800°C. Values of 1 for SiO_2 and 0.7 for TiO_2 were used in calculating the Zr-in-titanite temperatures for all samples. Red line is the 1-1 line.

Green and Pearson (1986) used titanite growth experiments to investigate partitioning of REE's at different temperatures and pressures. Their results suggest that the partition coefficient, for any REE, shows a steady increase with decreasing temperature. Our results (**Figure 7**)

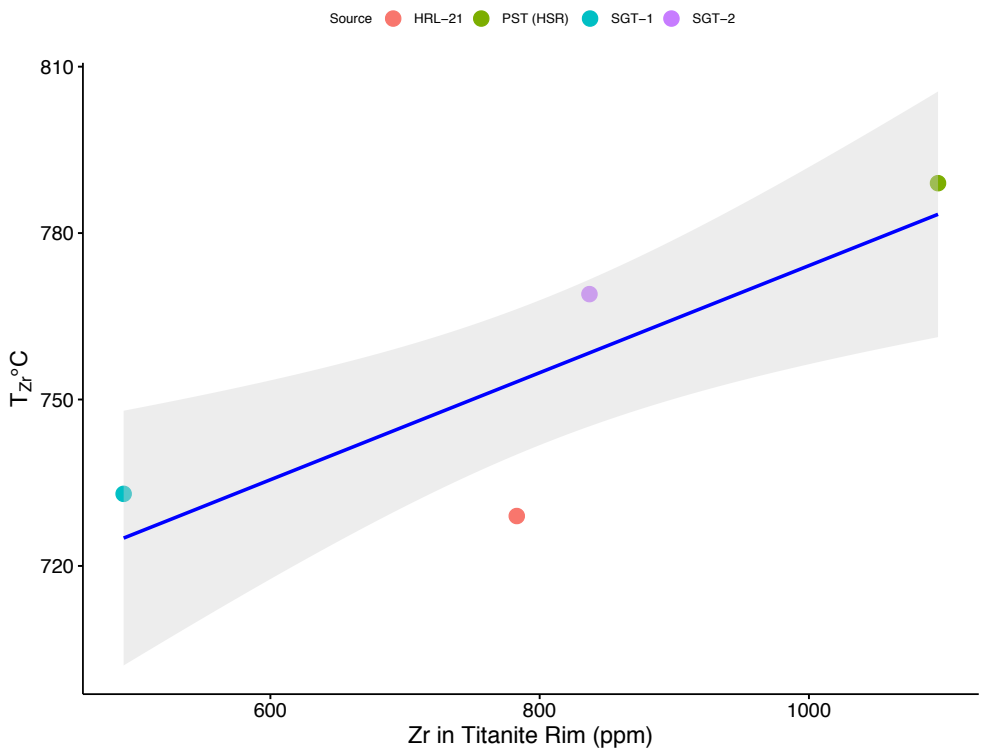

Figure 9: Zr-in-titanite rim versus temperature result from Zr-in-titanite geothermometer (Hayden et al. 2008) demonstrating the relationship between Zr-in-titanite rim with temperature. Pressures used for each sample are from previous studies (Foley, (2017), Wallrich et al. (2018), Bachl et al. (2001)) and by rhyolite-MELTS geobarometry for samples not constrained by earlier studies.

support this finding. Plots of Kd versus Zr-in-titanite rim (**Figure 10**, **Figure 11**, and **Figure 12**) show a negative correlation, where Zr is a proxy for temperature. We propose that the Zr (~temperature) correlated partition coefficients will be useful in constraining the melt compositions of the "lost" melts from which titanite grew.

In **Table 6** we present the regression parameters and the 1σ uncertainty for each model of Kd versus the Zr concentration in titanite rims (determined using .lm function in R). A Monte

Carlo analysis was performed (see supplementary material) to quantify the 1σ confidence intervals for the best fit correlation line for each Kd(element) vs Zr in titanite. The results of the Monte Carlo analysis highlight the relatively small differences (factor of ~2, as noted above) in partitioning over the range of temperatures spanned in this study. In the following section, we test the models using data presented by one study (Sliwinski et al., 2017). Our results show that even with the small amount of variability found in titanite Kd's in near-eutectic melts, the model presented here provides a useful estimate for titanite Kd's for trace element modeling. We then present a case study using Kds estimated in this way to reconstruct melt compositions through time recorded by titanite core to rim spot transects from the middle Searchlight Pluton (D.M. Flanagan, unpub. data)

Table 6: Values for partition coefficient model using .lm function in R. 1σ confidence intervals for the intercept (y) and slope (m) were determined using a Monte Carlo analysis. X-value is the measured Zr (ppm) content of the titanite rim.

Kd	y	m	r^2	m 1σ	y 1σ
La Kd	156.629	-0.064	0.59	-0.117 -0.0145	111.907 200.564
Ce Kd	396.170	-0.211	0.85	-0.292 -0.123	322.485 469.097
Pr Kd	627.960	-0.295	0.53	-0.533 -0.023	397.412 835.332
Nd Kd	950.950	-0.434	0.43	-1.361 0.119	832.560 2041.526
Sm Kd	1445.420	-0.662	0.43	-0.843 0.060	558.564 1301.749
Eu Kd	1293.785	-0.699	0.47	-1.393 0.031	649.205 1905.035
Gd Kd	1353.561	-0.580	0.34	-1.332 0.201	713.117 1972.822
Tb Kd	2044.968	-1.353	0.93	-1.653 -1.032	1780.487 2299.801

Dy Kd	1363.539	-0.646	0.56	-1.209 -0.077	896.076 1846.051
Ho Kd	1354.169	-0.792	0.88	-1.068 -0.515	1126.580 1568.454
Er Kd	1125.113	-0.709	0.85	-0.983 -0.425	888.917 1355.346
Tm Kd	731.630	-0.412	0.85	-0.587 -0.263	608.091 876.878
Yb Kd	520.519	-0.277	0.67	-0.452 -0.104	372.148 661.163
Lu Kd	342.933	-0.175	0.68	-0.282 -0.056	245.709 432.258

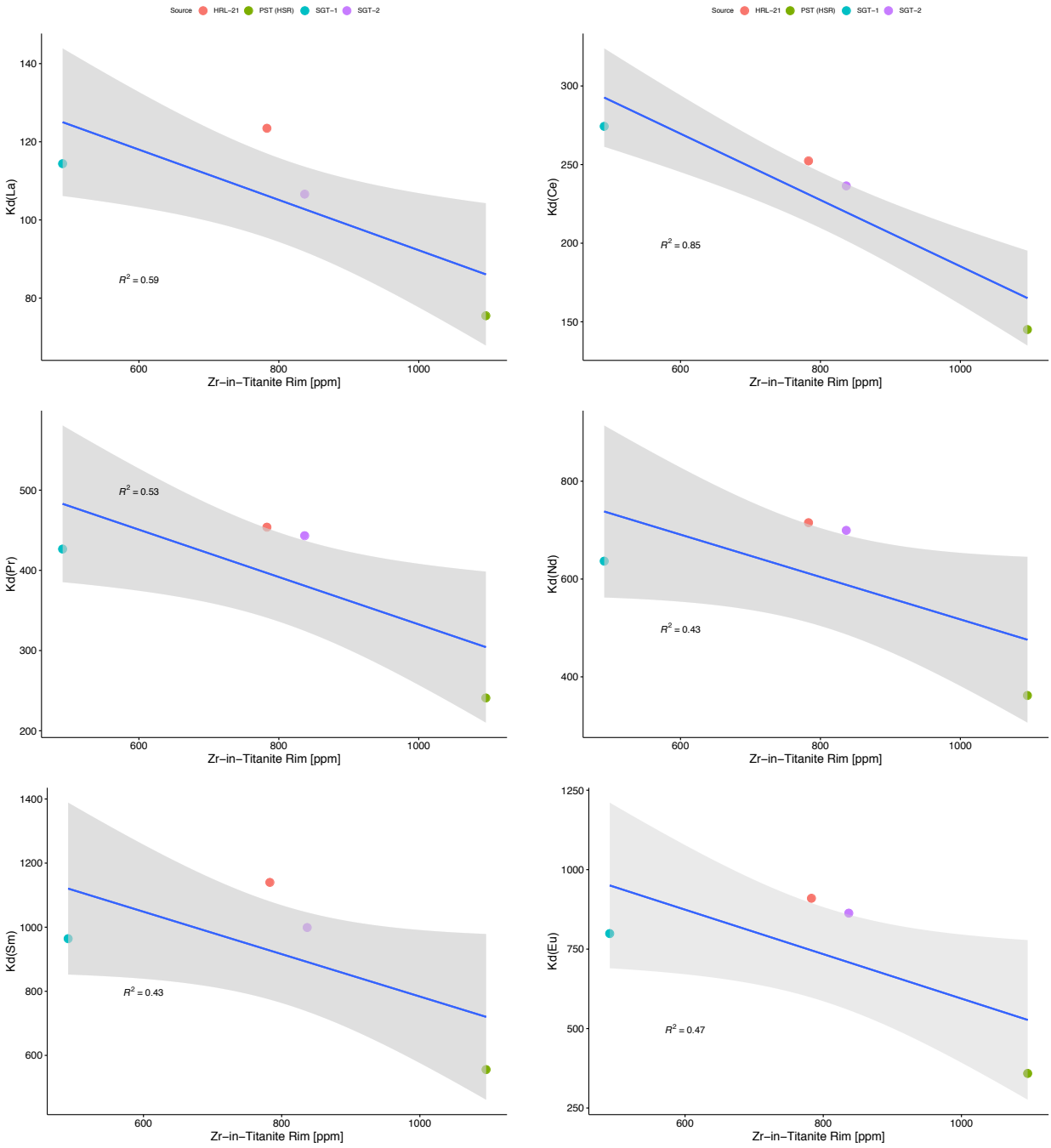

Figure 10: Plots of Kd[La - Eu] against Zr-in-Titanite Rim show strong negative correlations (where Z = element). 1σ confidence intervals for the best fit line through the data are shown in gray on each plot.

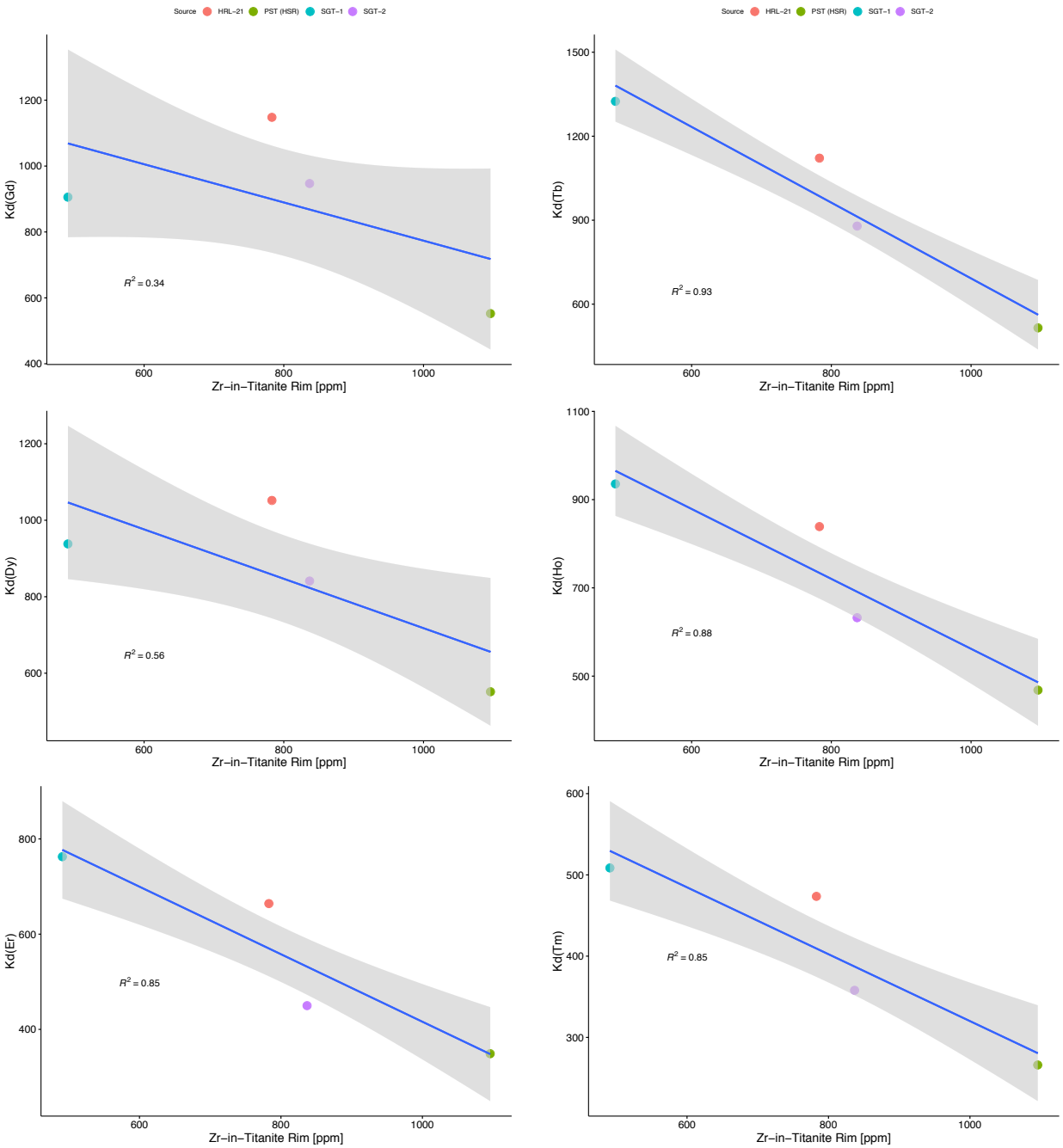

Figure 11: Plots of Kd[Gd - Tm] against Zr-in-Titanite Rim show strong negative correlations (where Z = element). 1σ confidence intervals for the best fit line through the data are shown in gray on each plot.

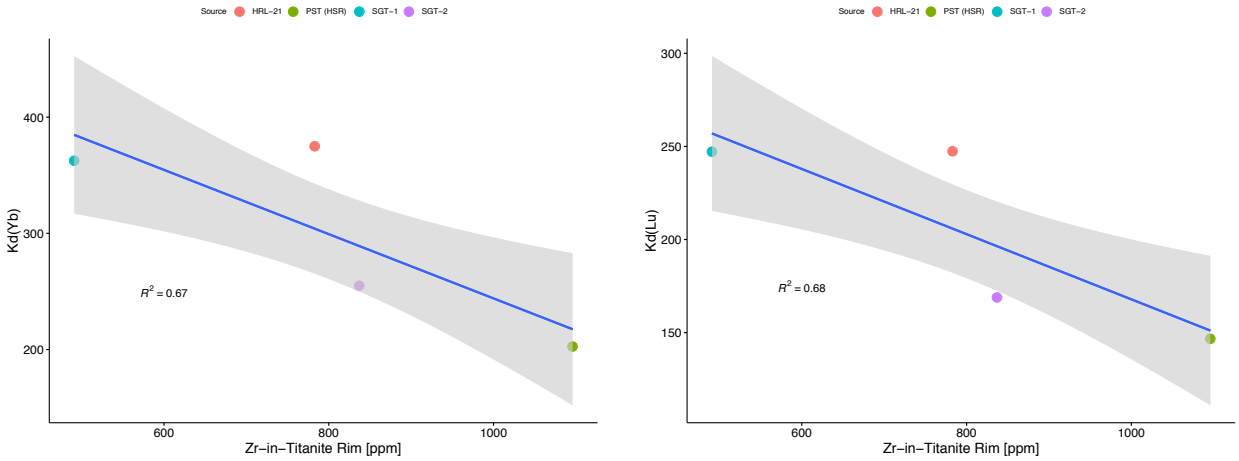

Figure 12: Plots of Kd[Yb - Lu] against Zr-in-Titanite Rim show strong negative correlations (where Z = element). 1σ confidence intervals for the best fit line through the data are shown in gray on each plot.

1.5 Application

We first apply our partition coefficient model to back-calculate the melt composition in equilibrium with the titanite rim composition reported by Bachmann et al. (2005)(sample bcf 83). This sample was not used in the calibration of the Zr-in-titanite model; thus, it provides an independent test of the new model calibration presented in this paper. We then compare the model melt composition to that of the measured coexisting glass composition presented by Bachmann et al. (2005)(**Figure 13**).

To test the application of the new model against a comparable temperature-dependent model for zircon (Claiborne et al., 2017), we performed a similar comparison using the equilibrium model melts generated from Ti concentrations measured in zircon rims from the same volcanic unit (Sliwinski et al., 2017). We then compare both model melts with the actual measured glass composition from the same sample (**Figure 13**). The shape of both model melts

capture the overall shape observed in the melt. However, the Zr-in-titanite model melt composition provides a much closer fit. We posit that the closer fit is due to the much higher concentrations of REE and Zr^{4+} in titanite than REE and Ti^{4+} in zircon (extreme incompatibility of LREE). For this reason the Ti-in-zircon model has a higher uncertainty and much greater susceptibility to effects of small inclusions (false high measured concentrations) for LREE.

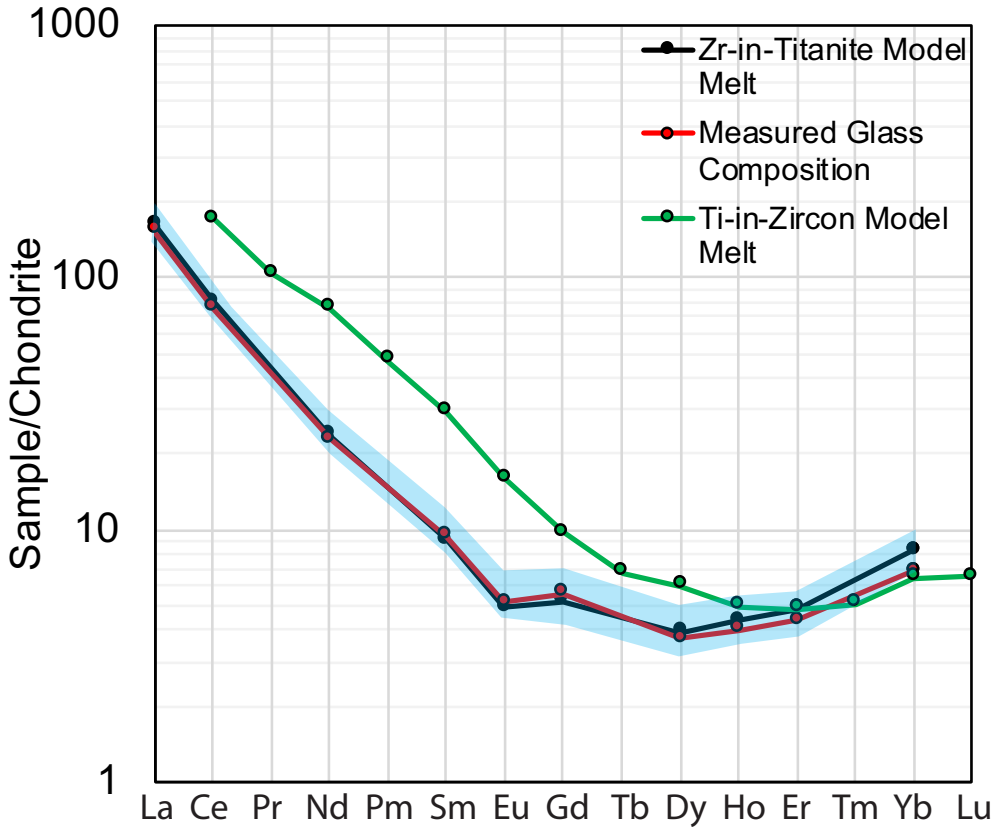

Figure 13: Ti-in-Zircon vs Zr-in-titanite model melt comparison. Comparison of Ti-in-Zircon Kd equilibrium model melt composition using the Claiborne et al. (2017) calibration and the average zircon rim composition collected by Sliwinski et al. (2017) for Fish Canyon Tuff glass compared to Zr-in-titanite model melts and the actual measured melt composition. Lu (Z=71) is not included in the titanite model melt calculations because it was not reported in Bachmann et al. (2005) titanite data. It was included in the zircon data from Sliwinski et al. 2017. Blue shaded region is the 1σ confidence interval for the Zr-in-titanite equilibrium model melt.

The modeled melt composition from the new partition coefficient model and the modeled melt composition calculated from the static Kd's presented by Colombini et al. (2011) closely match

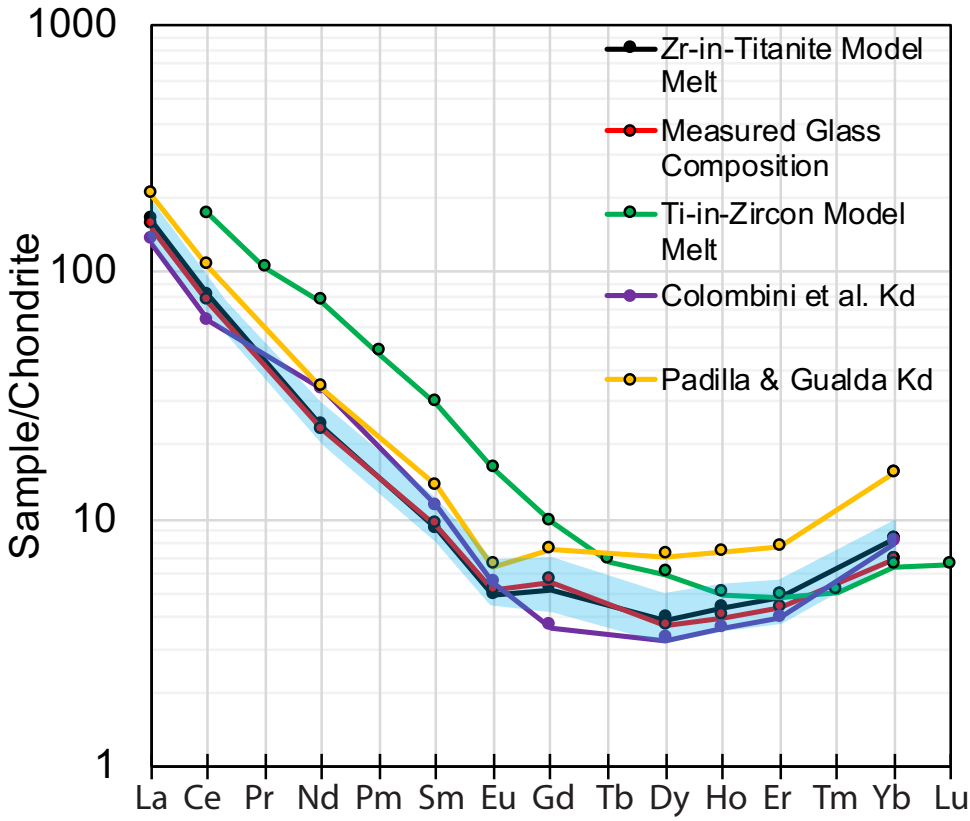

Figure 14: Comparison of back calculated equilibrium model melt compositions using the temperature independent Zr-in-titanite calibration (in this study), the Ti-in-zircon calibration (Claiborne et al. 2017) and the temperature dependent titanite Kd's presented in Colombini et al. (2011) and Padilla & Gualda (2016).

the measured glass composition presented by Bachmann et al. (2005) (**Figure 14**). However, we argue that since the Zr content of the Highland Range HSR glass (Colombini et al., 2011) and the Fish Canyon glass (Bachmann et al., 2005) are similar, it is expected that the model melts using temperature-independent Kd's from Colombini et al. (2011) would be similar. Furthermore, as the titanite and glass compositions diverge from those used to determine the temperature-independent Kds, calculated Kds will also diverge (**Figure 14**). Conversely, the model melt

produced by the Zr-in-titanite-based partition coefficient model will more reliably produce accurate results when compared to temperature-independent and Ti-in-zircon model melts, within the ~700-800 ºC temperature window, due to the higher abundances of REE's in titanite.

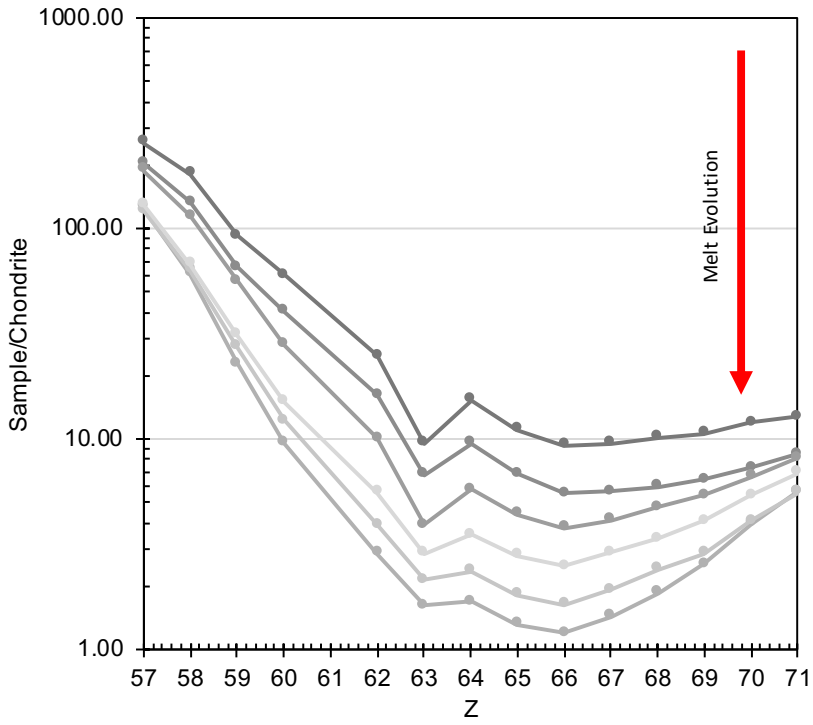

Figure 15: Model melt REE patterns for one titanite grain from middle-SLP (gray scale color: dark at core and light at rim) show the melt evolution as recorded by titanite from the middle Searchlight Pluton (SLD10-6 analyses 9.1-9.6; D.M. Flanagan data).

1.6 Interpretations and Conclusions

1. We present measured titanite-glass Kds for four high silica rhyolite samples from diverse petrogenetic environments that are robust, based on the following evidence:
    a. REE, except for multivalent Eu, fit well with lattice strain models.
    b. All Kds are consistent with previously published data and provide better constraints on

rim compositions, using the {111} section specifically, from multiple different magmatic environments at near-eutectic conditions.

2. We propose a system of estimating Kds that apply to a range of conditions relevant to HSR environments.

    a. There is a negative correlation between REE Kds and temperature; the negative slope of the Kd pattern is steeper for samples with higher Kds (e.g. Middle-REE).

3. Correlation of Kds with Zr concentration in titanite (proxy for temperature) permits useful approximate estimation of Kds for any zone in magmatic titanite that grew within the range of samples presented here. We provide best-fit equations with uncertainty intervals for Kds as a function of Zr in titanite that can be used to estimate the melt compositions of "lost" magmas from which the titanite zones grew (e.g., titanite interiors; titanite in plutonic rocks and detrital samples).

4. Testing of the temperature dependent partitioning model suggests that the model is robust and provides reasonable constraint on the Kds to be used based on the crystal rim composition.

Uniformly very high but highly variable $D_{REE}^{Titanite-Liq}$ suggests that titanite, where present, exerts a very important role in REE distribution during magma fractionation. Specifically, it will tend to deplete all REE, with an especially pronounced effect on MREE depletion (Glazner et al., 2008; Colombini et al., 2011).

2: SITGREAVES TUFF: INSIGHTS INTO POST SUPERERUPTION SILICIC MAGMATISM

2.1 Introduction

The temperature and pressure conditions under which high silica melts (>76 wt% SiO_2, anhydrous basis) are generated and evolve are constrained by quartz-feldspar phase equilibria, which generally requires low pressure, upper crustal conditions, as well as fractional crystallization (Gualda and Ghiorso, 2013). At low pressure, the quartz-feldspar cotectic is displaced toward the quartz apex (Tuttle and Bowen, 1958; Wolff, 2017). These conditions often exist at the terminal stages of melt evolution; due to this convergence, one could say that the quartz-feldspar cotectic is where "melts go to die". However, if conditions are right, these terminal-stage melts can be erupted, as commonly shown by the existence of long-lived high silica rhyolite volcanic and plutonic centers (e.g. Peach Spring Tuff, Spirit Mountain batholith, and Yellowstone)(Claiborne et al., 2010; Troch et al., 2017; Foley, 2017; Pamukcu et al., 2013).

The Miocene Peach Spring Tuff (PST) of NW Arizona, SE California and southernmost Nevada is a prime example of the products of a supereruption, where large volumes of near-eutectic melt was mobilized and erupted (Ferguson et al., 2013; Ferguson, 2016; Pamukcu et al., 2013; Frazier, 2013; Foley, 2017; Young and Brennan, 1974; Buesch and Valentine, 1986). Due to excellent exposure of the highly dissected pre- to post-PST volcanic section in the vicinity of the source caldera (Silver Creek caldera (SCC); (Ferguson et al., 2013)) in the southern Black Mountains, AZ, this volcanic succession is a prime location to investigate the events leading to and following a supereruption. Recent research focused on the PST itself has constrained the architecture of and processes within Peach Spring magma body, including characterization of

pre-eruptive magmatic conditions (pressure, temperature, phases, petrogenesis) (Ferguson et al., 2013; Pamukcu et al., 2013; 2015; Foley, 2017, Foley et al., in revision; Flansburg, 2015; Frazier, 2013a). However, the pre- and post-PST silicic volcanics are far less studied (Lang et al., 2008; McDowell et al., 2016, 2014), and post-PST ignimbrites have been overlooked except for very preliminary work (Wallrich et al., 2016). In this chapter, I expand upon the record exposed in a section (~140 m, **Figure 21**) of silicic tuffs within Meadow Creek Basin (MCB), ~6 km east of the SCC. These post-supereruption silicic tuffs provide a unique opportunity to gain a better understanding of the changes that occur within the magmatic system following a supereruption and, in this case, immediately preceding (possibly contemporaneous with?) regional extension (Murphy and Faulds, 2003; Faulds et al., 2002, 1999). They also provide a glimpse into the genesis of silicic magmas during the waning stages of a volcanic center that may be applicable to other localities.

Geologic Setting: Northern Colorado River Extensional Corridor

The Northern Colorado River Extensional Corridor (NCREC, **Figure 16**) is a 50 to 100 km wide region of Miocene crustal extension located along the eastern margin of the Basin and

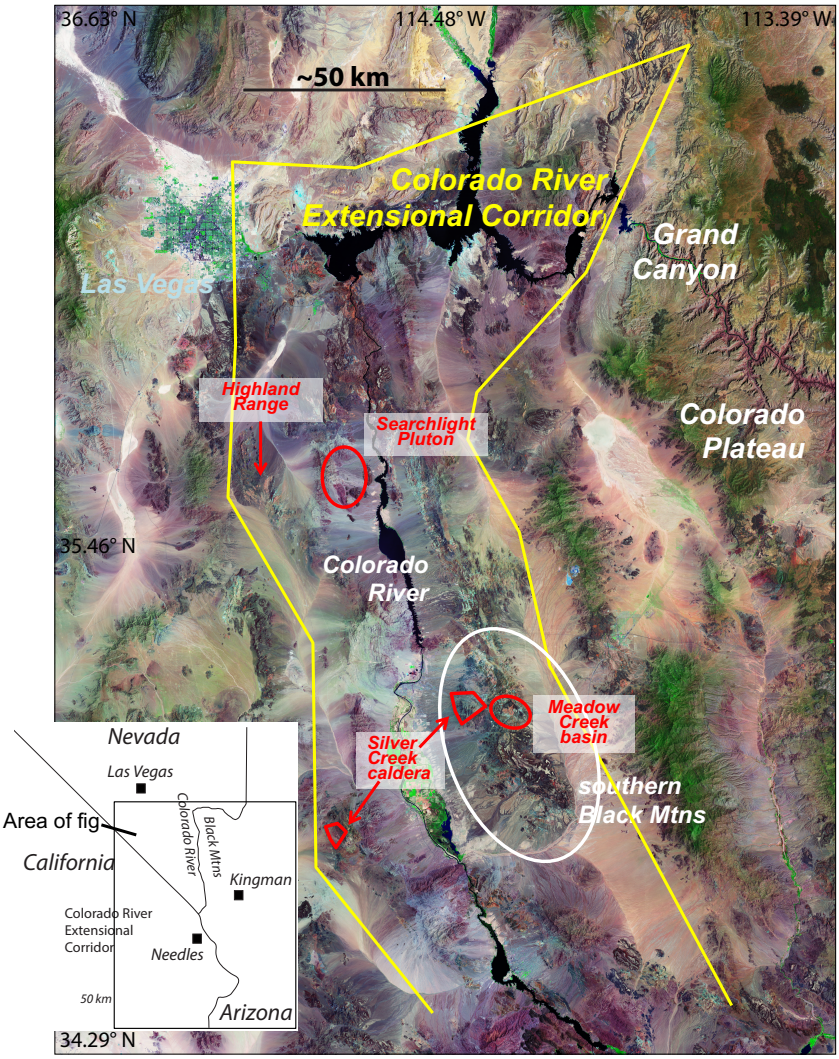

Figure 16: Overview of the Colorado River Extensional Corridor showing the locations of prominent locations of geologic interest including Meadow Creek Basin, the type locality for the Sitgreaves Tuff and the Silver Creek Caldera, source of the ~18.8 Ma Peach Spring Tuff Supereruption.

Range province in CA-NV-AZ. It has been the site of numerous investigations centered around the caldera-forming Peach Spring Tuff (PST) supereruption and the volcano-plutonic connection

in the Searchlight pluton-Highland Range section (Faulds et al., 2001, 1999; Colombini, 2009; Colombini et al., 2011; Foley, 2017; Miller and Miller, 2002; Claiborne et al., 2006; Walker et al., 2007; Bachl et al., 2001; Frazier, 2013; Pamukcu et al., 2013; Lang et al., 2008). In this work, we focus on the record preserved at the Meadow Creek Basin, part of the NCREC (Figure 19).

Southern Black Mountain Volcanic Center

Pre-PST Record

The pre-PST (~19.5 to 18.8 Ma) section consists primarily of voluminous trachytic and trachyandesitic lavas (commonly with abundant plagioclase and biotite phenocrysts) with lesser amounts of basaltic and rhyolitic tuffs and lavas (**Figure 17**) (Valentine et al., 1989; Flansburg, 2015; Buesch, 1992; Buesch and Valentine, 1986; McDowell et al., 2014, 2016). These deposits extend up to 15 km from the caldera margin in multiple directions (north, east, south) and exceed 1 km in total thickness throughout the southern 40 km of the Black Mountains (McDowell et al., 2016; Lang et al., 2008; Ferguson et al., 2013; Pearthree et al., 2009; Thorson, 1971; Ransom, 1923). Zircon saturation thermometry and Ti-in-zircon thermometry for relatively silicic rocks suggest that during the ~200 ka preceding the PST eruption magmas within the SBMVC were hot, with temperature of silicic magmas up to 900 °C (McDowell et al., 2014; Scheland et al., 2016; Perry et al., 2014). Input of large volumes of mafic magmas into the crustal magmatic system has been implicated as a thermal primer for the crust ultimately allowing for the genesis and storage of large volumes of silicic magmas (McDowell et al., 2014; Flansburg, 2015).

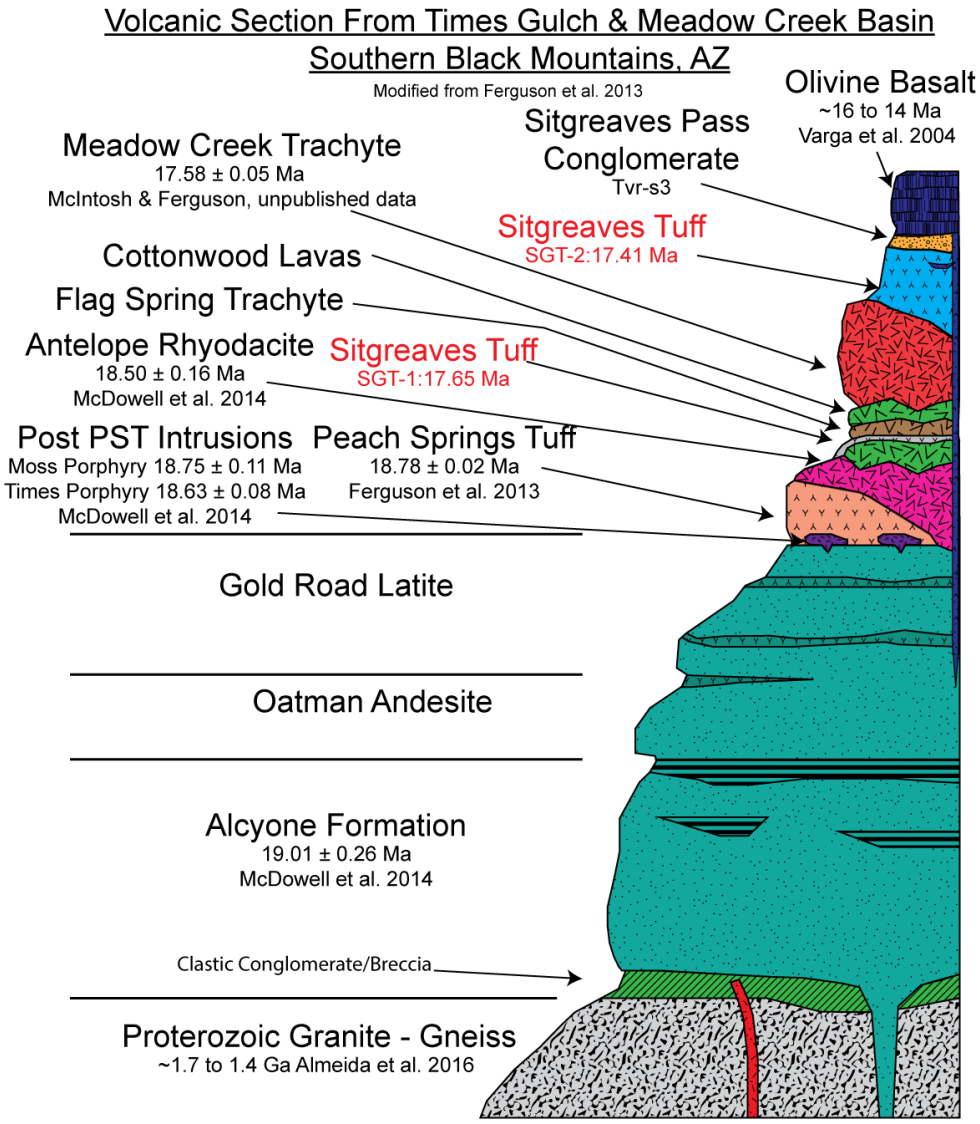

Figure 17: Stratigraphic section of the volcanic section from Times Gulch and Meadow Creek Basin, Southern Black Mountains, NW AZ. Modified from Ferguson (2016). New dates from this study for Sitgreaves tuff unit 1 and 2 are in red. Interbedding of SGT1 and Cottonwood lavas is based on the interpretations of Thorson (1971) and field observations by this study. However, these interbedding relationships could be variable and more geochronology work is needed to unravel this.

Supereruption

The PST supereruption (18.78 ± 0.02 Ma; Ferguson et al. 2013) outflow covers an area >35,000 km^2 and has a recently estimated volume of ~ 1300 km^3 (Glazner et al., 1986; Buesch,

1992; Ferguson et al., 2013). The Silver Creek Caldera, source caldera of the PST (SCC; Ferguson, 2008; Ferguson et al. 2013), is located within the southern Black Mountains. The eruptive deposits are composed of multiple units, notably, the intracaldera trachyte identified by Ferguson et al. (2013), the outflow high silica rhyolite (Pamukcu et al.,2013), and the outflow-capping Warm Springs trachyte (Foley et al., in revision). Geochemistry and textures coupled with thermobarometric modeling have elucidated both the pre-eruptive magma chamber conditions and the arrangement of the magmatic system within the crust. The findings of multiple studies suggest the magma body was stored in the shallow crust at a pressure of ~185-280 MPa (Rhyolite MELTS geobarometry; Pamukcu et al. 2015; Foley et al., in revision) with variable crystal fraction and temperatures, ranging from ~740-900°C (Foley, 2017; Foley et al., in revision; Pamukcu et al., 2013; and references therein).

Post-PST Record

Volcanic activity following the PST supereruption comprised intermediate to rhyolitic lavas and tuffs that are overlain by volcaniclastic sediments. Total thickness of these deposits ranges from ~100 to 800 m. These units unconformably overly the pre-PST trachytes within a 10 km radius surrounding the Silver Creek

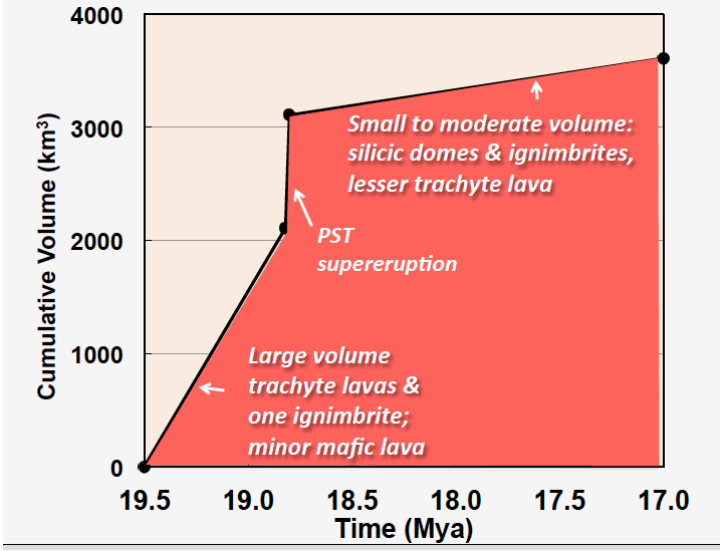

Figure 18: Schematic diagram of the estimated volume of erupted material with time in the SBMVC.

Caldera (Lang et al., 2008; Ferguson et al., 2013; Thorson, 1971; Ransom, 1923). McDowell et al (2014, 2016) suggest that post-PST volcanism was driven by magma recharge that periodically reinvigorated the waning volcanic center, producing relatively small volume, elementally and isotopically diverse eruptible batches of magma (**Figure 18**). Similar to pre and syn-supereruption magmas, post-PST magmas were generated from a combination of enriched mantle- and Paleoproterozoic crust-derived sources; however, they were more isotopically diverse and in general richer in the juvenile component (McDowell et al., 2014, 2016; Frazier, 2013).

2.2 Methods

Fieldwork

Fieldwork was conducted over four sessions between 2016 and 2018, with the first two excursions occurring during the Vanderbilt University Supereruption REU. During these expeditions we mapped the extent of the Sitgreaves tuff within and surrounding MCB, documented contact relations of the tuffs (internal and external), and collected samples for lab analyses. Our study built upon the understanding of the post-supereruption deposits originally described by Thorson (1971).

Thin Section Petrography

Billets were cut to size using a rock saw and shipped to R.A. Petrographic for thin section preparation. A Zeiss Axioskop 40 petrographic microscope, equipped with an AxioCam MRc 5 camera, at Vanderbilt University was used for mineral identification and photo documentation. See APPENDIX E for thin section tables.

Whole Pumice/Rock Geochemistry

To obtain pumice whole-rock compositions, whole pumice samples were extracted from rock fragments, powdered (mortar and pestle) and cleaned. Pumice clasts were first rinsed in deionized water and placed in a sonic bath for ~20 min. Samples were then poured through funnels lined with filter paper. Upon completion of filtration (time 30 min to 2 hours) samples were placed in an oven at 110 °C until dry. Three additional sonic bath, filtration and drying cycles followed the preliminary deionized water rinse. In the second step, 0.1M hydrochloric acid was used, while 2% hydrogen peroxide was used in step 3 followed by a deionized water rinse. Whole rock (lithic-fragments from within the tuff and bulk tuff) samples were cut in thin strips to minimize the "nugget effect" and the weathered edges were removed. Samples chosen for whole-pumice and rock analysis were sent to Activation Laboratories (Canada) for major and trace elements analysis (package: 4E ICP-MS). Elemental abundances were measured using a combination of fusion inductively coupled plasma mass spectrometry (FUS-ICP-MS), total digestion ICP (TD-ICP), and instrumental neutron activation analysis (INAA).

Glass and Mineral Chemistry

Scanning Electron Microscope

Energy dispersive spectroscopy (EDS) analysis using a Tescan Vega 3 LM variable pressure SEM equipped with an Oxford X-max 50 mm^2 EDS system and a LaB_6 filament was conducted at Vanderbilt University. USGS standard, RGM-1 for high silica glass was run daily as a secondary standard. Backscattered electron (BSE) images and quantitative EDS analyses were collected for major element concentrations of glass and phenocryst phases. During these

analyses the sample working distance was maintained at 15 mm, an electron beam acceleration of 15 kV and maximum beam intensity of 19 were used, resulting in absorbed currents of ~10 nA. Aztec processing software, developed by Oxford, was used for data acquisition and processing. Precision and accuracy of SEM-EDS measurements are discussed by Pamukcu et al. (2015).

Laser Ablation Inductively Coupled Plasma Mass Spectrometry

We determined concentrations of dispersed elements in glass and minerals by LA-ICPMS using a Photon Machines Excite 193 nm excimer laser ablation unit connected to a Thermo iCAP Q ICPMS installed at Vanderbilt University. We set the laser settings to yield a fluence of 4.8-5.0 J/cm^2, at a repetition rate of 10 Hz (15Hz for 7x50 μm spots) for 50x50 μm spots in glass, with He (0.9 min^{-1}) as the carrier gas. Each analysis (individual spot and line of spots) began with 30 s of blank acquisition, followed by 60 s of ablation and 30 s of wash-out time to allow the measured values to return to blank levels.

We measured a total of 36 analytes during each analysis. For every 15 measurements of unknowns for individual spots and every individual line of spots, we analyzed 3 primary (for calibration) and secondary (treated as unknowns) standards to evaluate the precision and accuracy of the results. We used NIST 610 as the primary standard and NIST 612, NIST 614, and RGM-1 glasses as secondary standards (Pearce et al., 1997). We chose ^{28}Si as the internal standard for glass and minerals, using average sample SiO_2 contents as determined for each unique location by SEM-EDS analysis prior to trace element collection. In samples where multiple composition domains were identified within a crystal, the average SiO_2 concentration within each domain was used as the internal standard

$^{40}Ar/^{39}Ar$ Geochronology

Sanidine separates were obtained for the pumiceous samples (SGT-1 and SGT-2) by extracting individual pumice from the tuffaceous host rock followed by lightly crushing with a baseball bat and sieving. The crystals were separated using different size sieves. Each size fraction was then winnowed by water to concentrate the mineral phases. The sanidine separates were then hand-picked under a stereomicroscope and checked for composition on the SEM using EDS prior to sending to the New Mexico Tech Geochronology Lab, where they were analyzed by W.C. McIntosh.

Geobarometry

Multiple different geobarometers were employed to further constrain the pre-eruptive storage conditions of post supereruption magmas. Rhyolite-MELTS geobarometry (Gualda & Ghiorso 2014) was performed using all high silica rhyolite glass compositions. In all cases, quartz and one to two felspars were observed to be in equilibrium with the coexisting glass. Requirements for use of rhyolite-MELTS geobarometry are straightforward, needing only a glass composition of interest and the phase assemblage in equilibrium with melt of that composition. The model then determines the equilibrium assemblage at each temperature and pressure step and searches for the point at which quartz and feldspar(s) are simultaneously saturated at the liquidus, which is the only set of conditions at which liquid of the given composition can be in equilibrium with the desired mineral assemblage. Gualda and Ghiorso (2014) define the point of simultaneous saturation when the saturation temperature between the phases is ≤5 °C (See Gualda and Ghiorso

(2014) for more information on the theory, process, and application of the rhyolite-MELTS geobarometer).

Amphibole barometry (Mutch et al., 2016) was used as an additional method for constraining the storage pressures. Both units within the Sitgreaves Tuff contain euhedral to subhedral amphibole phenocrysts that generally appear to be in equilibrium with the coexisting glass, some are fragmented likely due to decompression (See Best and Christiansen (1997)). However, SGT1 is the only unit that contains the appropriate mineral assemblage, amphibole + plagioclase + biotite + quartz + alkali feldspar + ilmenite/titanite + magnetite + apatite, for use with the Mutch et al. (2016) calibration. Therefore, the results obtained from SGT2 amphibole are purely speculative.

2.3 Results

Field Observations

Sitgreaves Tuff Unit 1 (SGT1)

SGT1 is ≤ 30 m thick and composed of interbedded pyroclastic flow and fall deposits (**Figure 21**). It locally overlies paleo-topography formed on pre-PST lavas (Gold Road Latite and Antelope Rhyolite of Thorson 1971). The Antelope Rhyolite has been dated at 18.50 ±0.16 Ma (SHRIMP zircon age; McDowell et al., 2014); Gold Road Latite is undated. Within Meadow Creek Basin SGT1 is directly overlain by SGT unit 2. Previous mapping by Thorson (1971) suggests that SGT1 may be interbedded with silicic lavas within the region (**Figure 17 and Figure 19)**).

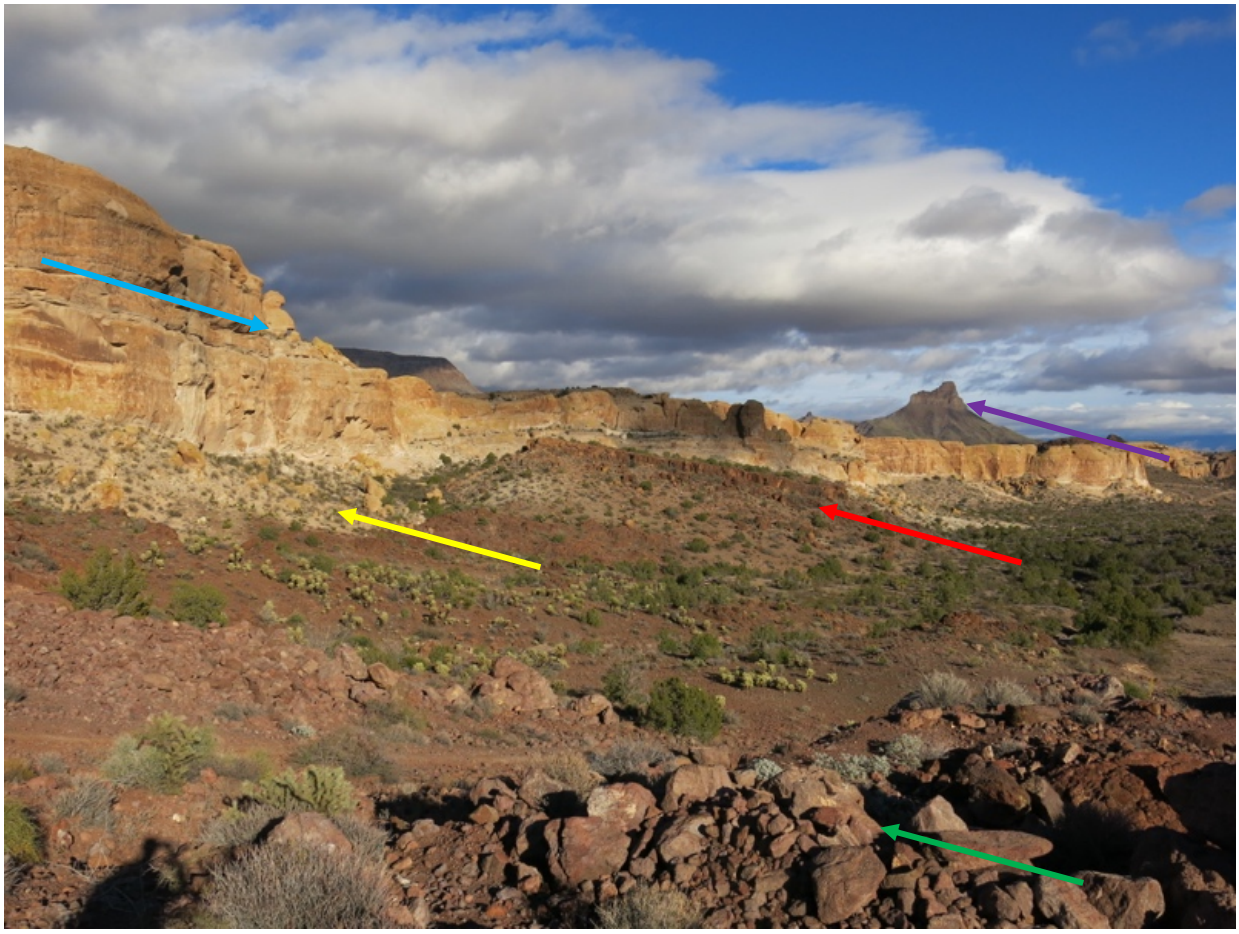

Figure 19: Exposure of the Sitgreaves Tuff section within Meadow Creek Basin. SGT-1 forms the lower apron (yellow arrow) below the cliff forming SGT-2 unit (blue arrow). The prominent peak in the background is Thimble mountain, volcanic neck of basaltic-trachyandesite composition (purple arrow). The dark flat topped feature in the middle of the image is the silicic Antelope Lava flow (red arrow), which preceded the ignimbrite forming eruptions by ~1 Ma. The dark red-brown rubbly material (green arrow) in the foreground is the Gold Road Latite (Pre-PST supereruption lava flow)

Individual SGT1 flow deposits range in thickness from 0.25 m to 10 m and contain 20 - 40% pumice and 10 - 20% lithic fragments. Fall deposits range in thickness from ~2 cm to 5 cm, with complete fall sequences up to 0.5 m thick. Flow deposits are composed of multiple different types of lithic fragments which I interpret to be vent and ground-surface-derived (less silicic) lithics, juvenile (cogenetic) lithics and pumice within a matrix of ash. Both fall and flow units contain a notably higher abundance of exotic lithic fragments when compared to SGT2. For field

photographs of SGT1 see APPENDIX C

Sitgreaves Tuff Unit 2 (SGT2)

SGT2 is an incrementally emplaced, lithic-rich (up to 30%) pyroclastic flow unit, with pumice-rich interspersed fall deposits ~140 m thick (**Figure 21**). Deposit thickness is variable with thin (~10 m thick, condensed sections) ignimbrite veneer deposits marking paleo-ridges and thick (~140 m) valley pond deposits marking paleo-valleys (**Figure 20**). Lava flows that directly underlie SGT-2 include the Meadow Creek Trachyte (Thorson (1971);17.58 ±0.05 Ma, $^{40}Ar/^{39}Ar$

Figure 20: Images of SGT outcrops (A) Cross section view of the paleo-valley fill deposit within Meadow Creek Basin. Black lines trace our apparent flow unit boundaries. Image taken to the east of Meadow Creek basin looking west. (B) SGT2 ignimbrite veneer deposit blanketing paleo-topography (Gold Road latite). Elephants Tooth, Oatman, AZ landmark, just to the left of the deposit is a volcanic neck composed of porphyritic rhyolite.

sanidine, McDowell et al. (2014)), Gold Road Latite and Flag Spring Trachyte (stratigraphically below the MCT according to Thorson 1971). Both of these lavas are also found as lithics within the pyroclastic deposits. The bulk of the lithics found within SGT2 are interpreted to be

cogenetic spherulitic and flow-banded rhyolite. Maximum lithic size is 3 m (average 1-5 cm) and the relative abundance of lithic clasts is up to 40%. The larger (>1 m) lithic mega-blocks are only found within Meadow Creek basin. The matrix within SGT2 consists of blocky, vesicle wall type vitric shards and fragmented phenocrysts of sanidine, quartz and titanite. Flow boundary zones are discrete throughout most of the pyroclastic flow units; however close inspection reveals frequent changes in grading. For field photographs of SGT see APPENDIX D.

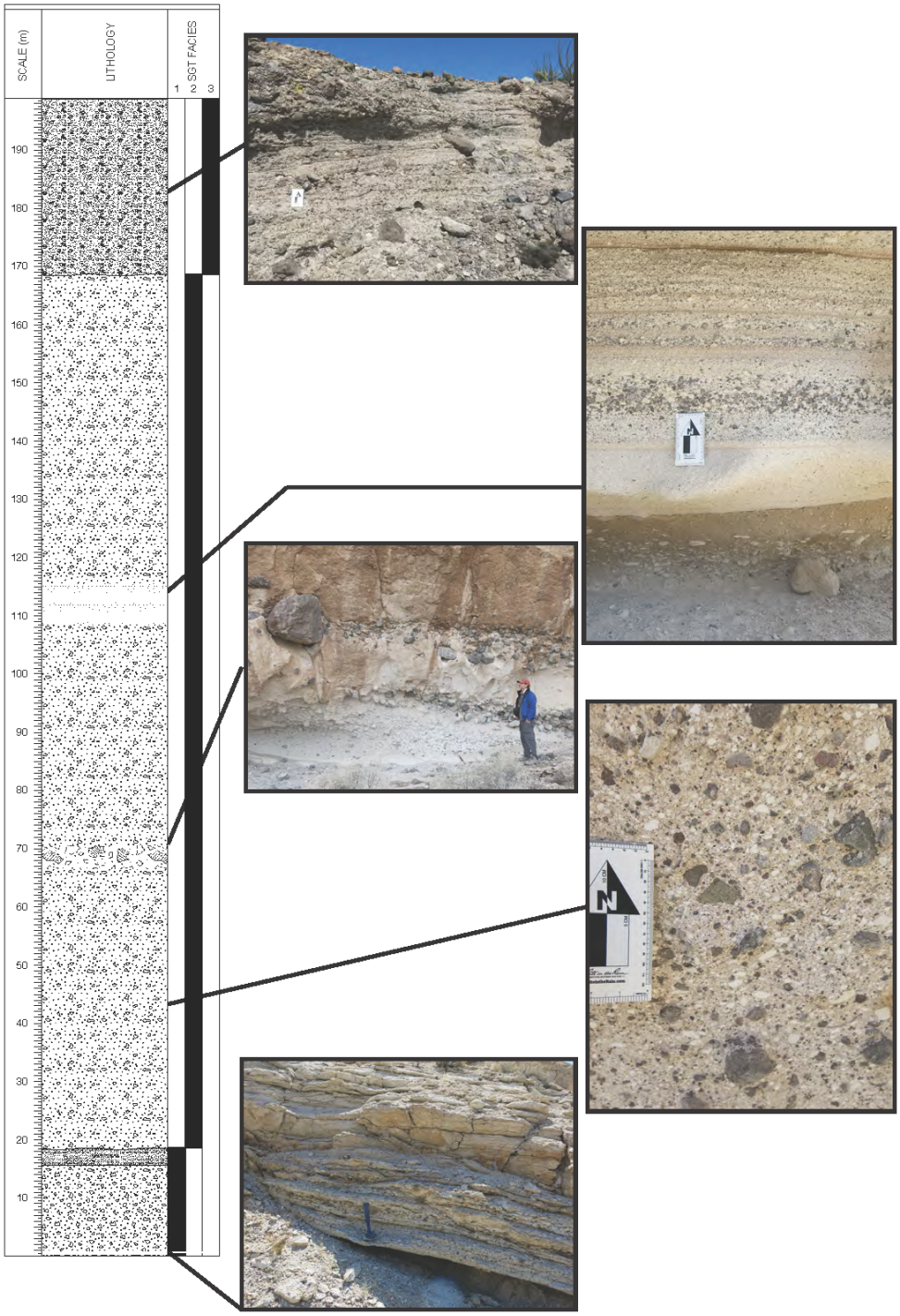

Figure 21: Sitgreaves Tuff stratigraphic section within Meadow Creek Basin. Pictures show distinct and representative horizons from within the ignimbrite section. Bar on the right of the schematic section shows the unit with respect to its thickness. SGT-3 is composed of reworked volcaniclastic sediments and is therefore omitted from this study.

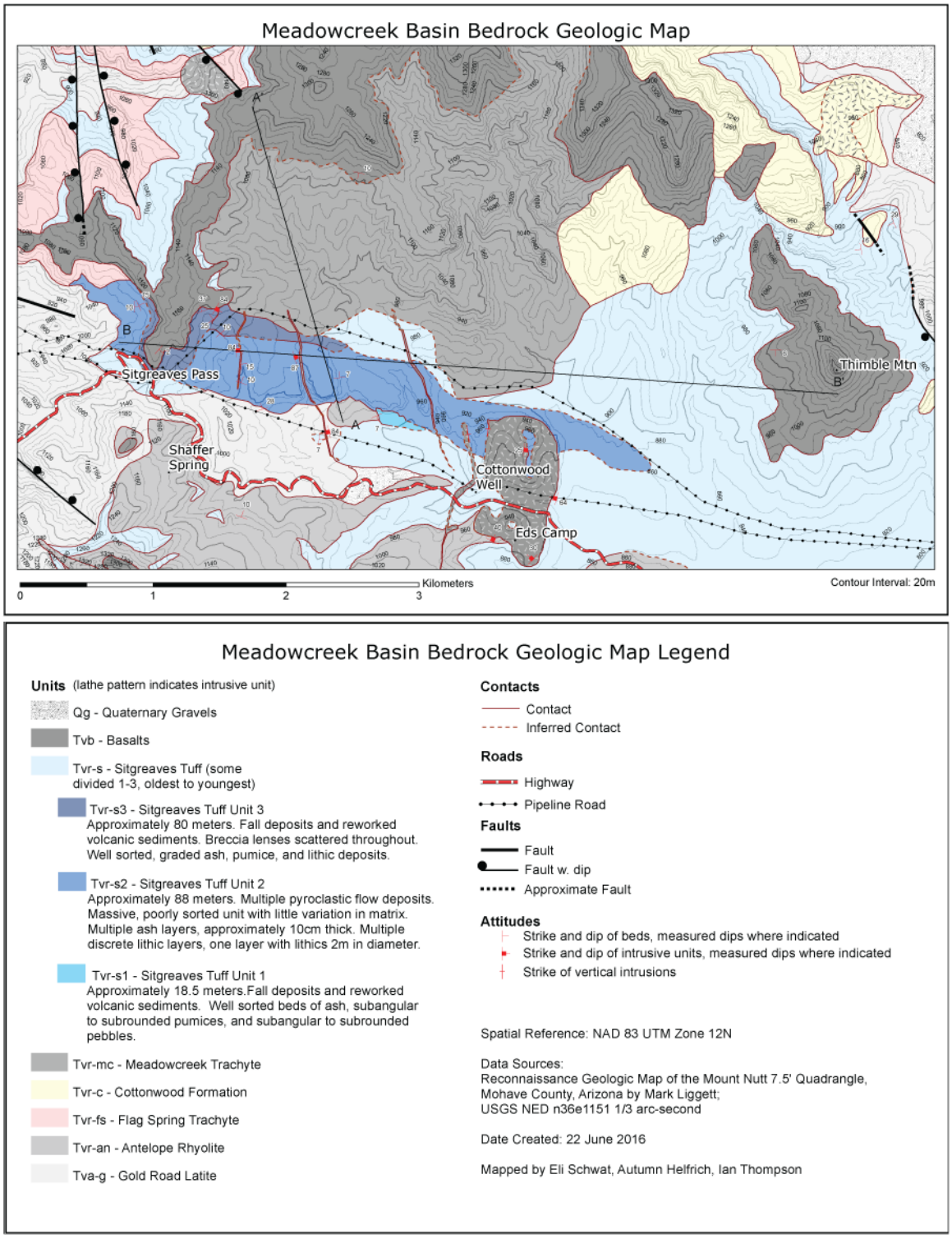

Figure 22: Geologic map of Meadow Creek Basin (Schwat et al., 2016).

$^{40}Ar/^{39}Ar$ Geochronology

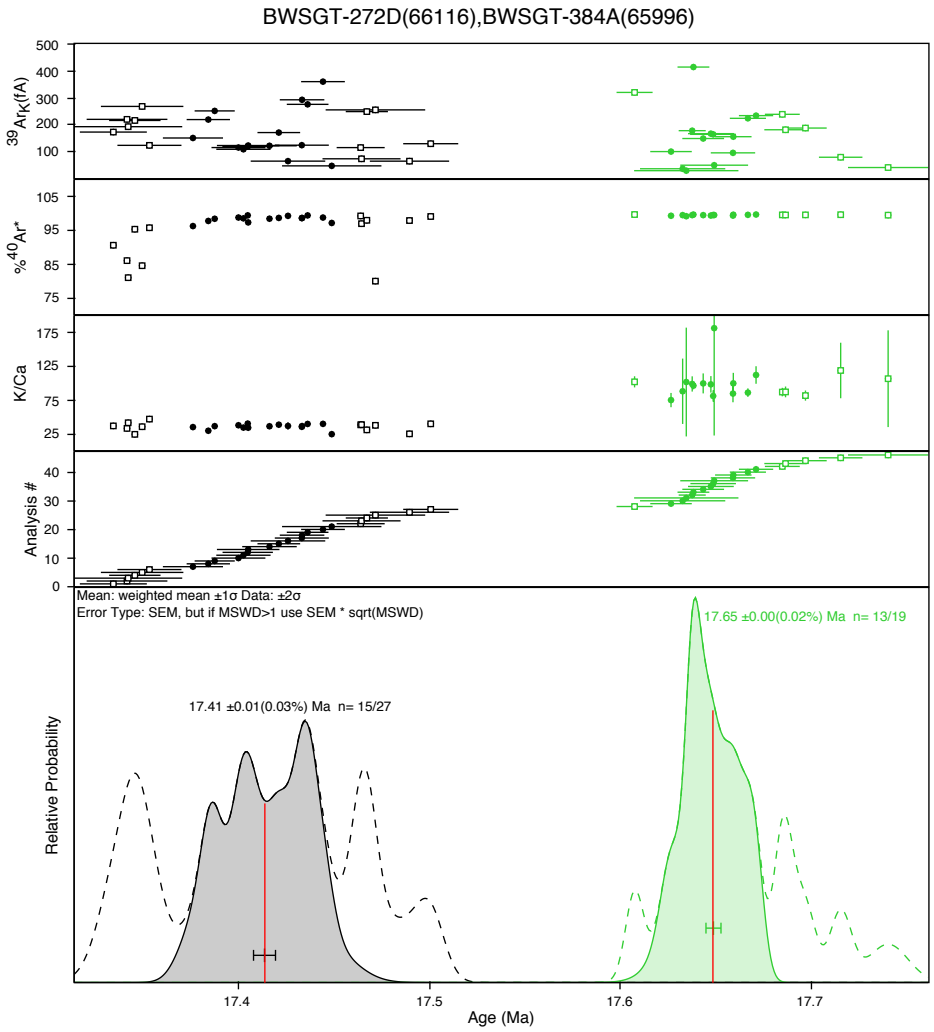

Figure 23: Results of $^{40}Ar/^{39}Ar$ analyses for SGT-1 (green) and SGT-2 (gray). Results suggest an age of 17.65 ± 0.008 Ma (red bar, n=13) for SGT-1 and 17.41 ± 0.016 Ma (red bar, n=27) for SGT 2.

Results from $^{40}Ar/^{39}Ar$ geochronology are consistent with the observed field relations. SGT1 sanidine returned an age of 17.65 ± 0.008 Ma. Field relations from the sampled outcrop place this unit in direct contact with and beneath SGT2. Elsewhere within the Southern Black Mountains the relationship is ambiguous. Thorson (1971) suggests that the pyroclastic units that compose the SGT, divided into two units by this study, are interbedded with the currently

undated Cottonwood series (total of 6 lava flows) and Flag Spring lavas. Mineralogically, the Cottonwood and Flag Spring lavas generally contain less plagioclase and more sanidine and appear to span the temporal gap between SGT1 and SGT2. For this reason, we show SGT1 interbedded with these two flow units in **Figure 17**.

Results from geochronology for SGT2, together with field relations, demonstrate that it is the youngest ignimbrite unit within the Meadow Creek Basin at 17.41 ± 0.0016 Ma. Field relations are unambiguous and show that SGT2 clearly was deposited onto paleo-topography underlain by Meadow Creek Trachyte, Gold Road Latite, Flag Spring Trachyte, and SGT1. In addition, lithics of Meadow Creek Trachyte can be found within the tuff.

Sitgreaves Tuff Unit 1 Geochemistry

SGT1 Whole Pumice/Bulk Tuff

Four samples were sent out for geochemical characterization from SGT-1 (BWSGT-295B, BWSGT-384A, BWSGT-384B, BWSGT-389B, See APPENDIX A for data), three whole pumice sample and a single bulk tuff. Silica concentrations for the bulk pumice samples ranged from 71 wt% to 74 wt% (oxides normalized to 100% anhydrous; See Harker diagrams in APPENDIX A). REE and trace elements show considerable variability (**Figure 24**).

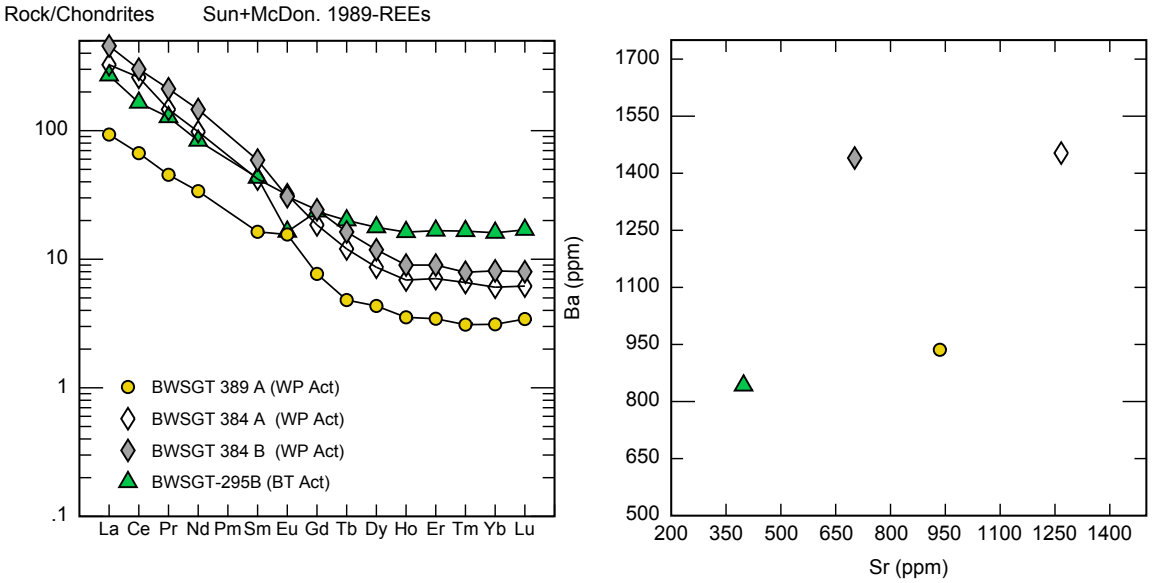

Figure 24: SGT-1 whole pumice geochemistry. Abbreviations in legend: WP = whole pumice, BT = bulk tuff

SGT1 Glass Compositions

Two end member glass compositions, 74 wt% SiO_2 and 77 wt% SiO_2, were distinguished within SGT-1 pumice (Samples BWSGT-384A and 384B). In some instances, these different types of glass are found within different pumice clasts; in others, they are found mingled in the same pumice. Glass (1) contains 74 wt% SiO_2, 340 ppm Sr, 720 ppm Ba, Eu/Eu* 0.7, and strong

HREE depletion. Glass (2) contains 77 wt% SiO_2, 100 ppm Sr, 210 ppm Ba, Eu/Eu* 0.7, and a

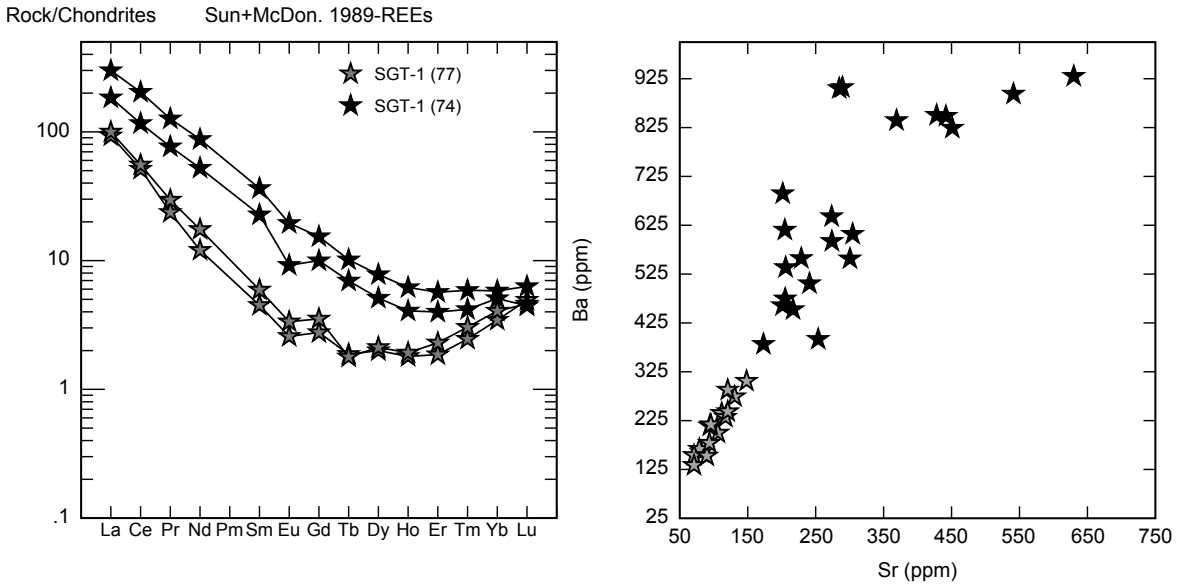

Figure 25: SGT-1 Glass Data. Left: Average REE pattern from SGT1 glasses. Right: Plot of Sr versus Ba (ppm) for all individual glass analyses from SGT1 glasses. Glass (1) = black stars and Glass (2) = gray stars.

strong depletion in both MREE and HREE (**Figure 25**). Zircon saturation thermometry suggests pre-eruptive storage temperatures of 790 and 720 ºC for glass (1) and (2) respectively (**Table 7**) (Watson and Harrison, 1983).

Table 7: Results from zircon saturation thermometry for SGT1.

Sample	Unit	M	$T_{Zr\text{-}Sat}$ (W&H)	$T_{Zr\text{-}Sat}$ (B)
BWSGT-384A (77)	SGT1	1.38	720	660
BWSGT-384A (74)	SGT1	1.39	790	740
W&H =Watson & Harrison 1983; B = Boehnke et al. 2013				

SGT1 Mineralogy

The mineral assemblage within unit 1 consists of Plagioclase>Sanidine>Biotite >Amphibole>Quartz + Titanite, Zircon, Apatite, Chevkinite, Magnetite, with quartz being rare to absent within the low silica rhyolite glass. The feldspars, plagioclase and sanidine, display

oscillatory zoning with multiple resorption surfaces (**Figure 27**). Sanidine in contact with both glasses, (1) and (2), contains BaO concentrations up to 5 wt%, but concentrations are generally

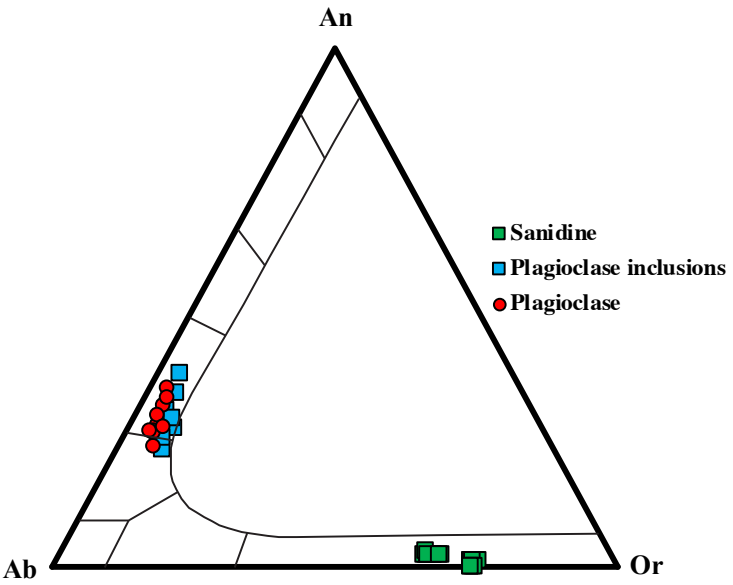

Figure 26: Sitgreaves Tuff unit-1 feldspar ternary. Individual plagioclase phenocryst (red circles) compositions combine core, intermediate, and rim zones. Plagioclase inclusions (blue squares) in sanidine are also shown. Also shown are individual sanidine phenocrysts (green squares).

lower, ~1.5 wt% BaO, for sanidine in contact with the more evolved glass (2). Plagioclase is found as individual, euhedral phenocrysts and as anhedral inclusions within sanidine grains (average plagioclase composition in glass (2): $Ca_{29}Na_{66}K_{5}$,; Average plagioclase composition in glass (1): $Ca_{23\text{-}31}Na_{66\text{-}70}K_{1}$ see **Figure 26**). Quartz is sparse within the HSR glass and is commonly subhedral in shape. Amphibole and biotite are present in subhedral to euhedral forms, with occasional biotite grains displaying reaction rims of amphibole in both glasses.

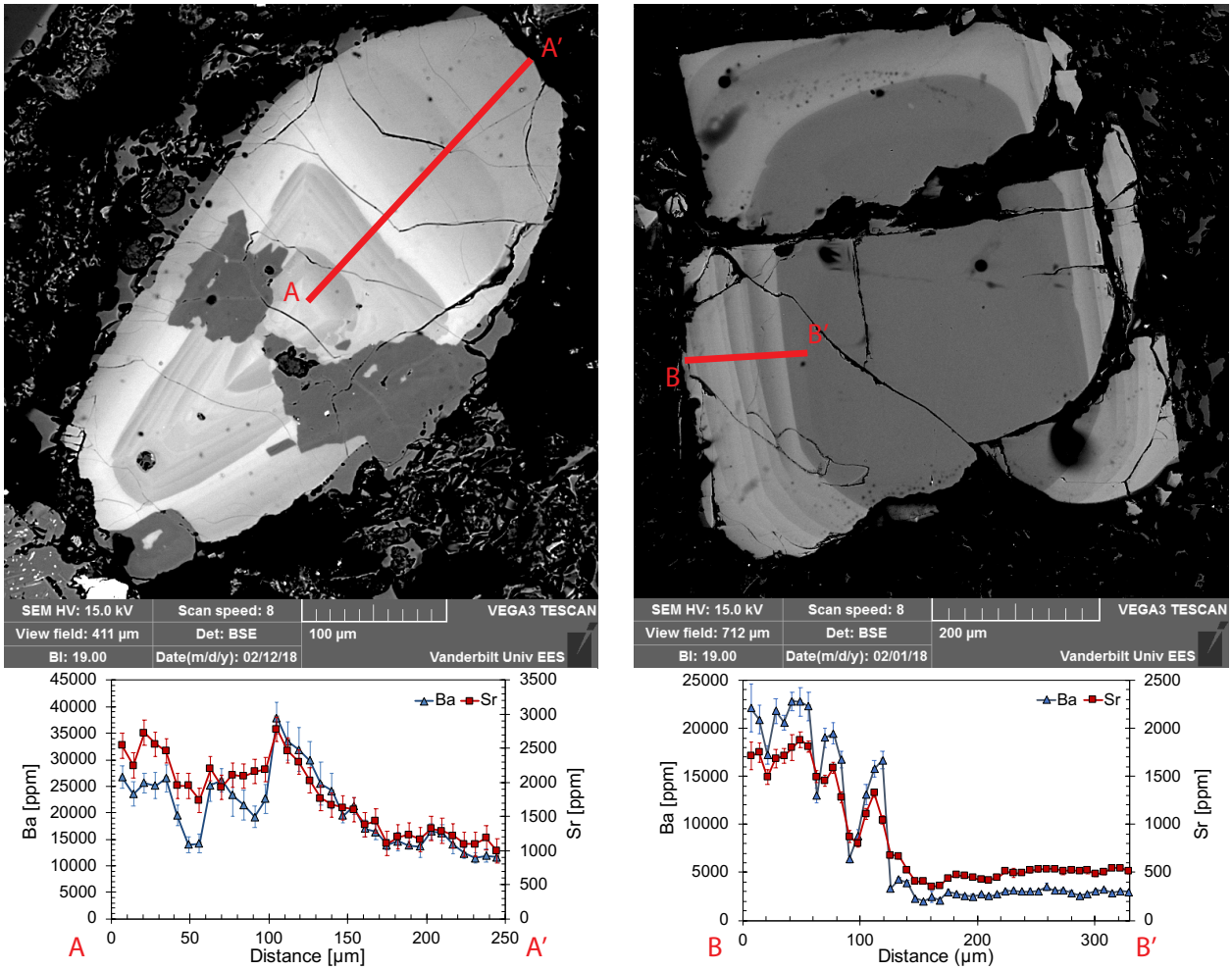

Figure 27: Core to rim transects from SGT-1 sanidine from glass (1). Geochemistry obtained by LA-ICPMS using a spot size of 7x50 µm. SGT1 sanidine contain elevated trace element concentrations (Ba and Sr shown) with respect to SGT2 sanidine.

Sitgreaves Tuff Unit 2 Geochemistry

SGT2 Whole Pumice/Rock

Five samples were sent out for geochemical characterization from SGT-2 (BWSGT-271B, BWSGT-296BA, BWSGT-284A, BWSGT-307B, BWSGT-271C1, See APPENDIX A for data), four whole pumice and a single whole lithic). Silica concentrations for the bulk pumice samples range from 76 wt% to 78 wt% (oxides normalized to 100%; See APPENDIX A for Harker diagrams) and 77 wt% for the spherulitic rhyolite lithic. REE and trace elements show limited

variability except in BWSGT-296B (**Figure 28**).

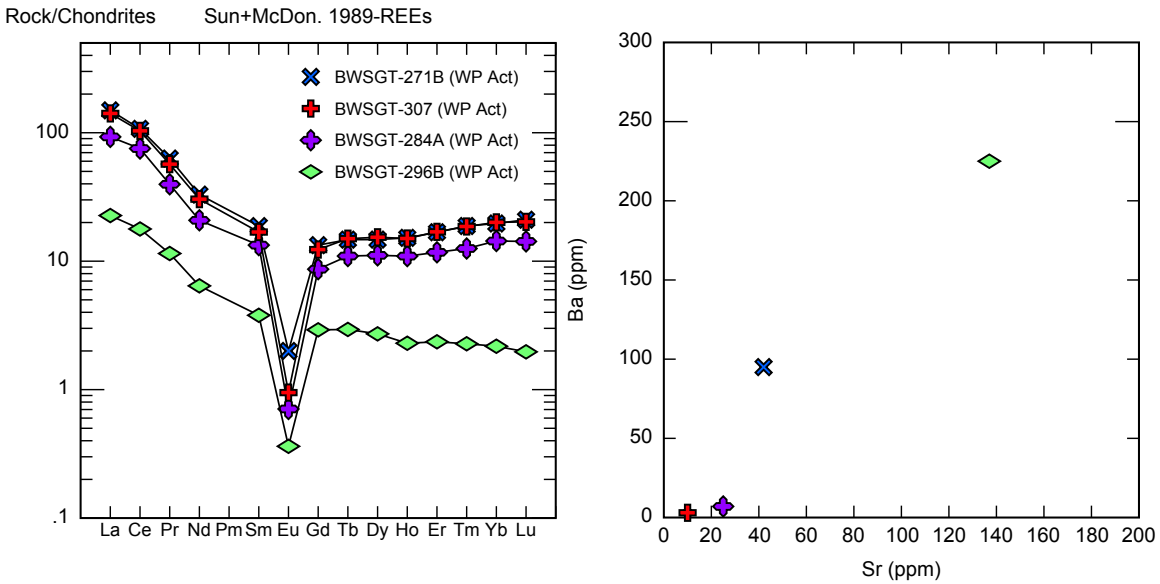

Figure 28: Whole pumice geochemistry SGT2 samples. WP ACT = whole pumice sample; analysis performed by ACT labs.

SGT2 Glass Compositions

A single highly evolved glass was found within all samples from SGT unit 2 glass analyses (SEM-EDS and LA-ICPMS). Glass (**Figure 29**) from this unit is composed of 77 wt% SiO_2, very low Sr (<4 ppm) and Ba (<4 ppm). REE patterns show an enrichment in HREE, a very subtle MREE depletion, and a large Eu anomaly (Eu/Eu* = 0.06). Zircon saturation thermometry (**Table 8**) using major element concentrations collected via SEM-EDS and Zr concentrations collected by LA-ICPMS suggest pre-eruptive storage temperatures of ~760 ºC using the calibration by Watson and Harrison (1983).

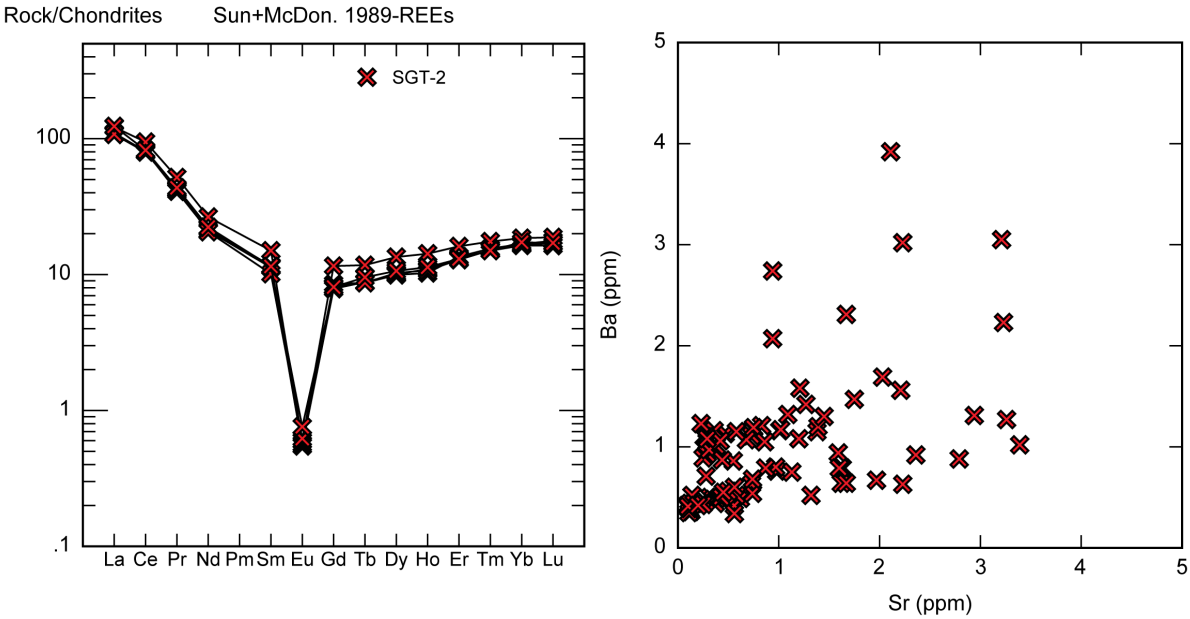

Figure 29: Plots of SGT-2 Glass data from 6 samples. REE patterns are nearly identical and Trace elements such as Ba and Sr show limited variability (few ppm) and extremely low concentrations.

Table 8: Results from Zircon saturation thermometry for SGT2

Sample	Unit	M	$T_{Zr\text{-}Sat}$ (W&H)	$T_{Zr\text{-}Sat}$ (B)
BWSGT-309B	SGT2	1.38	757	702
BWSGT-284A	SGT2	1.38	758	703
BWSGT-307	SGT2	1.33	761	708
BWSGT-271	SGT2	1.37	752	696
BWSGT-272D	SGT2	1.39	761	706
BWSGT-381	SGT2	1.32	769	717
W&H =Watson & Harrison 1983; B = Boehnke et al. 2013				

SGT2 Mineralogy

The mineral assemblage of Sitgreaves tuff unit 2 consists Sanidine-anorthoclase>Quartz>Amphibole >Biotite (rare)+ Magnetite, Titanite, Zircon, Apatite, Chevkinite. The single feldspar within SGT-2 contains patchy exsolution domains that are

distinctly more sodic than the host grain (**Figure 31**). Compositions span the gap between the sodic ($K_{22}Na_{72}Ca_4$) and potassic ($K_{51}Na_{48}Ca_1$) end members. Rare perthitic grains (host $K_{87}Na_{13}Ca_0$, with nearly pure albite ($K_1Na_{97}Ca_2$) exsolution lamellae) are also present (See APPENDIX B for annotated images of perthite and typical SGT2 anorthoclase-sanidine grains). Quartz is common, occurring as euhedral, doubly terminated grains. Amphibole and magnetite are sparse, and where found are commonly clustered with accessory minerals (titanite, zircon, apatite, chevkinite.

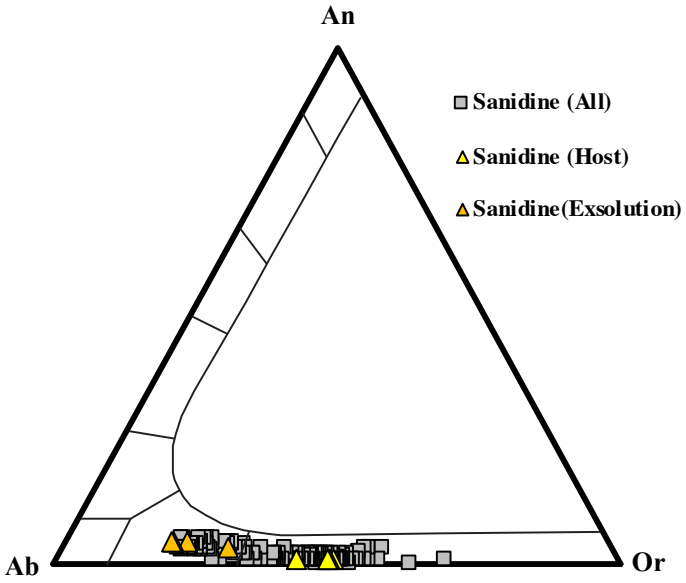

Figure 30: Sitgreaves Tuff unit 2 feldspar ternary. Example host grain (yellow triangle) and exsolution lamellae (orange triangle) plotted with all feldspar data from unit 2.

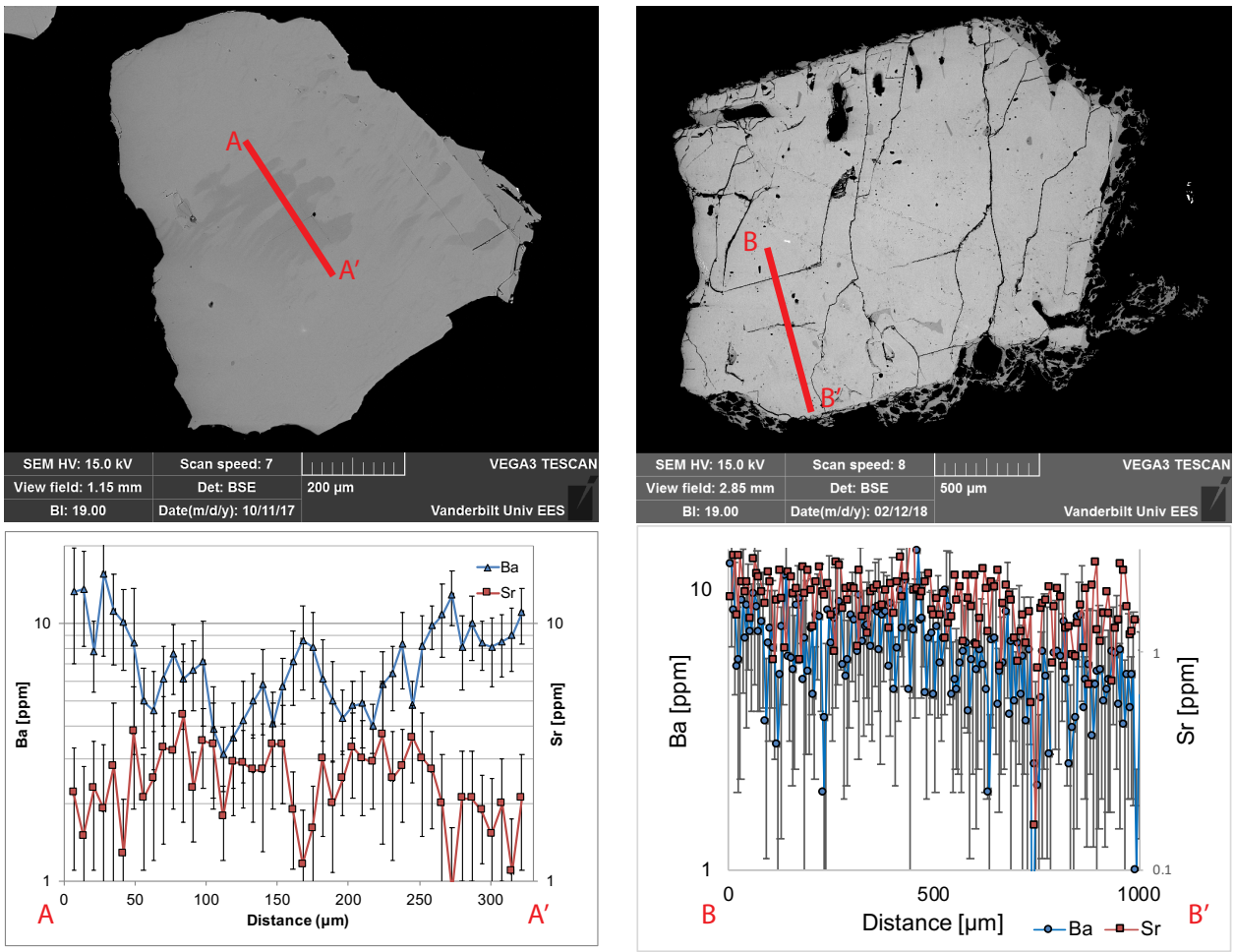

Figure 31: Core to rim transects from SGT-2 sanidine. SGT-2 feldspar contains distinct domains of more sodic and potassic composition. Trace element concentrations vary within each domain following expected elemental partitioning (e.g Sr higher in Na-fsp, Ba higher in K-fsp).

Geobarometry

Pressure estimates (**Figure 32**) derived from rhyolite-MELTS phase-equilibria geobarometry (Pamukcu et al., 2015)range from 300 to 50 MPa, with an average of 200 MPa for SGT-2 based on the equilibrium between melt (pumice glass compositions obtained via SEM-EDS), quartz, and one feldspar (Q1F). Pressure estimates for SGT-1 are shallower, ranging from 150 to 40 MPa using melt, quartz, and 1 feldspar equilibrium and 85 to 65 MPa using melt, quartz, and 2

feldspar equilibrium (Q2F).

Due to the limited number of successful results for SGT1 glasses using Rhyolite MELTS geobarometry, amphibole barometry (Mutch et al., 2016) was employed to further constrain the possible pre-eruptive storage conditions. The Al-in-hornblende geobarometer is applicable to rocks containing the mineral assemblage: amphibole + plagioclase + biotite + quartz + alkali feldspar + ilmenite/titanite + magnetite + apatite. SGT1 contains the appropriate assemblage for use with the barometer, SGT2 is missing plagioclase from the mineral assemblage and is employed with caution. Amphibole phenocrysts from both units were enclosed in high-silica rhyolite glass (e.g. glass (2) from SGT1) and appear to be in textural equilibrium with the melt.

Table 9: Results from Al-in-Amphibole barometry.

Unit	Analytical Method	Al wt%	Al^{apfu}	Mutch et al. (MPa)	Depth* (km)
SGT1	SEM-EDS	7.3	1.24	240	9
SGT2	SEM-EDS	5.2	0.89	160	6
*Depth determined assuming crustal density of 3.7 g/cm^3 Results are averages from multiple amphibole rim analyses from samples within each unit					

Pressure estimates for average rim compositions of amphibole (analyzed by SEM-EDS) within pumice from SGT1 (Glass 2) range from 210 to 350 MPa (~8 to 13 km depth) and from 130 to 200 MPa (~5 to 8 km depth)(**Table 9**).

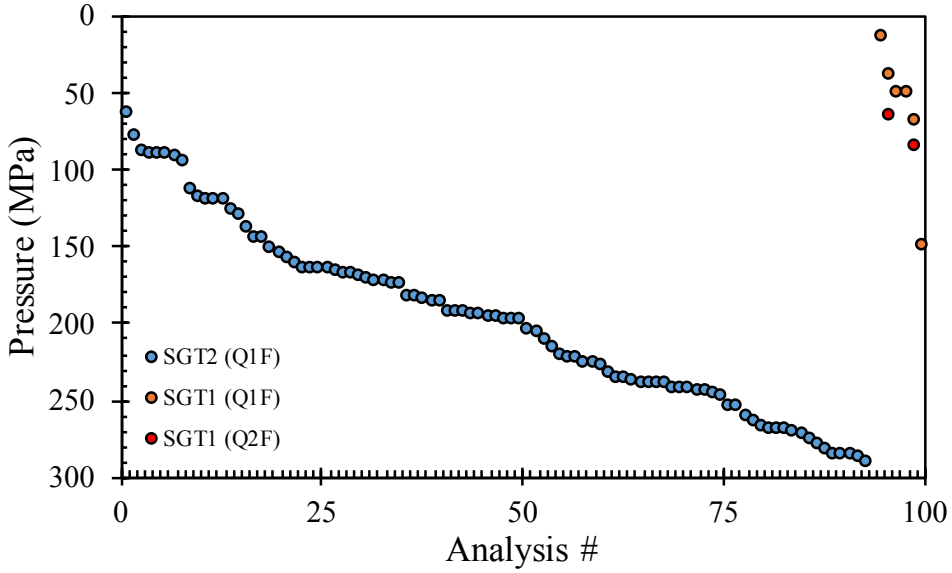

Figure 32: Results from rhyolite-MELTS Geobarometry using glass data from SGT-1 and SGT-2 obtained via SEM-EDS. Each point represents the results of one glass analysis run with rhyolite-MELTS geobarometer. Total of 94 pressure results for SGT2. Total of 6 successful geobarometer results out of 42 glass analyses from SGT1.

2.4 Discussion

Dynamic post supereruption magmatic system

Numerous studies (e.g. DePaolo and Daley, 2000; Feuerbach et al., 1993; Metcalf et al., 1995; Daley and Depaolo, 1992; Bachl et al., 2001; Falkner et al., 1995) have concluded that the juvenile mantle component supplying magmatism within the Colorado River Extensional Corridor is ancient, enriched lithospheric mantle [$\varepsilon_{Nd} < \sim -4$, $^{87}Sr/^{86}Sr > \sim 0.705$]. However, DePaolo and Daley (2000) also show that ε_{Nd} values for syn- to post-extension magmas record a change in mantle source from ancient, enriched lithospheric mantle to asthenospheric mantle, where ε_{Nd} is >0, due to lithospheric thinning. McDowell et al. 2016 use various isotopic ratios (ε_{Hf}, ε_{Nd}, $^{87}Sr/^{86}Sr$) to show that the post-supereruption parental magmas contain increasing

juvenile component with time, that is, lowest proportions of Paleoproterozoic crust (ε_{Nd} =-15 to -22 , $^{87}Sr/^{86}Sr$ = >0.710, up to 0.80 and higher; Bennett and DePaolo, 1987; Miller and Wooden, 1994)) and higher fractions of mantle-derived material (ε_{Hf} = -8.4 to -10, ε_{Nd} = -8.2 to -9.2, $^{87}Sr/^{86}Sr$ = 0.706 to 0.710).

Geobarometry

Pamukcu et al. (2015) demonstrated the effectiveness of the rhyolite-MELTS geobarometer in weeding out glass compositions affected by alteration and for constraining the broadly correct, unaltered, glass composition for a given melt using the quartz + two feldspar (Q2F) constraint. However, SGT unit 2 does not contain a second feldspar phase, thus, the only constraint that can be applied is quartz + one feldspar, which has a much larger uncertainty when compared to Q2F (Pamukcu et al., 2015; Gualda and Ghiorso, 2014). In light of these constraints, we interpret the results for Sitgreaves tuff glasses with caution. A negative slope on Na_2O vs K_2O diagrams (**Figure 33**) for glass analyses from the SGT2 hint at the occurrence of alteration (alkali exchange)(Zielinski et al., 1977; Scott, 1971; Lipman, 1965). The effects of the alkali exchange (depletion in Na_2O, complementary enrichment in K_2O) in glass compositions used in rhyolite-MELTS geobarometry are apparent in **Figure 34**. Pressure is correlated with total alkali content with shallower pressures returned at lower ($Na_2O + K_2O$) values. Based on the findings of previous studies (Pamukcu et al. 2015 and references therein), this would suggest that the pressures returned for glasses with higher Na_2O and lower K_2O should be considered. To further constrain the total alkali content of the original, unaltered melt, we used melt inclusions compositions found in titanite and the coexisting pumice glass in which the titanite was hosted for one sample from SGT2 (BWSGT-381). Titanite-hosted melt inclusions were chosen for

multiple reasons: (1) titanite is a late saturating mineral in general and (2) our data suggest that titanite saturation within SGT2 melt was delayed (See discussion below). Compositions of the melt inclusions overlap for most major elements, excluding TiO_2, Na_2O, and K_2O. The slightly higher values for TiO_2 and CaO are attributed to secondary fluorescence, and the lower K_2O and higher Na_2O values are likely due to the buffering effect of the mineral during post-eruption alteration processes (See APPENDIX C for data). Therefore, the titanite-hosted melt inclusion glass data may provide guidance for inferring melt compositions of the alkalis prior to post-eruption alteration. In a plot of Na_2O vs K_2O the effects of post-eruption alteration are apparent in SGT2 glass, where a negative slope is indicative of alteration (**Figure 33**) (Lipman, 1965; Pamukcu et al., 2015). Conversely, titanite hosted melt inclusion glass analyses do not contain any trend on a plot of Na_2O vs K_2O (**Figure 33**). The results suggest that if the titanite hosted melt inclusion glass is wholly unaltered and more representative of the near-eutectic to eutectic melt from which the titanite was in equilibrium, most SGT2 glasses have experienced some post-eruption alteration. The effect of alteration can therefore be expected to yield systematically higher pressures than those of unaltered glasses under the Q1F constraint (**Figure 34** and **Figure 35**). This results in an average pressure of ~130 MPa (2σ = +/- 13 MPa; n=17) for the titanite melt inclusion data and ~185 MPa (2σ = +/- 20 MPa; n=17) for the pumice glass analyses. The average pressure retuned from the melt inclusions and glass fall within the range suggested by Al-in-amphibole barometry (Mutch et al., 2016).

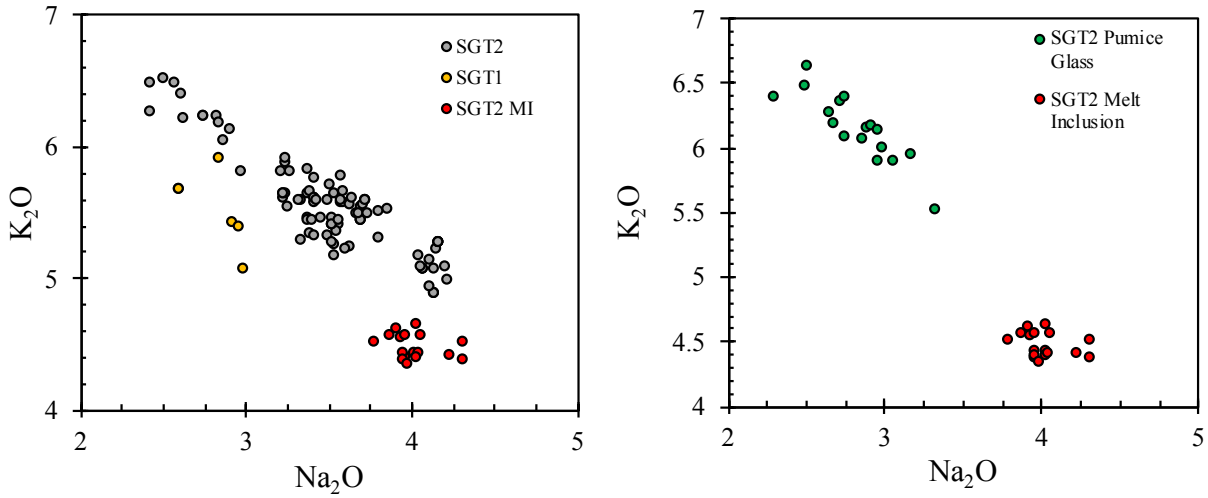

Figure 33: Na_2O vs K_2O for SGT1, SGT2 glass data. Analyses from pumice glass and melt inclusions in titanite from SGT2. (Left) Negative correlation between Na and K values suggest that many of the SGT glasses suffered from post-eruptive alkali exchange. (Right) Titanite hosted melt inclusion analyses and pumice glass data from glass adhering to titanite crystals from a single sample (BWSGT-381). Melt inclusion data do not contain a negative trend, suggesting titanite crystal may have limited post-eruptive alkali exchange.

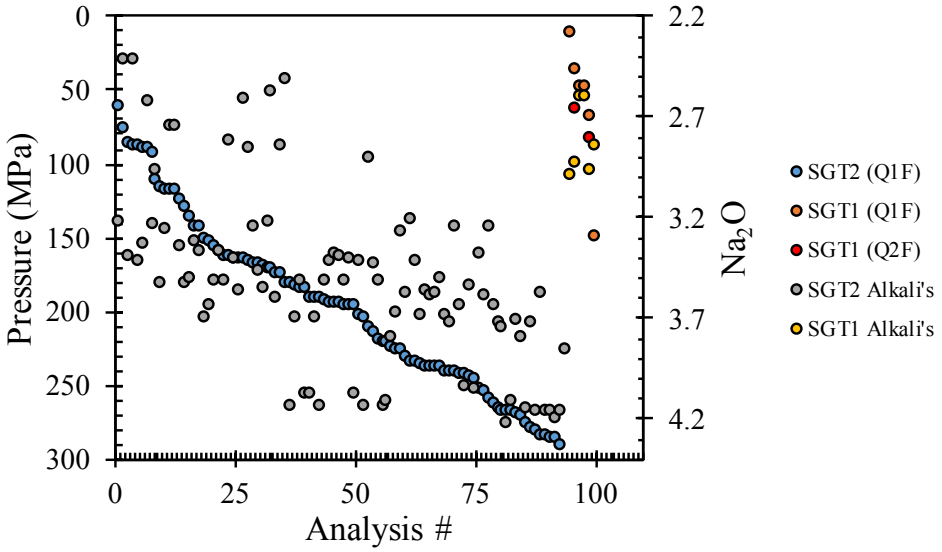

Figure 34: Results from rhyolite-MELTS geobarometry plotted against Na_2O. glass analyses (SEM-EDS) from SGT1 and SGT2 plotted along with Na_2O content in the glass from each geobarometry model. Blue circles are pressures returned from Rhyolite MELTS (Q1F) for SGT2. Gray circles are Na_2O content for SGT2 glasses for each corresponding pressure point.

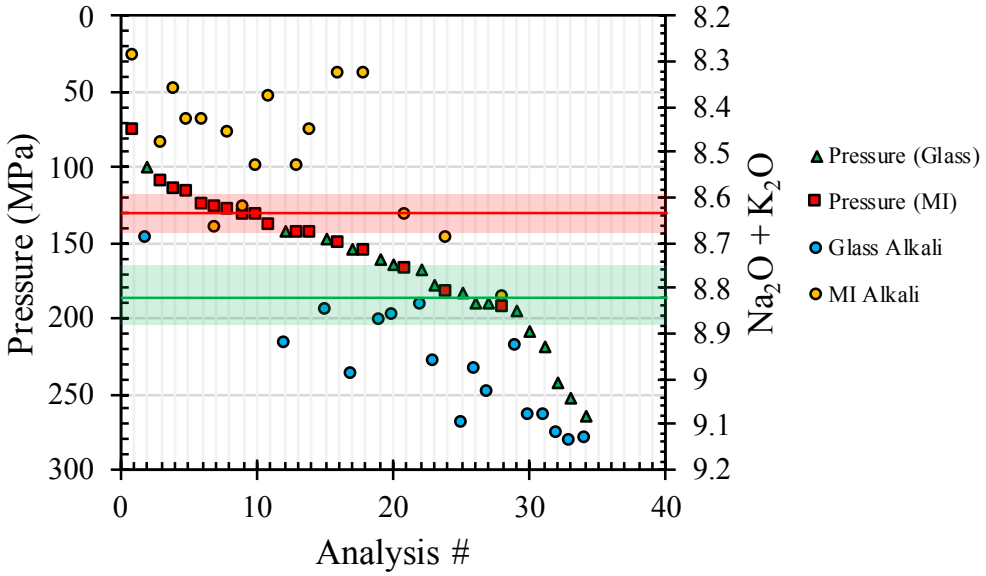

Figure 35: Results from rhyolite-MELTS geobarometry for select glass data, in rank order, using glass analyses (SEM-EDS) from SGT2 glass and melt inclusions (hosted within titanite) from sample BWSGT-381, plotted along with total alkali content in the glass show similar trends. Data from melt inclusions have consistently lower total alkali's and lower pressures. Solid bars mark the average pressure for each set of glass data and shaded regions are the 2σ confidence intervals around each mean.

Phase chemistry (SGT1 vs SGT2)

Dynamic post-supereruption magmatic environments were present within the SBMVC. The presence of two feldspars, sanidine and plagioclase within SGT-1 pumice (**Figure 26**), suggests that subsolvus crystallization conditions dominated during the genesis of the rhyolitic melts for a period of ~1.3 Ma (~18.8 Ma Peach Spring Tuff to ~17.46 Ma Sitgreaves Tuff unit 2) following the cataclysmic PST eruption. Within a ~240 ka period subsolvus crystallization conditions transitioned to hypersolvus conditions: in contrast to SGT-1, SGT-2 contains only one feldspar, sanidine-anorthoclase (**Figure 30**). Other units, notably the early post-supereruption Cottonwood lavas of Ransom (1923) and Thorson (1971), corroborate this transition. Within the succession of the 6 different flows that comprise the Cottonwood lava sequence there is a decrease in the amount of plagioclase and an increase in the abundance of sanidine with time (Thorson, 1971).

The differences in composition and texture of the sanidine between SGT units 1 and 2 suggest the change in solvus conditions was accompanied by transition from open to closed system processes. Oscillatory zoning and numerous resorption surfaces within sanidine from SGT1 suggest that the crystals were in contact with new, hotter, magmas enriched in Ba. Multiple types of sanidine phenocrysts, distinguished by normal or reverse zoning, suggest that phenocrysts were entrained within the replenishing melts (**Figure 27**). Previous researchers have documented similar compositional differences in other locations and suggest that the different zoning profiles represent multiple different magma bodies/pods within the magma plumbing system (Kahl et al., 2011, 2013). We take the SGT1 sanidine profiles to reflect similar architecture within the system that produced SGT1.

Conversely, sanidine phenocrysts from SGT2 contain blebby zones of more sodic composition which we interpret to be exsolution domains due to their arrangement, commonly subparallel zones of more Na-rich feldspar within a host of sanidine (**Figure 31**). The exsolution domains contain trace element abundances that are consistent with expected elemental partitioning, that is, within the sodic domains Sr increases and Ba decreases and within the potassic domains Ba increases and Sr decreases.

Glass chemistry (SGT1 vs SGT2)

Bachmann and Bergantz (2008) review magma petrogenesis and the relationship between the melt geochemistry and the environments from which the magmas were derived. They argue that geochemical characteristics imprinted on the melt are a direct result of the mechanism through which mantle melting, and subsequent mush column dynamics, including phase chemistry, occurs. For example, melting through adiabatic decompression, which occurs mostly at mid-ocean ridges and continental rifts-hotspots, will yield extracted melts that carry a hot-dry-reduced signature (Bachmann and Bergantz, 2008). Conversely, melting of the mantle through the addition of volatiles, which occurs mostly at convergent margins, will generate cold-wet-oxidized signatures. In the following paragraphs we interpret the glass geochemistry in the context of Bachmann and Bergantz (2008).

Glass geochemistry from the Sitgreaves tuff provides further support for conditions suggested by mineral chemistry and modal abundance of characteristic minerals within the SBMVC. In SGT1, REE patterns suggest dominance by amphibole fractionation for glass SGT1(74) and titanite fractionation for glass SGT1(77) (**Figure 36)**. The presence of a small Eu-anomaly is consistent with the suggestion that SGT1 melts evolved in a relatively high fO_2

environment. Previous research (e.g.. Drake and Weill, 1975; Wilke and Behrens, 1999) has shown that fO_2 is strongly correlated with the distribution coefficient of Eu between melts and minerals. Therefore, hot-reducing conditions are expected to accompany low *f*O2, and cool-wet conditions with high fO_2. The change in shape of the REE patterns between SGT1 glass (1) and (2) strongly suggests fractionation of titanite, with its high Kd's for all REE, especially middle REEs. In addition to the REE data, the presence of abundant amphibole, biotite, and titanite

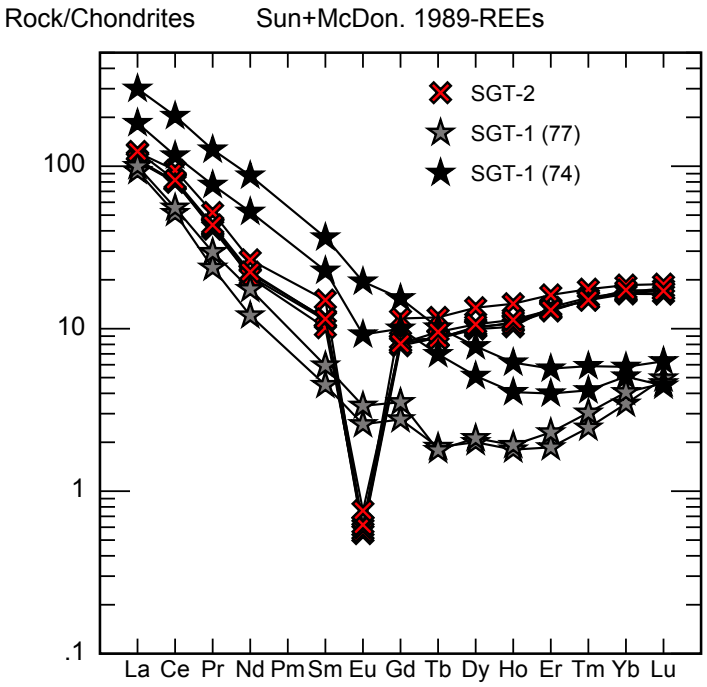

Figure 36: REE patterns for SGT-1 and SGT-2 glasses show the effects of progressive crystallization under different conditions, where minerals such as titanite and feldspar control the abundances of specific REEs in the melt (now glass).

phenocrysts, and the presence of two feldspars, lends further support toward magma evolution under relatively wet, high fO_2 and cool conditions.

In SGT2, REE patterns show the effects of extensive feldspar fractionation (large negative Eu-anomaly) and delayed titanite and amphibole saturation as suggested by the

presence of both minerals in SGT2 pumice. Colombini et al. (2011) and Padilla & Gualda (2016) show that middle-REE have a high affinity to partition into both titanite and amphibole. Therefore, if these phases saturated in SGT2 melt earlier there would be a much greater depletion visible in the middle-REEs. The extremely low abundance of trace elements such as Ba and Sr provide further evidence for fractional crystallization of feldspars. The presence of both amphibole and titanite within SGT2 pumice along with its highly vesiculated nature suggest that the melt, prior to eruption had a high fO_2. This is not unique in that fractionated melts from hot-dry-reducing environments can saturate in phases that are more typical of wet and oxidizing conditions when they concentrate water and reach lower temperatures as they approach their solidi. Furthermore, simple modeling using Rhyolite MELTS, with unconstrained fO_2, shows that fO_2 will systematically increase with melt evolution. Therefore, we interpret the trace element signatures (**Figure 36**) to be the result of differentiation of the SGT2 melt under initially hot-dry-reducing conditions where Eu^{2+} is more abundant compared to oxidizing environments, in which more muted Eu anomalies are common (Drake and Weill, 1975; Wilke and Behrens, 1999).

What is the cause of the transition from cool-wet to hot-dry magmatism? Faulds et al. (2001) suggest that magmatism within the Oatman, AZ area began around 19.5 Ma (**Figure 20**; McDowell et al., 2014) and that the magmatic front stalled within the region at ~19 Ma, as evidenced by the thick intermediate to felsic lavas within this area. Following the passage of the northward migrating magmatic front, east-west extension commenced, typically within the range of 1-4 Ma within the extensional corridor as a whole (Faulds et al., 1999, 2001). The Sitgreaves tuff units fall within this time frame for the onset of extension.

The timing of extension coupled with the assumption that elemental signatures are intrinsic to conditions in magma sources suggests that the Sitgreaves Tuff units 1 and 2 may bracket the transition from cool-wet-oxidizing to hot-dry-reducing conditions. This may reflect the onset of hotter, more reducing magmas entering the crustal magmatic system within the SBMVC and rejuvenating some of the near-solidus eutectic melts during the waning stages of the silicic magmatic system. The presence of tholeiitic olivine basalt sequence that caps post PST silicic lavas and tuffs (Smith et al., 2016) appears to document the eventual appearance of hot-dry-reducing juvenile magmas at the surface (**Figure 17**).

Deering and Bachmann (2010) demonstrate the applicability of trace element ratios to discriminate the conditions of crystallization, noting that low Zr concentration, in addition to the

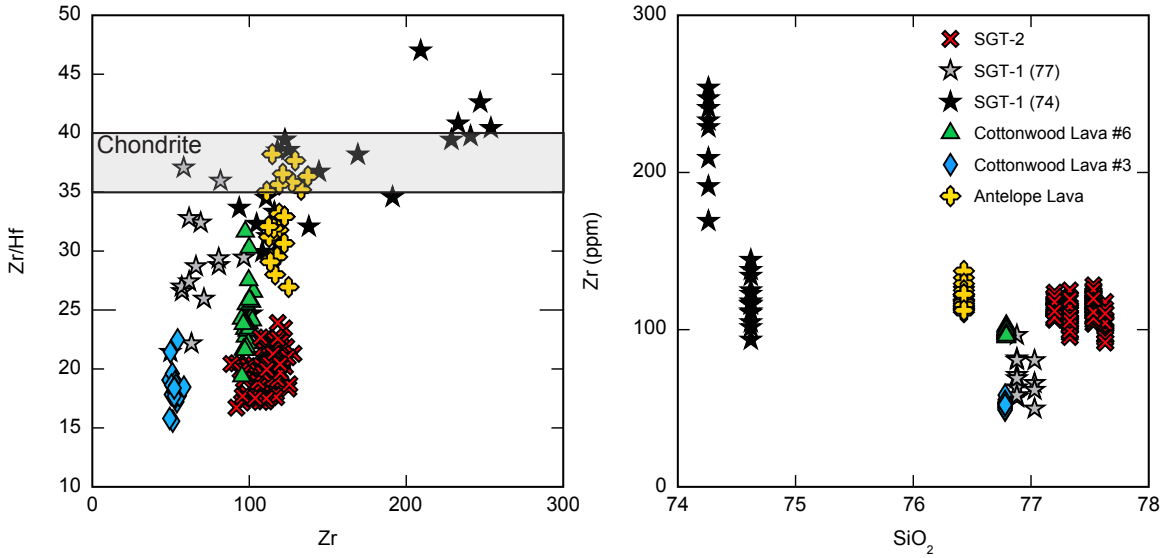

Figure 37: Zr/Hf vs Zr and Zr vs SiO_2 for post-supereruption units shows that all other high silica rhyolite glasses from the post-supereruption volcanic sequence contain elevated Zr/Hf for similar values of Zr when compared to SGT2. Similar results are found when plotting Zr versus SiO_2 (Right) where SGT2 contains elevated Zr concentrations compared to units with similar SiO_2 values .

Zr/Hf ratio, may be one of the more reliable indicators melts extracted form cumulates in arc

settings. Claiborne et al. (2006) showed that low Zr/Hf is a fingerprint of melt that has experienced extensive fractional crystallization of zircon. Although the cumulates from which these melts were extracted are not exposed, **Figure 37** highlights the difference between Sitgreaves tuff unit 2 and SGT1 and the other post supereruption units, which we interpret to be part of the cool-wet-oxidizing trend, where Zr concentration is lower at higher SiO_2 values.

Zr/Sr has also been proposed as an additional parameter that can distinguish hot from cool magmatic environments (Miller et al., 2014). Specifically, Zr/Sr tracks the saturation and growth histories of the zircon and feldspar. Miller et al. (2014) show that melts from high temperature, "hot", environments typically have Zr/Sr values >>2 at 70 wt% SiO_2 and melts from lower temperature, "cool", environments have Zr/Sr values of <<2 at 70 wt% SiO_2. At higher SiO_2 concentrations Zr/Sr continues to rise in both types of systems (**Figure 38**).

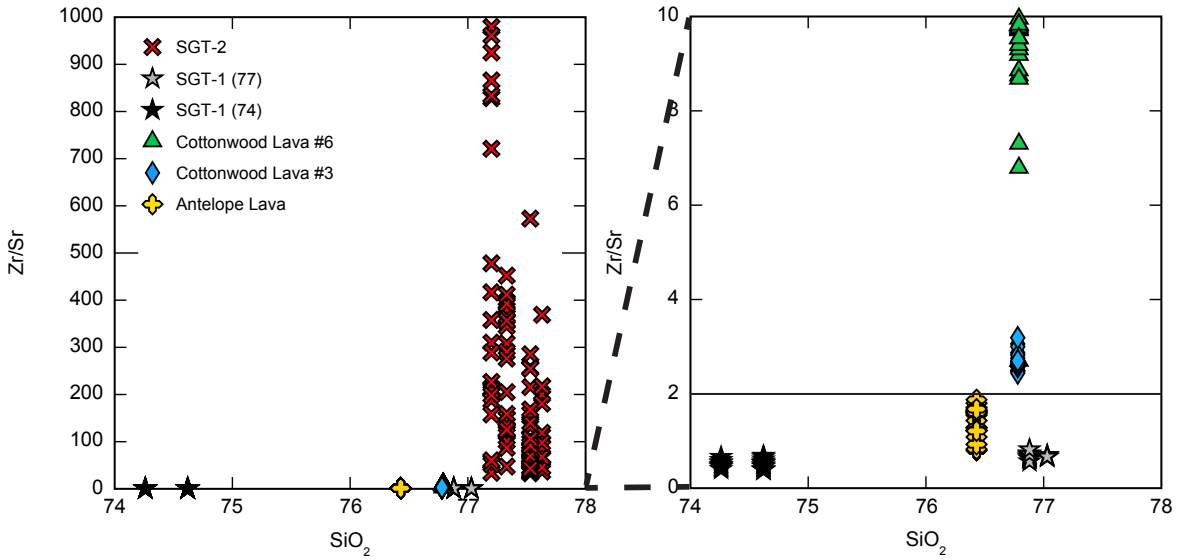

Figure 38: Zr/Sr versus SiO_2 for glass data from the post-supereruption volcanic sequence compiled by this study and the Antelope lava data from Schlaerth et al. (2016). Average Zr/Sr for the SGT2 is 278 (2σ = 59).

Discrimination of the two environments can become difficult at lower Sr concentrations. However, the results from the post supereruption silicic glasses are clear, with even the most

evolved glasses (>76 wt% SiO_2) having distinctly lower Zr/Sr (<10) values than those of the SGT2. Whole rock values (See APPENDIX A) display similar trends where SGT2 Zr/Sr is greater than or equal to a factor of 6 higher than other post-supereruption units.

Table 10: Results from Zircon saturation thermometry for all post-supereruption glasses.

Sample	Unit	M	$T_{Zr\text{-}Sat}$ (W&H)	$T_{Zr\text{-}Sat}$ (B)
BWSGT-309B	SGT2	1.38	757	702
BWSGT-284A	SGT2	1.38	758	703
BWSGT-307	SGT2	1.33	761	708
BWSGT-271	SGT2	1.37	752	696
BWSGT-272D	SGT2	1.39	761	706
BWSGT-381	SGT2	1.32	769	717
BWSGT-384A (77)	SGT1	1.38	722	662
BWSGT-384A (74)	SGT1	1.39	789	739
CLW-6	CWL #6	1.40	749	692
CLW-1	CWL #3	1.35	703	642
ALHS-19	ANL	1.27	774	725
CWL = Cottonwood Lava, ANL = Antelope Lava (Schlaerth et al., 2016)				
W&H =Watson & Harrison 1983; B = Boehnke et al. 2013				

Pearce et al. (1984) proposed multiple trace element ratio combinations to effectively discriminate between the four main tectonic settings where granite form: ocean ridge granites (ORG), volcanic arc granites (VAG), within plate granites (WPG) and collision granites (COLG). The applicability of these diagrams extends not just to granites but also to their extrusive counterparts, rhyolites. Using the available glass data from the post-supereruption volcanics the Pearce et al. (1984) tectonic discrimination diagrams also suggest a different magmatic lineage for SGT2, when compared to the earlier (older) units. The Y vs Nb diagram

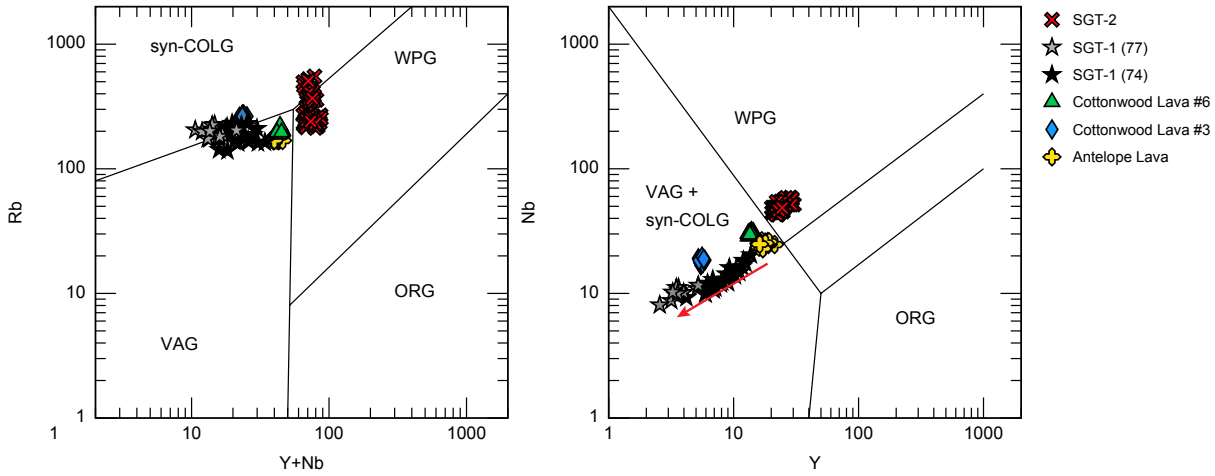

Figure 39: Pearce tectonic discrimination diagrams for post supereruption glasses. (Right) Rb versus Y+ Nb shows the effects of amphibole and titanite crystallization. Rb is a useful tracker of melt evolution and remains relatively incompatible with progressive crystallization, thus, more evolved melts would plot with greater Rb values. Y+Nb tracks the onset of amphibole crystallization (and titanite); upon saturation, amphibole and titanite prevent increases in Y. (Left) Y versus Nb. SGT1 glasses along with Cottonwood Lava # 3, #6, and the Antelope Lava again plot within the VAG field. SGT2 plots within the WPG field, suggesting a different magmatic lineage when compared to the other post-supereruption units. Red arrow points in the direction of apparent melt evolution from SGT1 glass (1) to glass (2). See APPENDIX F for average glass data from each unit.

(**Figure 39**) shows that SGT2 glasses contains higher amounts of Nb and Y than all other units. Low Nb and Y concentrations in all glasses except SGT2 suggest that melts saturated in amphibole and titanite early, further suggestive of hydrous, high fO_2 crystallization pathways for

early post supereruption volcanics. Conversely, high Nb and Y concentrations in the SGT2 glass suggest a magmatic lineage dominated by anhydrous crystallization.

Multiple methods of discriminating between cool-wet-oxidizing and hot-dry-reducing magmatic environments suggest that the SGT2 magmas formed through a different evolutionary pathway when compared to earlier post-caldera forming silicic lavas. Thompson et al. (1986) documents similar complexity within post-caldera forming volcanics where the phase assemblage of lavas fluctuates between hypersolvus (sanidine) and subsolvus (plagioclase + sanidine only) conditions. Similarly, Eddy et al. (2016) shows that both hypersolvus and subsolvus magmatic conditions can exist within the same magmatic reservoir. In this instance, the post supereruption magmas represent tapping of those different parts of the system.

Previous research into Southern Black Mountain magmatism suggests that there was a large thermal flux of material into the crust that acted as a thermal primer (Flansburg, 2015; McDowell et al., 2016, 2014). Some of this material erupted, as evidenced by the hot-pre-supereruption trachyte lavas and minor mafic lavas. Some of this material must have undergone assimilation-fractional crystallization to form the large volume of silicic magma erupted during the PST supereruption. Discrimination of the high-silica rhyolite glasses using the methods above suggests the magmas evolved under hot-dry-reducing conditions similar to those of the Snake River Plain volcanics (Frazier, 2013). This pattern could suggest that the silicic volcanics following the supereruption were the result of the much cooler, less thermally insulated crust and development of a hydrothermally active system following the evacuation of >1000 km^3 of magma . If so, then the hot-dry magmatic lineage suggested by SGT2 magmas could hint at the presence of a new batch of hotter material into the crust.

2.5 Conclusions

In the period following the 18.8 Ma PST supereruption the evolutionary pathways through which magmas evolved appear to have undergone a transition from cool-wet-oxidizing to hot-dry-reducing within the Southern Black Mountain Volcanic Center. The ignimbrite units that compose the Sitgreaves Tuff document the following changes within the magmatic system over a 240 ka period:

- Feldspar composition and abundance suggest a transition from subsolvus to hypersolvus rhyolites
- Trace element and phase assemblage suggest that the magmatic system transitioned from predominantly cool-wet-oxidizing to hot-dry-reducing conditions
- The flux of new, more juvenile material decreased with time, as evidenced by the decrease in open system indicators such as mafic enclaves, and disequilibrium textures. However, mafic input into the system may have started to ramp up again as indicated by the hot-dry-reducing conditions suggested by SGT2 geochemistry.
- Based on the results of amphibole geobarometry storage pressures decreased subtly with time.
- These changes could be the result of changing tectonic conditions, in particular the onset of rifting in the region.

The results of this study in the broad context of this thesis pose the question of whether the post supereruption volcanic sequence could be representative of the waning stages of a magma

reservoir as a whole.

REFERENCES

Bachl, C.A., Miller, C.F., Miller, J.S., and Faulds, J.E., 2001, Construction of a pluton: Evidence from an exposed cross section of the Searchlight pluton, Eldorado Mountains, Nevada: Geological Society of America Bulletin, v. 113, p. 1213–7606.

Bachmann, O., and Bergantz, G.W., 2008, Rhyolites and their source mushes across tectonic settings: Journal of Petrology, v. 49, p. 2277–2285, doi: 10.1093/petrology/egn068.

Bachmann, O., Dungan, M.A., and Bussy, F., 2005a, Insights into shallow magmatic processes in large silicic magma bodies: The trace element record in the Fish Canyon magma body, Colorado: Contributions to Mineralogy and Petrology, v. 149, p. 338–349, doi: 10.1007/s00410-005-0653-z.

Bachmann, O., Dungan, M.A., and Bussy, F., 2005b, Insights into shallow magmatic processes in large silicic magma bodies: The trace element record in the Fish Canyon magma body, Colorado: Contributions to Mineralogy and Petrology, doi: 10.1007/s00410-005-0653-z.

Bazar, D., Miller, J., Miller, C., Dodge, M., Hodge, K., and Faulds, J., 2006, Eruption of deep mushy magma from the Searchlight magma system, southern Nevada (USA): a crystal size distribution and geochemical analysis:

Bennett, V.C., and Depaolo, D.J., 1987, Proterozoic crustal history of the western United States as determined by neodymium isotopic mapping: Geological Society of America Bulletin, v. 99, p. 674–685.

Best, M.G., and Christiansen, E.H., 1997, Origin of broken crystals in ash-flow tuffs: Geological Society of America Bulletin, v. 109, p. 63–73, doi: 10.1130/0016-7606(1997)109<0063.

Blundy, J., and Wood, B., 2003, Partitioning of trace elements between crystals and melts: Earth and Planetary Science Letters, v. 210, p. 383–397, doi: 10.1016/S0012-821X(03)00129-8.

Blundy, J., and Wood, B., 1994, Prediction of crystal--melt partition coefficients from elastic moduli: Nature, v. 372, p. 452.

Boehnke, P., Watson, E.B., Trail, D., Harrison, T.M., and Schmitt, A.K., 2013, Zircon saturation re-revisited: Chemical Geology, v. 351, p. 324–334, doi: 10.1016/j.chemgeo.2013.05.028.

Brice, J.C., 1975, Some thermodynamic aspects of the growth of strained crystals: Journal of Crystal Growth, v. 28, p. 249–253, doi: 10.1016/0022-0248(75)90241-9.

Buesch, D.C., 1992, Incorporation and redistribution of locally derived lithic fragments within a pyroclastic flow: Geological Society of America Bulletin, v. 104, p. 1193–7606.

Buesch, D.C., and Valentine, G.A., 1986, Peach Springs Tuff and Volcanic Stratigraphy of the Southern Cerbat Mountains, Kingman, Arizona: Geological Society of America, Cordilleran Section, Field Trip Guidebook,.

Claiborne, L.L., Miller, C.F., Gualda, G.A.R., Carley, T.L., Covey, A.K., Wooden, J.L., and Fleming, M.A., 2017, Zircon as magma monitor: Robust, temperature-dependent partition coefficients from glass and zircon surface and rim measurements from natural systems, *in* Micro-Geochronology: Visualizing Deep Time, p. 3–33, doi: 10.1002/9781119227250.ch1.

Claiborne, L.L., Miller, C.F., Walker, B.A., Wooden, J.L., Mazdab, F.K., and Bea, F., 2006, Tracking magmatic processes through Zr/Hf ratios in rocks and Hf and Ti zoning in zircons: An example from the Spirit Mountain batholith, Nevada: Mineralogical Magazine, v. 70, p. 517–543, doi: 10.1180/0026461067050348.

Claiborne, L.L., Miller, C.F., Wooden, J.L., and Rejuvenation, Á.F.Á., 2010, Trace element composition of igneous zircon : a thermal and compositional record of the accumulation and evolution of a large silicic batholith , Spirit Mountain , Nevada: , p. 511–531, doi: 10.1007/s00410-010-0491-5.

Colombini, L.L., 2009, Mid-Miocene Rhyolite Sequence, Highland Range, NV: Record of Magma Evolution and Eruption From the Searchlight Pluton Magma Chamber: Vanderbilt University, 1–126 p.

Colombini, L.L., Miller, C.F., Gualda, G.A.R., Wooden, J.L., and Miller, J.S., 2011, Sphene and zircon in the Highland Range volcanic sequence (Miocene, southern Nevada, USA): elemental partitioning, phase relations, and influence on evolution of silicic magma: Mineralogy and Petrology, v. 102, p. 29–708.

Coombs, D.S., Nakamura, Y., and Vuagnat, M., 1976, Pumpellyite-actinolite facies schists of the taveyanne formation near loèche, valais, Switzerland: Journal of Petrology, v. 17, p. 440–471, doi: 10.1093/petrology/17.4.440.

Daley, E.E., and Depaolo, D.J., 1992, Isotopic evidence for lithospheric thinning during extension : Southeastern Great Basin: Geology, v. 20, p. 104–108.

Daly, R.A.., 1911, The Nature of Volcanic Action: Proceedings of the American Academy of

Arts and Sciences, v. 47, p. 47–122.

Deer, W.A., Howie, R.A., and Zussman, J.%@ 1897799888, 1982, Rock-Forming Minerals: Orthosilicates, Volume 1A: Geological Society of London.

Deering, C.D., and Bachmann, O., 2010, Trace element indicators of crystal accumulation in silicic igneous rocks: Earth and Planetary Science Letters, v. 297, p. 324–331, doi: 10.1016/j.epsl.2010.06.034.

DePaolo, D.J., and Daley, E.E., 2000, Neodymium isotopes in basalts of the southwest basin and range and lithospheric thinning during continental extension: Chemical Geology, v. 169, p. 157–2541.

Drake, M.J., and Weill, D.F., 1975, Partition of Sr, Ba, Ca, Y, Eu2+, Eu3+, and other REE between plagioclase feldspar and magmatic liquid: an experimental study: Geochimica et Cosmochimica Acta, v. 39, p. 689–712, doi: 10.1016/0016-7037(75)90011-3.

Eddy, M.P., Bowring, S.A., Miller, R.B., and Tepper, J.H., 2016, Rapid assembly and crystallization of a fossil large-volume silicic magma chamber: Geology, v. 44, p. 331–334, doi: 10.1130/G37631.1.

Falkner, C.M., Miller, C.F., Wooden, L., and Heizler, M., 1995, Petrogenesis and tectonic significance of the calc-alkaline, bimodal Aztec Wash pluton, Eldorado Mountains, Colorado River extensional corridor: Journal of Geophysical Research, v. 100, p. 10453–10467.

Faulds, J.E., Feuerbach, D.L., Miller, C.F., and Smith, E.I., 1999, Cenozoic Evolution of the Northern Colorado River Exten- Sional Corridor , Southern Nevada and Northwest Arizona: , p. 239–271.

Faulds, J.E., Feuerbach, D.L., Miller, C.F., and Smith, E.I., 2001, Cenozoic evolution of the northern Colorado River extensional corridor, southern Nevada and northwest Arizona:

Faulds, J.E., Olson, E.L., Harlan, S.S., and Mcintosh, W.C., 2002, Miocene extension and fault-related folding in the Highland Range , southern Nevada : a three-dimensional perspective: v. 24.

Ferguson, C.A., 2016, The Peach Spring Tuff, its source caldera, and implications for structural geology of the Colorado River Extensional Corridor: Arizona Geological Society 2016 Fall Field Trip, p. 29.

Ferguson, C.A., McIntosh, W.C., and Miller, C.F., 2013, Silver Creek caldera-The tectonically dismembered source of the Peach Spring Tuff: Geology, v. 41, p. 3–6, doi: 10.1130/G33551.1.

Feuerbach, D.L., Smith, E.I., Walker, J.D., and Tangeman, J.A., 1993, The role of the mantle during crustal extension: Constraints from geochemistry of volcanic rocks in the Lake Mead area, Nevada and Arizona: Geological Society of America Bulletin, v. 105, p. 1561–7606.

Flansburg, M.E., 2015, Priming for Supereruption: The Hot Pre-Peach Spring Tuff Lavas and Peach Spring Tuff Magmatic Enclaves, Black Mountains, Arizona.

Foley, M.L., 2017, Textural and geochemical investigation of the peach spring tuff CA-NV-AZ, USA: evidence for dynamic pre-supereruption processes: Vanderbilt University, 117 p.

Foley, M.L., Miller, C.F., and Gualda, G.A.R. Architecture of a Super-Sized Magma Chamber and Remobilization of its Basal Cumulate (Peach Spring Tuff, USA): Journal of Petrology,.

Frazier, W.O., 2013, Petrochemical Contraints On Generation Of The Peach Spring Tuff Supereruption Magma, Arizona, Nevada, California: Vanderbilt University.

Frost, B.R., Chamberlain, K.R., and Schumacher, J.C., 2000, Sphene (titanite): Phase relations and role as a geochronometer: Chemical Geology, v. 172, p. 131–148, doi: 10.1016/S0009-2541(00)00240-0.

Glazner, A.F., and Coleman, D.S., 2008, The tenuous connection between high-silica rhyolites and granodiorite plutons: , p. 183–186, doi: 10.1130/G24496A.1.

Glazner, A.F., Nielson, J.E., Howard, K.A., and Miller, D.M., 1986, Correlation of the Peach Springs Tuff, a large-volume Miocene ignimbrite sheet in California and Arizona: Geology, v. 14, p. 840–7613.

Green, T.H., and Pearson, N.J., 1986, Rare-Earth Element Partitioning Between Sphene And Coexisting Silicate Liquid At High Pressure And Temperature: Chemical Geology, v. 55, p. 105–119.

Griffin, W.L., 2008, GLITTER: data reduction software for laser ablation ICP-MS: Laser Ablation ICP-MS in the Earth Sciences: Current practices and outstanding issues, p. 308–311.

Gualda, G.A.R., and Ghiorso, M.S., 2013, Low-Pressure Origin of High-Silica Rhyolites and Granites: The Journal of Geology, v. 121, p. 537–545, doi: 10.1086/671395.

Gualda, G.A.R., and Ghiorso, M.S., 2014, Phase-equilibrium geobarometers for silicic rocks based on rhyolite-MELTS. Part 1: Principles, procedures, and evaluation of the method: Contributions to Mineralogy and Petrology, v. 168, p. 1–7999.

Gualda, G.A.R., Ghiorso, M.S., Lemons, R. V., and Carley, T.L., 2012, Rhyolite-MELTS: A modified calibration of MELTS optimized for silica-rich, fluid-bearing magmatic systems: Journal of Petrology, v. 53, p. 875–890, doi: 10.1093/petrology/egr080.

Hayden, L.A., Watson, E.B., and Wark, D.A., 2008, A thermobarometer for sphene (titanite): Contributions to Mineralogy and Petrology, v. 155, p. 529–7999.

Higgins, J.B., and Ribbe, P.H., 1976, The crystal chemistry and space groups of natural and synthetic titanites: Rare Earth Elements in Ultramafic and Mafic Rocks and their Minerals, v. 61, p. 878–888, doi: 10.1201/b11831-7.

Hildreth, W., 2004, Volcanological perspectives on Long Valley, Mammoth Mountain, and Mono Craters: several contiguous but discrete systems: Journal of Volcanology and Geothermal Research, v. 136, p. 169–273.

Jaffe, H.W., 1947, Reexamination of Sphene (Titanite): American Mineralogist: Journal of Earth and Planetary Materials, v. 32, p. 637–642.

Kahl, M., Chakraborty, S., Costa, F., and Pompilio, M., 2011, Dynamic plumbing system beneath volcanoes revealed by kinetic modeling, and the connection to monitoring data: An example from Mt. Etna: Earth and Planetary Science Letters, v. 308, p. 11–22.

Kahl, M., Chakraborty, S., Costa, F., Pompilio, M., Liuzzo, M., and Viccaro, M., 2013, Compositionally zoned crystals and real-time degassing data reveal changes in magma transfer dynamics during the 2006 summit eruptive episodes of Mt. Etna: Bulletin of volcanology, v. 75, p. 1–8900.

Kaiser, J.F., de Silva, S., Schmitt, A.K., Economos, R., and Sunagua, M., 2017, Million-year melt–presence in monotonous intermediate magma for a volcanic–plutonic assemblage in the Central Andes: Contrasting histories of crystal-rich and crystal-poor super-sized silicic magmas: Earth and Planetary Science Letters, v. 457, p. 73–86, doi: 10.1016/j.epsl.2016.09.048.

Kohn, M.J., 2017, Titanite Petrochronology: Reviews in Mineralogy and Geochemistry, v. 83, p. 419–441, doi: 10.2138/rmg.2017.83.13.

Kowallis, B.J., Christiansen, E.H., Dorais, M.J., Winkel, A., Henze, P., Franzen, L., and Webb, H., 2018, Compositional Variation of Fe, Al, and F in titanite (sphene): Geological Society of America Abstracts with Programs, v. 50.

Kowallis, B.J., Christiansen, E.H., and Griffen, D.T., 1997, Compositional variations in titanite: v. 29, 402 p.

Lang, N., Walker, B.J., Claiborne, L.L., Miller, F.C., Hazlett, R., and Heizler, M., 2008, The Spirit Mountain batholith and Secret Pass Canyon volcanic center: A cross-sectional view of the magmatic architecture of the uppermost crust of an extensional terrain, Colorado River, Nevada-Arizona: The Geological Society of America, v. 11, p. 187–214, doi: 10.1130/2008.fl.

Lipman, P.W., 1965, Chemical comparison of glassy and crystalline volcanic rocks: United States Geological Survey Bulletin, v. 1201-D, p. D1–D24.

Loewen, M.W., and Kent, A.J.R., 2012, Sources of elemental fractionation and uncertainty during the analysis of semi-volatile metals in silicate glasses using LA-ICP-MS: Journal of Analytical Atomic Spectrometry, v. 27, p. 1502–1508, doi: 10.1039/c2ja30075c.

McDowell, S.M., Miller, C.F., Mundil, R., Ferguson, C.A., and Wooden, J.L., 2014, Zircon evidence for a~ 200 ky supereruption-related thermal flare-up in the Miocene southern Black Mountains, western Arizona, USA: Contributions to Mineralogy and Petrology, v. 168, p. 1–7999.

McDowell, S.M., Overton, S., Fisher, C.M., Frazier, W.O., Miller, C.F., Miller, J.S., and Economos, R.C., 2016, Hafnium, oxygen, neodymium, strontium, and lead isotopic constraints on magmatic evolution of the supereruptive southern Black Mountains volcanic center, Arizona, USA: A combined LASS zircon-whole-rock study: American Mineralogist, v. 101, p. 311–327, doi: 10.2138/am-2016-5127.

Metcalf, R. V, Smith, E.I., Walker, J.D., Reed, R.C., and Gonzales, D.A., 1995, Isotopic disequilibrium among commingled hybrid magmas: evidence for a two-stage magma mixing-commingling process in the Mt. Perkins Pluton, Arizona: The Journal of Geology, v. 103, p. 509–1376.

Miller, C.F., Colombini, L.L., Wooden, J.L., Mazdab, F.K., Gualda, G.A., Claiborne, L.E., and Ayers, J.C., 2009, Sphene (titanite) as both monitor and driver of evolution of felsic

magma: Miocene volcanic plutonic and rocks of the Colorado River region, NV-AZ, USA:

Miller, C.F., Frazier, W.O., Carley, T.L., Claiborne, L.L., Padilla, A.D.J., Thomas, D., and Gualda, G.A.R., 2014, Zr/Sr Ratios Distinguish Cool & Wet From Hot & Dry Magmatic Suites: Geological Society of America Abstracts with Programs, v. 46, p. 198.

Miller, C.F., and Miller, J.S., 2002, Contrasting stratified plutons exposed in tilt blocks, Eldorado Mountains, Colorado River Rift, NV, USA: Lithos, v. 61, p. 209–4937.

Miller, C.F., and Mittlefehldt, D.W., 1984, Extreme fractionation in felsic magma chambers: a product of liquid-state diffusion or fractional crystallization? Earth and Planetary Science Letters, v. 68, p. 151–158.

Miller, C.F., and Wooden, J.L., 1994, Anatexis, hybridization and the modification of ancient crust: Mesozoic plutonism in the Old Woman Mountains area, California: Lithos, v. 32, p. 111–4937.

Murphy, R.T., and Faulds, J.E., 2003, Interactions between Tertiary magmatism and extension in the Colorado River extensional corridor, Union Pass area, northwestern Arizona:

Mutch, E.J.F., Blundy, J.D., Tattitch, B.C., Cooper, F.J., and Brooker, R.A., 2016, An experimental study of amphibole stability in low-pressure granitic magmas and a revised Al-in-hornblende geobarometer: Contributions to Mineralogy and Petrology, v. 171, p. 1–27, doi: 10.1007/s00410-016-1298-9.

Onuma, N., Higuchi, H., Wakita, H., and Nagasawa, H., 1968, Trace element partition between two pyroxenes and the host lava: Earth and Planetary Science Letters, v. 5, p. 47- 51 %@ 0012- 821X.

Padilla, A. de J., 2011, Volcano-pluton connections in silicic magmatic systems: Insights from southeast Iceland and southern Nevada: , p. 126.

Padilla, A.J., and Gualda, G.A.R., 2016, Crystal-melt elemental partitioning in silicic magmatic systems: An example from the Peach Spring Tuff high-silica rhyolite, Southwest USA: Chemical Geology, v. 440, p. 326–344, doi: 10.1016/j.chemgeo.2016.07.004.

Pamukcu, A.S., Carley, T.L., Gualda, G.A.R., Miller, C.F., and Ferguson, C.A., 2013, The evolution of the peach spring giantmagma body: Evidence from accessory mineraltextures and compositions, bulk pumice and glass geochemistry, and rhyolite-MELTS modeling: Journal of Petrology, v. 54, p. 1109–1148, doi: 10.1093/petrology/egt007.

Pamukcu, A.S., Gualda, G.A.R., Ghiorso, M.S., Miller, C.F., and McCracken, R.G., 2015, Phase-equilibrium geobarometers for silicic rocks based on rhyolite-MELTS—Part 3: Application to the Peach Spring Tuff (Arizona–California–Nevada, USA): Contributions to Mineralogy and Petrology, v. 169, p. 1–7999.

Paterson, B.A., and Stephens, W.E., 1992, Kinetically induced compositional zoning in titanite: implications for accessory-phase/melt partitioning of trace elements: Contributions to Mineralogy and Petrology, v. 109, p. 373–385, doi: 10.1007/BF00283325.

Pearce, J. a, Harris, N.B.W., and Tindle, A.G., 1984, Trace element distribution diagrams for the tectonic interpretation of granitic rocks: Journal of Petrology, v. 25, p. 956–983, doi: 10.1093/petrology/25.4.956.

Pearce, N.J.G., Perkins, W.T., Westgate, J.A., Gorton, M.P., Jackson, S.E., Neal, C.R., and Chenery, S.P., 1997, A {Compilation} of {New} and {Published} {Major} and {Trace} {Element} {Data} for {NIST} {SRM} 610 and {NIST} {SRM} 612 {Glass} {Reference} {Materials}: Geostandards Newsletter, v. 21, p. 115–144, doi: 10.1111/j.1751-908X.1997.tb00538.x.

Pearthree, P.A., Ferguson, C.A., Johnson, B.J., and Guynn, J., 2009, Geologic Map and Report for the Proposed State Route 95 Realignment Corridor in Eastern Mohave Valley , Mohave County , Arizona:

Perry, S.E., Scheland, C.L., Miller, C.F., Claiborne, L.L., McDowell, S.M., and Covey, A.K., 2014, Mineralogical and Geochemical Characterization of Cook Canyon Tuff near Kingman, AZ with implications for Magmatic Processes: Geological Society of America Abstracts with programs, v. 47, p. 543.

Piccoli, P., Candela, P., and Rivers, M., 2000, Interpreting magmatic processes from accessory phases: titanite---a small-scale recorder of large-scale processes: Earth and Environmental Science Transactions of The Royal Society of Edinburgh, v. 91, p. 257–6910.

Ransom, F.L., 1923, Geology of the Oatman Gold District: Washington: Government Printing Office,.

Sahama, T.G., 1946, On the chemistry of the mineral titanite: Bull. Comm. Geol. Finlande, v. 138, p. 120.

Scheland, C.L., Wood, E.M., Miller, C.F., Claiborne, L.L., Foley, M.L., Cribb, W.J., and Carley,

T.L., 2016, Explosive Silicic Volcanism Preceding The Peach Spring Tuff Supereruption, Part 2: Magmatic Processes Recorded By Petrochemistry: Geological Society of America Abstracts with Programs, v. 48.

Schlaerth, H.L., Collins, E., Miller, C.F., Foley, M.L., Claiborne, L.L., and Cribb, W., 2016, Petrologic Investigation Of The Enclave-Bearing Trachydacite To Rhyolite Antelope Lava, Southern Black Mountains, AZ: Geological Society of America Abstracts with Programs, v. 48.

Schwat, E., Wallrich, B.M., Helfrich, A.L., Thompson, I.P., Lang, N.P., and Miller, C.F., 2016, Characterizing And Mapping The Post-Supereruption Sitgreaves Tuff In Meadow Creek Basin, Southern Black Mountains, NW Arizona, *in* Geological Society of America Abstracts with programs,.

Scott, R.B., 1971, Alkali Exchange during Devitrification and Hydration of Glasses in Ignimbrite Cooling Units Author (s): Robert B . Scott Source : The Journal of Geology , Vol . 79 , No . 1 (Jan ., 1971), pp . 100-110 Published by : The University of Chicago Press Sta: The Journal of Geology, v. 79, p. 100–110.

Shannon, R.D., 1976, Revised effective ionic radii and systematic studies of interatomic distances in halides and chalcogenides: Acta crystallographica section A: crystal physics, diffraction, theoretical and general crystallography, v. 32, p. 751–7394.

Sliwinski, J.T., Bachmann, O., Dungan, M.A., Huber, C., Deering, C.D., Lipman, P.W., Martin, L.H.J., and Liebske, C., 2017, Rapid pre-eruptive thermal rejuvenation in a large silicic magma body: the case of the Masonic Park Tuff, Southern Rocky Mountain volcanic field, CO, USA: Contributions to Mineralogy and Petrology, v. 172, p. 1–20, doi: 10.1007/s00410-017-1351-3.

Smith, A.L., 1970, Sphene, perovskite and coexisting Fe-Ti oxide minerals: American Mineralogist, v. 55, p. 264–269.

Smith, V., Williams, S.G., Helfrich, A.L., Miller, C.F., Foley, M.L., and Cribb, W.J., 2016, Geochemical And Petrographic Relations Between Mafic Intrusions In Post-Peach Spring Tuff Deposits In The Southern Black Mountains, Meadow Creek Basin, Near Oatman, Arizona: Geological Society of America Abstracts with programs, v. 48.

Thompson, R.A., Dungan, M.A., and Lipman, P.W., 1986, Multiple Differentiation Processes in

Early-Rift Calc-Alkaline Volcanics, Northern Rio Grande Rift, New Mexico: Journal of Geophysical Research, v. 91, p. 6046–6058.

Thorson, J.P., 1971, Igneous Petrology of the Oatman Quad Mohave County, Arizona: , p. 1–233.

Troch, J., Ellis, B.S., Mark, D.F., Bindeman, I.N., Kent, A.J.R., Guillong, M., and Bachmann, O., 2017, Rhyolite generation prior to a yellowstone supereruption: Insights from the Island Park-Mount Jackson rhyolite series: Journal of Petrology, v. 58, p. 29–52, doi: 10.1093/petrology/egw071.

Tuttle, O.F., and Bowen, N.L., 1958, Origin of granite in the light of experimental studies in the system NaAlSi_3O_8-KAlSi_3O_8-SiO_2-H_2O: Geol. Soc. Am. Mem., v. 74, p. 153.

Valentine, G.A., Buesch, D.C., and Fisher, R. V., 1989, Basal layered deposits of the Peach Springs Tuff, northwestern Arizona, USA: Bulletin of Volcanology, v. 51, p. 395–414, doi: 10.1007/BF01078808.

Walker, B.A., Miller, C.F., Lowery Claiborne, L., Wooden, J.L., and Miller, J.S., 2007, Geology and geochronology of the Spirit Mountain batholith, southern Nevada: Implications for timescales and physical processes of batholith construction: Journal of Volcanology and Geothermal Research, v. 167, p. 239–262, doi: 10.1016/j.jvolgeores.2006.12.008.

Wallrich, B.M., Miller, F.C., Claiborne, L.L., McIntosh, W.C., Bradshaw, R., and Gualda, G.A.R., 2018, Sitgreaves Tuff, Southern Black Mountains, Nw Az: Phase Chemistry And Ar Dating Illuminate The Evolution Of A Dynamic Silicic Magmatic System, *in* Geological Society of America Abstracts with Programs.

Wallrich, B.M., Schwat, E., Thompson, I.P., Miller, C.F., Claiborne, L.L., Foley, M.L., and Cribb, W., 2016, Sitgreaves Tuff: Insights into the Evolution of a Post Supereruption High Silica Rhyolite, Southern Black Mountains, NW AZ, *in* Geological Society of America, p. 16057.

Watson, E.B., and Harrison, T.M., 1983, Zircon saturation revisited: temperature and composition effects in a variety of crustal magma types: Earth and Planetary Science Letters, v. 64, p. 295–304.

Wilke, M., and Behrens, H., 1999, The dependence of the partitioning of iron and europium between plagioclase and hydrous tonalitic melt on oxygen fugacity: Contributions to

Mineralogy and Petrology, v. 137, p. 102–114, doi: 10.1007/s004100050585.

Wolff, J.A., 2017, On the syenite-trachyte problem: v. 45, p. 1–4, doi: 10.1130/G39415.1.

Xirouchakis, D., Lindsley, D.H., and Frost, B.R., 2001, Assemblages with titanite (CaTiOSiO4), Ca-Mg-Fe olivine and pyroxenes, Fe-Mg-Ti oxides, and quartz: Part II. Application: American Mineralogist, v. 86, p. 254–264, doi: 10.2138/am-2001-2-307.

Young, R.A., and Brennan, W.J., 1974, Peach Springs tuff: Its Bearing on structural evolution of the Colorado plateau and development of Cenozoic drainage in Mohave County, Arizona: Bulletin of the Geological Society of America, v. 85, p. 83–90, doi: 10.1130/0016-7606(1974)85<83:PSTIBO>2.0.CO;2.

Zielinski, R.A., Lipman, P.W., and Millard, H.T., 1977, Minor-element abundances in obsidian, perlite, and felsite of calc-alkalic rhyolites: American Mineralogist, v. 62, p. 426–437, http://www.intl-ammin.geoscienceworld.org/content/62/5-6/426.short.

APPENDIX A

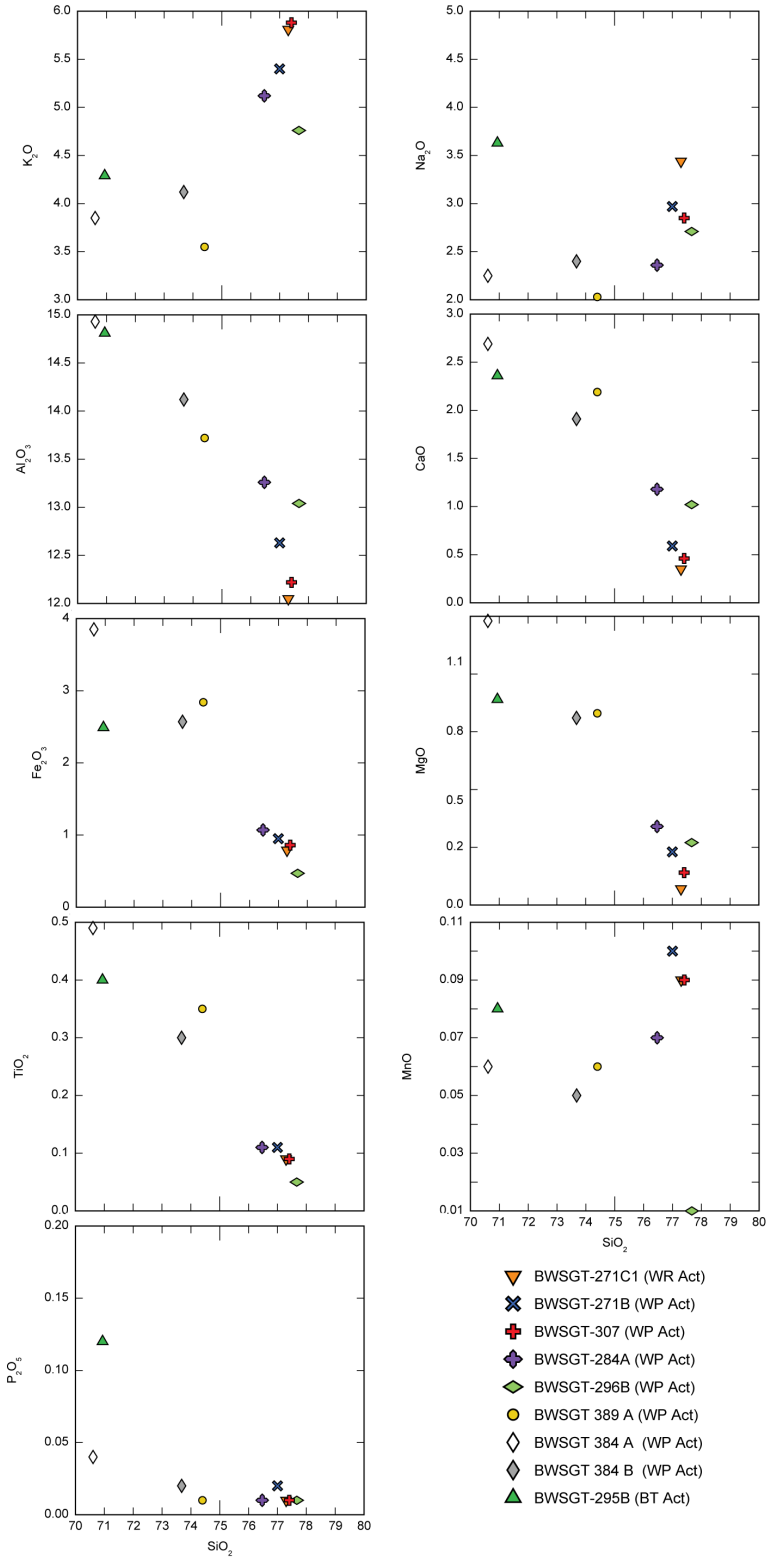
K2O
Na2O
Al2O3
CaO
Fe2O3
MgO
TiO2
MnO
P2O5
SiO2
SiO2
BWSGT-271C1 (WR Act)
BWSGT-271B (WP Act)
BWSGT-307 (WP Act)
BWSGT-284A (WP Act)
BWSGT-296B (WP Act)
BWSGT 389 A (WP Act)
BWSGT 384 A (WP Act)
BWSGT 384 B (WP Act)
BWSGT-295B (BT Act)

Table 11: Act Labs whole pumice (WP) and whole rock (WR) data for the Sitgreaves Tuff. Major element oxides normalized to 100% anhydrous.

Sample	Unit Symbol	Detection Limit	Analysis Method
Unit			
SiO_2	%	0.01	FUS-ICP
TiO_2	%	0.001	FUS-ICP
Al_2O_3	%	0.01	FUS-ICP
Fe_2O_3	%	0.01	FUS-ICP
MnO	%	0.001	FUS-ICP
MgO	%	0.01	FUS-ICP
CaO	%	0.01	FUS-ICP
Na_2O	%	0.01	FUS-ICP
K2O	%	0.01	FUS-ICP
P_2O_5	%	0.01	FUS-ICP
Au	ppb	1	INAA
Ag	ppm	0.5	MULT INAA / TD-ICP
As	ppm	1	INAA
Ba	ppm	1	FUS-ICP
Be	ppm	1	FUS-ICP
Bi	ppm	0.1	FUS-MS
Br	ppm	0.5	INAA
Cd	ppm	0.5	TD-ICP
Co	ppm	0.1	INAA
Cr	ppm	0.5	INAA
Cs	ppm	0.1	FUS-MS
Cu	ppm	1	TD-ICP
Ga	ppm	1	FUS-MS
Ge	ppm	0.5	FUS-MS
Hf	ppm	0.1	FUS-MS
Hg	ppm	1	INAA
In	ppm	0.1	FUS-MS
Ir	ppb	1	INAA
Mo	ppm	2	FUS-MS
Nb	ppm	0.2	FUS-MS
Ni	ppm	1	TD-ICP
Pb	ppm	5	TD-ICP

Rb	ppm	1	FUS-MS
S	%	0.001	TD-ICP
Sb	ppm	0.1	INAA
Sc	ppm	0.01	INAA
Se	ppm	0.5	INAA
Sn	ppm	1	FUS-MS
Sr	ppm	2	FUS-ICP
Ta	ppm	0.01	FUS-MS
Th	ppm	0.05	FUS-MS
U	ppm	0.01	FUS-MS
V	ppm	5	FUS-ICP
W	ppm	1	INAA
Y	ppm	1	FUS-ICP
Zn	ppm	1	MULT INAA / TD-ICP
Zr	ppm	1	FUS-ICP
La	ppm	0.05	FUS-MS
Ce	ppm	0.05	INAA
Pr	ppm	0.05	FUS-MS
Nd	ppm	1	INAA
Sm	ppm	0.01	FUS-MS
Eu	ppm	0.05	FUS-MS
Gd	ppm	1	INAA
Tb	ppm	0.01	FUS-MS
Dy	ppm	0.01	INAA
Ho	ppm	0.005	FUS-MS
Er	ppm	0.2	INAA
Tl	ppm	0.01	FUS-MS
Tm	ppm	0.01	FUS-MS
Yb	ppm	0.1	INAA
Lu	ppm	0.01	FUS-MS
Mass	g		INAA

Table 13 Continued,

Sample	BWSGT-271B (WP)	BWSGT-271-C1 (WR)	BWSGT-284A (WP)
Unit	**SGT-2**	**SGT-2**	**SGT-2**
SiO2	77	77.3	76.47
TiO2	0.11	0.09	0.11
Al2O3	12.63	12.05	13.26
Fe2O3	0.95	0.79	1.07
MnO	0.1	0.09	0.07
MgO	0.23	0.07	0.34
CaO	0.59	0.35	1.18
Na2O	2.97	3.44	2.36
K2O	5.4	5.81	5.12
P2O5	0.02	0.01	0.01
Au	4	< 1	7
Ag	<0.5	< 0.5	0.6
As	5	6	3
Ba	95	4	7
Be	7	7	5
Bi	0.2	0.2	0.1
Br	5.8	1.7	1.1
Cd	< 0.5	< 0.5	< 0.5
Co	1.5	< 0.1	< 0.1
Cr	< 0.5	< 0.5	< 0.5
Cs	2.8	3.2	5.3
Cu	8	2	4
Ga	20	21	20
Ge	1.7	1.6	1.1
Hf	8.3	8.2	6.4
Hg	< 1	< 1	< 1
In	< 0.1	< 0.1	< 0.1
Ir	< 1	< 1	< 1
Mo	4	5	3
Nb	38.2	35.6	35.5
Ni	< 1	< 1	< 1
Pb	36	36	27
Rb	221	228	255

S	0.005	0.007	0.006
Sb	0.6	0.7	0.5
Sc	1.55	1.35	1.7
Se	< 0.5	1.5	1.5
Sn	3	3	3
Sr	42	4	25
Ta	2.94	2.89	3.01
Th	30.3	30.8	28
U	4.87	5.53	5.41
V	< 5	< 5	< 5
W	< 1	< 1	< 1
Y	29	25	21
Zn	65	64	77
Zr	263	257	162
La	35.4	34.1	22
Ce	65.6	60.5	46.1
Pr	5.98	5.18	3.77
Nd	15.4	12.8	9.72
Sm	2.87	2.18	2.04
Eu	0.116	0.055	0.041
Gd	2.74	2.04	1.78
Tb	0.55	0.43	0.41
Dy	3.74	3.14	2.82
Ho	0.86	0.75	0.62
Er	2.78	2.47	1.94
Tl	0.75	0.81	0.59
Tm	0.479	0.43	0.32
Yb	3.34	3.25	2.44
Lu	0.534	0.483	0.362
Mass	1.094	1.207	1.126

Table 13 continued.

Sample	BWSGT-296B (WP)	BWSGT-307 (WP)	BWSGT 384A (WP)
Unit	SGT-2	SGT-2	SGT-1
SiO_2	77.67	77.41	70.61
TiO_2	0.05	0.09	0.49
Al_2O_3	13.04	12.22	14.93
Fe_2O_3	0.47	0.86	3.85
MnO	0.01	0.09	0.06
MgO	0.27	0.14	1.23
CaO	1.02	0.46	2.69
Na_2O	2.71	2.85	2.25
K2O	4.76	5.88	3.85
P_2O_5	0.01	0.01	0.04
Au	3	7	28
Ag	< 0.5	0.5	< 0.5
As	< 1	6	1
Ba	225	3	1453
Be	7	7	3
Bi	< 0.1	0.2	< 0.1
Br	< 0.5	3	< 0.5
Cd	< 0.5	< 0.5	< 0.5
Co	< 0.1	1.5	5.1
Cr	2.8	< 0.5	1.5
Cs	1	3.5	5.9
Cu	1	11	10
Ga	15	21	18
Ge	< 0.5	1.4	0.9
Hf	4.9	7	7.7
Hg	< 1	< 1	< 1
In	< 0.1	< 0.1	< 0.1
Ir	< 1	< 1	< 1
Mo	< 2	5	< 2
Nb	13.6	42.3	10.3
Ni	< 1	< 1	3
Pb	< 5	40	17
Rb	116	286	137
S	0.008	0.004	0.005

Sb	0.1	0.8	0.4
Sc	0.8	1.45	4.18
Se	< 0.5	< 0.5	< 0.5
Sn	1	6	1
Sr	137	10	1267
Ta	2.38	3.1	0.93
Th	9.32	30.4	19.9
U	2.42	5.33	2.02
V	< 5	< 5	36
W	< 1	< 1	< 1
Y	4	29	11
Zn	27	69	58
Zr	121	182	336
La	5.37	33.5	77.2
Ce	10.9	63.3	159
Pr	1.09	5.41	13.9
Nd	3	14.2	45.8
Sm	0.58	2.58	6.43
Eu	0.021	0.055	1.84
Gd	0.6	2.53	3.8
Tb	0.11	0.56	0.45
Dy	0.69	3.9	2.2
Ho	0.13	0.85	0.39
Er	0.39	2.8	1.17
Tl	0.05	0.88	0.4
Tm	0.058	0.475	0.168
Yb	0.37	3.41	1.03
Lu	0.05	0.514	0.157
Mass	1.106	1.081	1.043

Table 13 Continued.

Sample	**BWSGT 384B (WP)**	**BWSGT 389A (WP)**	**BWSGT-295B (BT)**
Unit	**SGT-1**	**SGT-1**	**SGT-1**
SiO_2	73.68	74.4	70.94
TiO_2	0.3	0.35	0.4
Al_2O_3	14.12	13.72	14.81

Fe_2O_3	2.57	2.84	2.49
MnO	0.05	0.06	0.08
MgO	0.81	0.83	0.89
CaO	1.91	2.19	2.36
Na_2O	2.4	2.03	3.63
K2O	4.12	3.55	4.29
P_2O_5	0.02	0.01	0.12
Au	80	58	< 1
Ag	< 0.5	< 0.5	< 0.5
As	< 1	< 1	2
Ba	1440	936	842
Be	3	3	3
Bi	< 0.1	< 0.1	0.1
Br	< 0.5	< 0.5	< 0.5
Cd	< 0.5	< 0.5	< 0.5
Co	4.1	4.2	5.4
Cr	17.3	9.2	9.6
Cs	2.2	4.3	2.5
Cu	9	13	12
Ga	18	15	18
Ge	1.2	0.8	0.9
Hf	6.4	5.3	6.5
Hg	< 1	< 1	< 1
In	< 0.1	< 0.1	< 0.1
Ir	< 1	< 1	< 1
Mo	< 2	< 2	< 2
Nb	12.1	9.2	22.1
Ni	2	3	7
Pb	18	19	21
Rb	134	95	138
S	0.006	0.004	0.02
Sb	0.4	0.3	0.4
Sc	4.07	3.54	3.8
Se	< 0.5	< 0.5	< 0.5
Sn	2	< 1	2
Sr	702	935	398
Ta	1.07	0.77	1.7
Th	21.1	10.2	20.2

U	2.27	1.54	3.06
V	21	29	30
W	< 1	< 1	< 1
Y	13	5	27
Zn	52	43	49
Zr	281	249	239
La	108	22.1	63.7
Ce	184	40.9	101
Pr	20.1	4.31	12.1
Nd	68.2	15.8	39
Sm	9.03	2.5	6.58
Eu	1.78	0.903	0.949
Gd	4.98	1.58	4.83
Tb	0.61	0.18	0.75
Dy	3.01	1.1	4.5
Ho	0.51	0.2	0.92
Er	1.49	0.57	2.76
Tl	0.86	0.49	0.38
Tm	0.202	0.079	0.422
Yb	1.38	0.53	2.73
Lu	0.203	0.087	0.43
Mass	1.096	1.091	1.064

APPENDIX B

Images of SGT2 Sanidine

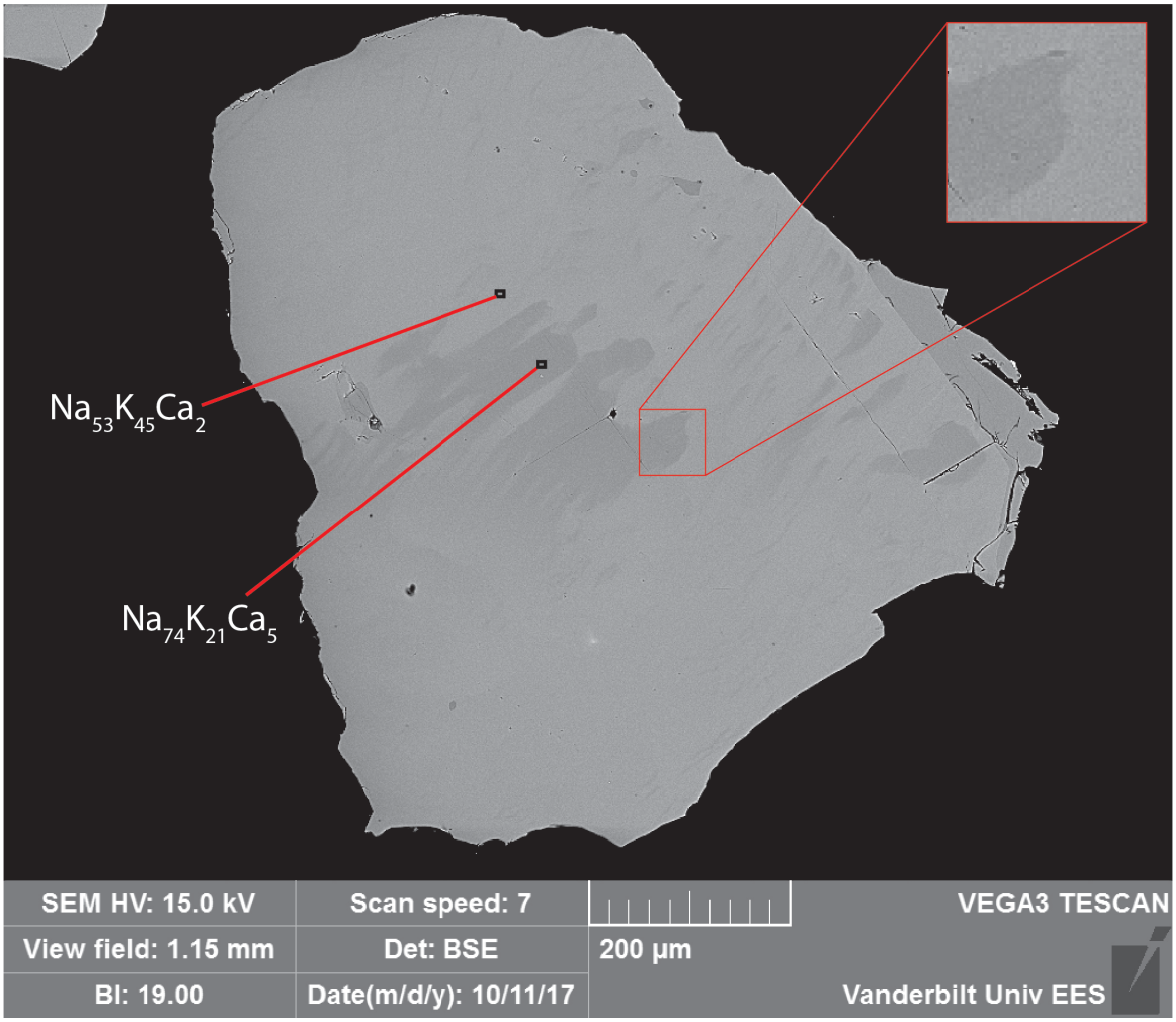

(Above) BSE image of most common texture observed in SGT2 sanidine-anorthoclase.

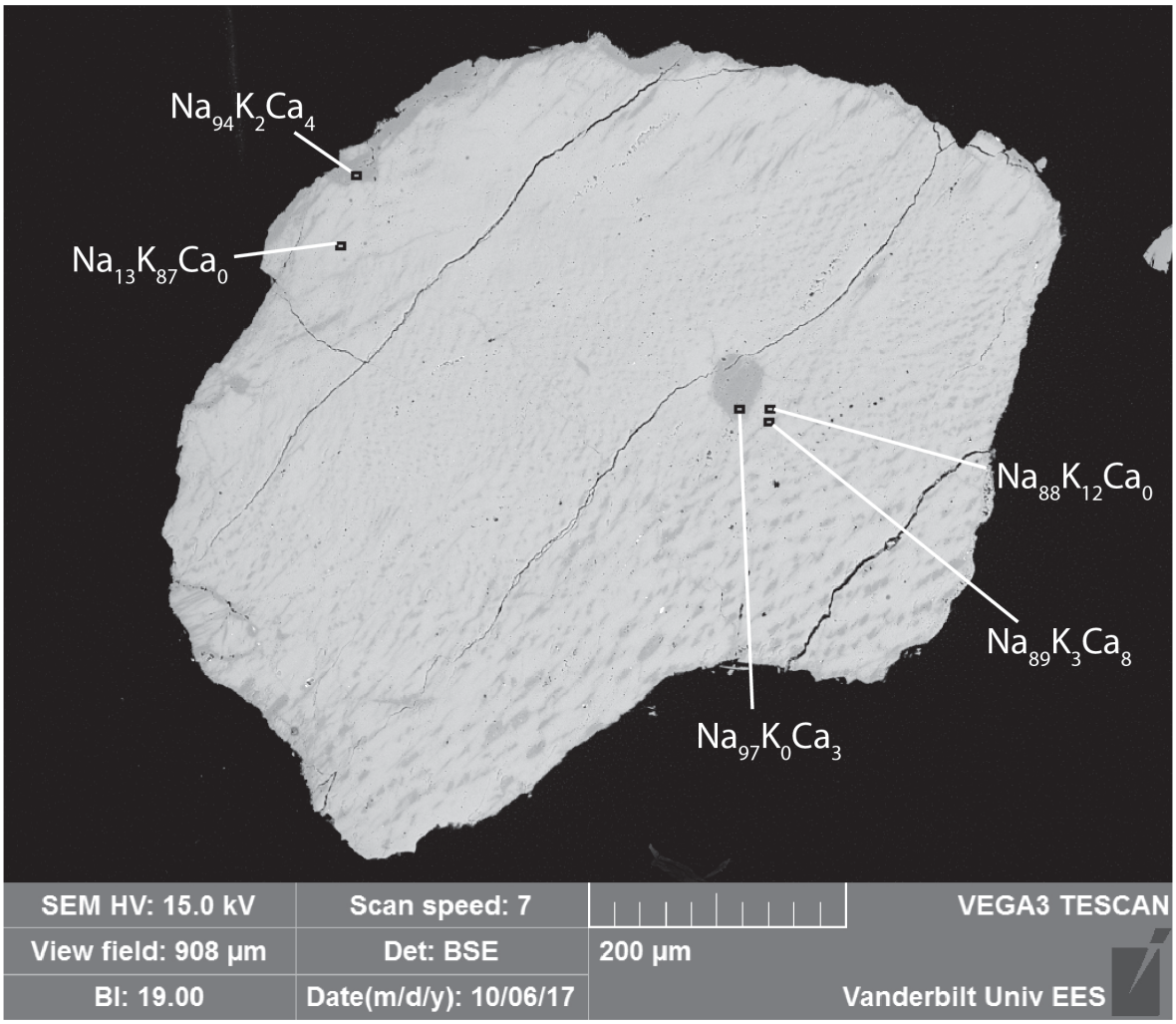

(Above) BSE image of rare perthite grains within SGT2 pumice.

APPENDIX C

Table 12: Pumice glass analyses for SGT2 sample BWSGT-381(obtained via SEM-EDS)

Spectrum Label	Na	Mg	Al	Si	K	Ca	Ti	Mn	Fe	Total	A/CNK
Spectrum 711	2.97	0	12.24	77.69	6.13	0.34	0.05	0.03	0.54	100	1.01
Spectrum 712	2.5	0.04	12.48	77.32	6.48	0.3	0	0.18	0.71	100	1.07
Spectrum 713	2.52	0.04	12.36	77.15	6.62	0.42	0.16	0.1	0.63	100	1.02
Spectrum 714	2.3	0.08	12.47	77.42	6.39	0.35	0.08	0.17	0.74	100	1.10
Spectrum 715	2.72	0.03	12.51	77.42	6.36	0.35	0	0.08	0.51	100	1.04
Spectrum 716	2.51	0	12.4	77.39	6.35	0.43	0.03	0.18	0.7	100	1.05
Spectrum 699	2.92	0.04	12.38	77.39	6.16	0.33	0.1	0.06	0.61	100	1.02
Spectrum 700	3.18	0.02	12.46	77.13	5.94	0.34	0.11	0.06	0.76	100	1.01
Spectrum 701	3	0	12.46	77.66	5.99	0.3	0.05	0	0.54	100	1.04
Spectrum 702	2.86	0.07	12.36	77.57	6.06	0.32	0.08	0	0.68	100	1.04
Spectrum 703	3.07	0.05	12.46	77.45	5.89	0.33	0.04	0.06	0.64	100	1.03
Spectrum 704	2.89	0	12.37	77.42	6.14	0.34	0.05	0	0.79	100	1.03
Spectrum 705	2.69	0.04	12.42	77.3	6.18	0.4	0.05	0.06	0.86	100	1.05
Spectrum 706	2.97	0	12.63	77.44	5.89	0.38	0.01	0	0.69	100	1.06
Spectrum 707	2.97	0.09	12.46	77.38	6.09	0.38	0.02	0.02	0.6	100	1.02
Spectrum 708	3	0	12.44	77.27	6.1	0.35	0.06	0	0.78	100	1.02
Spectrum 681	3.11	0.04	13.02	76.44	5.97	0.48	0.14	0.08	0.72	100	1.04
Spectrum 682	2.76	0.08	12.47	77.34	6.08	0.45	0.04	0.08	0.7	100	1.04
Spectrum 684	2.66	0.03	12.38	77.27	6.27	0.46	0.03	0.08	0.81	100	1.03
Spectrum 685	2.75	0	12.68	77.08	6.38	0.31	0.05	0.11	0.64	100	1.06
Spectrum 686	3.33	0.04	12.5	77.52	5.52	0.42	0.13	0	0.54	100	1.02
Spectrum 687	2.98	0.07	12.16	78.16	5.52	0.38	0.12	0.06	0.55	100	1.05
Spectrum 688	2.47	0.04	12.55	77.28	6.33	0.41	0.13	0	0.8	100	1.07
Spectrum 691	2.47	0.04	12.43	77.38	6.26	0.33	0.12	0.04	0.93	100	1.08
Spectrum 692	3	0	12.46	77.37	5.91	0.31	0.1	0.2	0.64	100	1.05
Spectrum 693	2.45	0.07	12.42	77.6	6.33	0.3	0	0.15	0.68	100	1.09
Spectrum 672	2.77	0.01	12.22	77.4	6.34	0.4	0.16	0.04	0.65	100	1.00
Spectrum 673	2.66	0.01	12.53	77.18	6.28	0.38	0.05	0	0.9	100	1.05
Spectrum 674	2.87	0.03	12.29	77.56	6.18	0.37	0.05	0	0.64	100	1.02
Spectrum 675	2.77	0.01	12.28	77.59	6.35	0.32	0.04	0.02	0.63	100	1.02
Spectrum 676	2.65	0.05	12.03	77.83	6.21	0.32	0.16	0.06	0.69	100	1.03
Spectrum 677	2.95	0	12.57	76.85	6.51	0.28	0.02	0.21	0.62	100	1.01
Spectrum 678	2.43	0.05	12.44	77.42	6.74	0.28	0	0.09	0.56	100	1.05
Spectrum 679	2.97	0.1	12.55	77.37	6.09	0.34	0.08	0.08	0.41	100	1.04

Spectrum 680	2.65	0	12.4	77.27	6.42	0.41	0.08	0.12	0.66	100	1.03
Spectrum 662	2.73	0.03	12.37	77.27	6.38	0.32	0.1	0.01	0.78	100	1.03
Spectrum 663	2.78	0.01	12.56	77.25	6.13	0.38	0.03	0.24	0.61	100	1.05
Spectrum 664	2.49	0.06	12.52	77.42	6.51	0.32	0.08	0.03	0.56	100	1.07
Spectrum 665	2.85	0.02	12.38	77.16	6.16	0.33	0.13	0.21	0.76	100	1.03
Spectrum 666	2.6	0.01	12.5	77.22	6.52	0.29	0	0.08	0.79	100	1.05
Spectrum 667	2.67	0.06	12.29	77.59	6.25	0.27	0.05	0	0.83	100	1.05
Spectrum 668	2.61	0.07	12.44	77.33	6.37	0.39	0.07	0.1	0.6	100	1.04
Spectrum 669	2.81	0	12.44	77.43	6.13	0.38	0	0.15	0.66	100	1.04
Spectrum 670	2.69	0.04	12.52	76.93	6.31	0.32	0.24	0.09	0.87	100	1.06
Spectrum 671	2.58	0.03	12.31	77.44	6.47	0.37	0.07	0.02	0.71	100	1.03
Average	**2.80**	**0.03**	**12.43**	**77.36**	**6.18**	**0.36**	**0.08**	**0.07**	**0.69**		**1.04**
SD	**0.22**	**0.03**	**0.16**	**0.28**	**0.24**	**0.05**	**0.05**	**0.07**	**0.11**		**0.02**
RD	**0.08**	**0.87**	**0.01**	**0.00**	**0.04**	**0.14**	**0.61**	**1.02**	**0.16**		**0.02**

Table 13: Titanite hosted melt inclusion data for SGT2 sample BWSGT-381 (obtained via SEM-EDS)

Spectrum Label	Na	Mg	Al	Si	K	Ca	Ti	Mn	Fe	Total	A/CNK
Spectrum 858	4.04	0	12.22	77.73	4.63	0.36	0.19	0	0.83	100	0.991
Spectrum 859	4.06	0	12.43	77.73	4.56	0.34	0.14	0.1	0.64	100	1.015
Spectrum 860	3.79	0.05	12.51	77.81	4.5	0.32	0.18	0.16	0.67	100	1.069
Spectrum 861	3.84	0.03	12.55	77.11	4.53	0.6	0.21	0.34	0.79	100	1.018
Spectrum 862	3.79	0.01	12.29	77.98	4.49	0.4	0.2	0	0.85	100	1.038
Spectrum 863	3.77	0	12.37	77.72	4.41	0.46	0.15	0.2	0.92	100	1.046
Spectrum 864	3.94	0.09	12.28	77.63	4.54	0.35	0.12	0.09	0.95	100	1.019
Spectrum 865	3.92	0.05	12.43	77.59	4.61	0.52	0.07	0.1	0.71	100	1.003
Spectrum 866	3.99	0	12.13	77.49	4.47	0.46	0.38	0.26	0.83	100	0.990
Spectrum 867	3.97	0	12.52	77.59	4.56	0.42	0.11	0	0.84	100	1.023
Spectrum 868	3.97	0.02	12.22	77.62	4.39	0.51	0.46	0	0.81	100	1.000
Spectrum 869	4.07	0	12.66	76.95	4.41	0.63	0.43	0.01	0.84	100	1.002
Spectrum 872	3.88	0.06	12.44	77.7	4.55	0.45	0.17	0	0.75	100	1.025
Spectrum 873	3.91	0.02	12.4	77.31	4.53	0.45	0.17	0.22	1	100	1.019
Spectrum 874	4	0.04	12.41	77.69	4.55	0.37	0.12	0.17	0.66	100	1.018
Spectrum 887	4.32	0.04	12.4	77.23	4.37	0.46	0.22	0.17	0.79	100	0.977
Spectrum 888	3.96	0.09	12.54	77.45	4.42	0.46	0.14	0.22	0.71	100	1.032

Spectrum 889	4.03	0.09	12.4	77.58	4.42	0.5	0.19	0.12	0.67	100	1.005
Spectrum 890	4.32	0.07	12.37	77.39	4.5	0.51	0.21	0.03	0.6	100	0.958
Spectrum 891	4.05	0.04	12.37	77.52	4.41	0.38	0.31	0.15	0.78	100	1.019
Spectrum 892	4.24	0.09	12.45	77.24	4.4	0.4	0.25	0.08	0.85	100	0.998
Spectrum 893	3.96	0.05	12.59	77.35	4.37	0.56	0.25	0.13	0.75	100	1.026
Spectrum 896	3.99	0.01	12.58	77.4	4.34	0.59	0.29	0.18	0.63	100	1.019
Spectrum 897	4.04	0.02	12.27	77.37	4.39	0.39	0.35	0.08	1.1	100	1.012
Average	**3.99**	**0.04**	**12.41**	**77.51**	**4.47**	**0.45**	**0.22**	**0.12**	**0.79**		**1.01**
SD	**0.14**	**0.03**	**0.13**	**0.24**	**0.08**	**0.09**	**0.10**	**0.09**	**0.12**		**0.02**
RD	**0.04**	**0.89**	**0.01**	**0.00**	**0.02**	**0.19**	**0.46**	**0.80**	**0.15**		**0.02**

APPENDIX D

Sitgreaves Tuff fieldwork photographs

SGT Looking west from Sitgreaves pass

Large basin filling deposit of SGT looking west toward the Gold Road Mine. On this side of the pass the SGT is in contact with Gold Road Latite (GRL) and Flag Spring Trachyte. There are great exposures of the SGT filling ”cracks” within the paleo-surface of the GRL.

SGT (west of Sitgreaves pass)

At this location on the north side of the exposure to the west of SGT pass there are large megablocks of a aphyric (black almost glassy groundmass) lava. The lava contains ~4-6% biotite and plagioclase as the main phenocryst phase (could correlate with the flag spring trachyte?). The tuff here has also been silicified from hydrothermal activity along the GLR-SGT contact.

Sitgreaves Tuff Section looking North (East of Sitgreaves pass)

In this picture SGT1 appears to form a wedge shaped outcrop against the Gold Road Latite (standing on this unit). The contact relations are misleading directly below where the picture was taken (See next picture for description). The lines indicate breaks and apparent bedding planes in the SGT section. The crosscutting dike was the last unit within the sequence of events (indicated by chilled margins on the tuff, it cuts through the GRL, SGT, and MCT.

Sitgreaves Tuff Section looking North

In this picture SGT1 appears to form a wedge shaped outcrop against the Gold Road Latite (standing on this unit). The contact relations are misleading directly below where the picture was taken (See next picture for description). The lines indicate breaks and apparent bedding planes in the SGT section. The crosscutting dike was the last unit within the sequence of events (indicated by chilled margins on the tuff, it cuts through the GRL, SGT, and MCT.

Contact relations between units

This picture shows the bedding planes within the SGT unit 1 truncating into the GRL. Also not the lithic clasts of GRL, and their high concentration near the contact, suggesting that the GRL was a paleosurface from which the lithics were incorporated into the tuff.

SGT Deposits

SGT ignimbrite veneer deposits blanketing paleo ridges. Elephants Tooth is directly behind this deposit and boundary cone is in the upper right. Both are volcanic necks and attest to the presence of numerous vents within this area of the southern Black Mountains.

Contact Relations cont.

This picture shows a larger view of the last image. At first glance it might seem that the contact between the SGT and the GRL was an ~45 degree onlap surface. However, the observations from the last image contradict this interpretation.

Contact relations between units

Airfall units, graded beds.

This picture shows the bedding planes within the SGT unit 1 lapping onto GRL (outcrop just to the left in the picture). This outcrop calls into question the bedding planes that truncate into the GRL. Possibly some onlap and some truncation of the tuffaceous flows and falls?

Contact relations between units

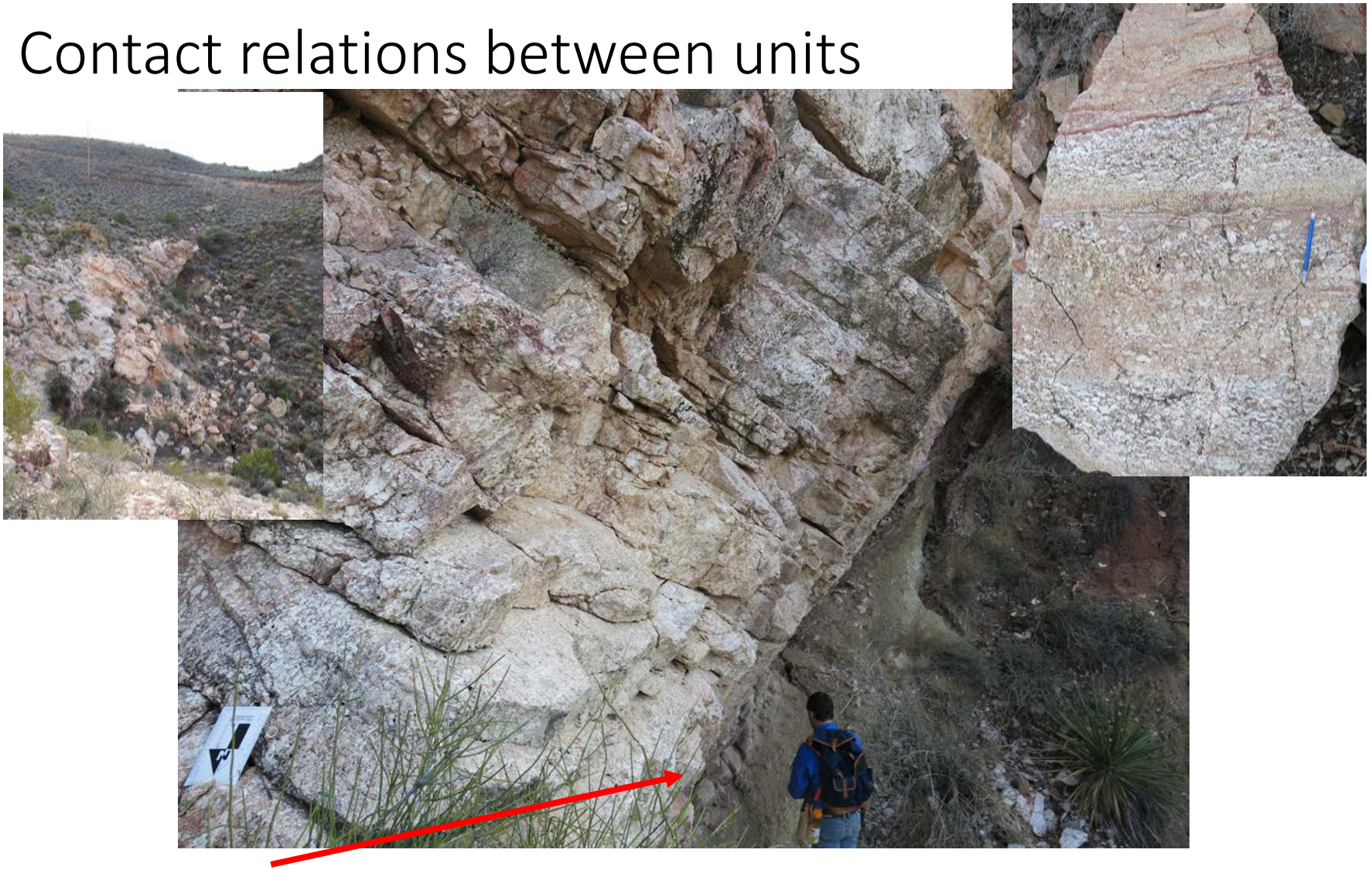

Red arrow points to a sharp contact between GLR and Silicified SGT. At this location the GRL has been extensively altered (argillic) and is composed of clays. If you walk ~ 20 meters to the west there is unaltered GRL. Small picture in the upper right shows the beautiful layering of the silicified fall deposits at this location.

Contact relations between units

SGT-GRL contact. Red arrow points to crack filling SGT into GRL, supporting the hypothesis that SGT was deposited onto paleo-surfaces. Also worth noting here is the dip of the SGT, GRL contact, suggests that the dip of the SGT is primary (onlap, basin filling)

Contact relations between units

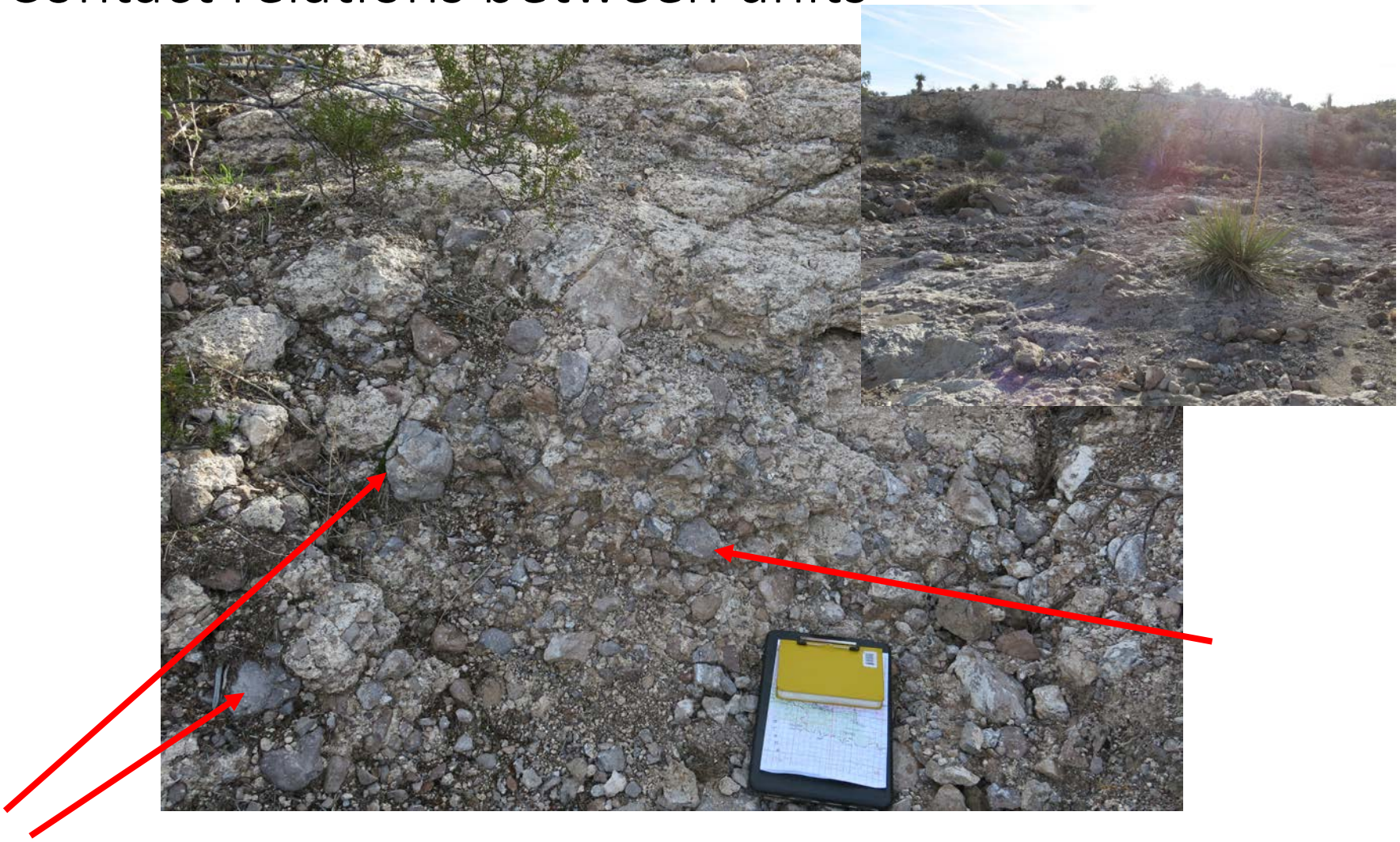

SGT with Meadow Creek Trachyte lithic fragments at a paleo channel deposit.

SGT1 – Antelope Lava Contact

In this picture the lowest units of SGT are visible. The deposit in contact with the 18.5 Ma Antelope lava is an airfall deposit. This appears to be a sequence of fall deposits based on the number of graded (coarse to fining upwards) beds present. Above the airfall sequence there is a ~0.5 m thick pyroclastic flow sheet capped by additional interbedded airfall and flow sheets.

SGT1 – Antelope Lava Contact

The mini sledge in the lower right of the picture is sitting on Antelope lava. The graded units are SGT1 airfall.

SGT1 (BWSGT-390)

Pumice rich fall deposit within SGT1. Note the more silicic (color index is higher (felsic/mafic) that other units within SGT1, yet, there is still very obvious mafic phaee of amphibole and biotite

SGT1 (Lower airfall sequence)

Above sample 390 location, 390 location approx. correlates with the lowest unit in this picture.

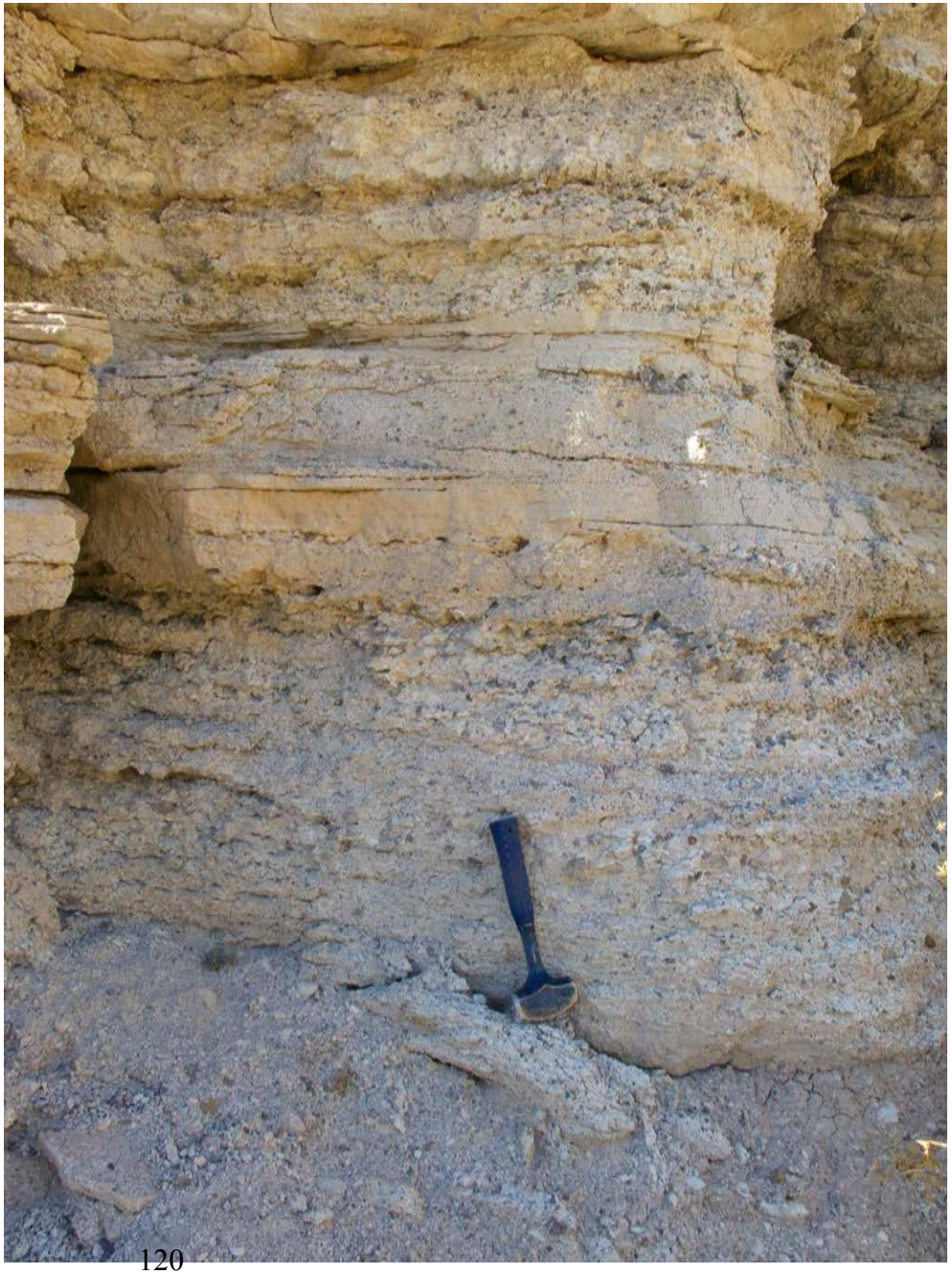

SGT1 (Lower airfall sequence)

Within the SGT1 (BWSGT-390 sample location) sample horizon there are rare large pumice clasts.

BWSGT-295B

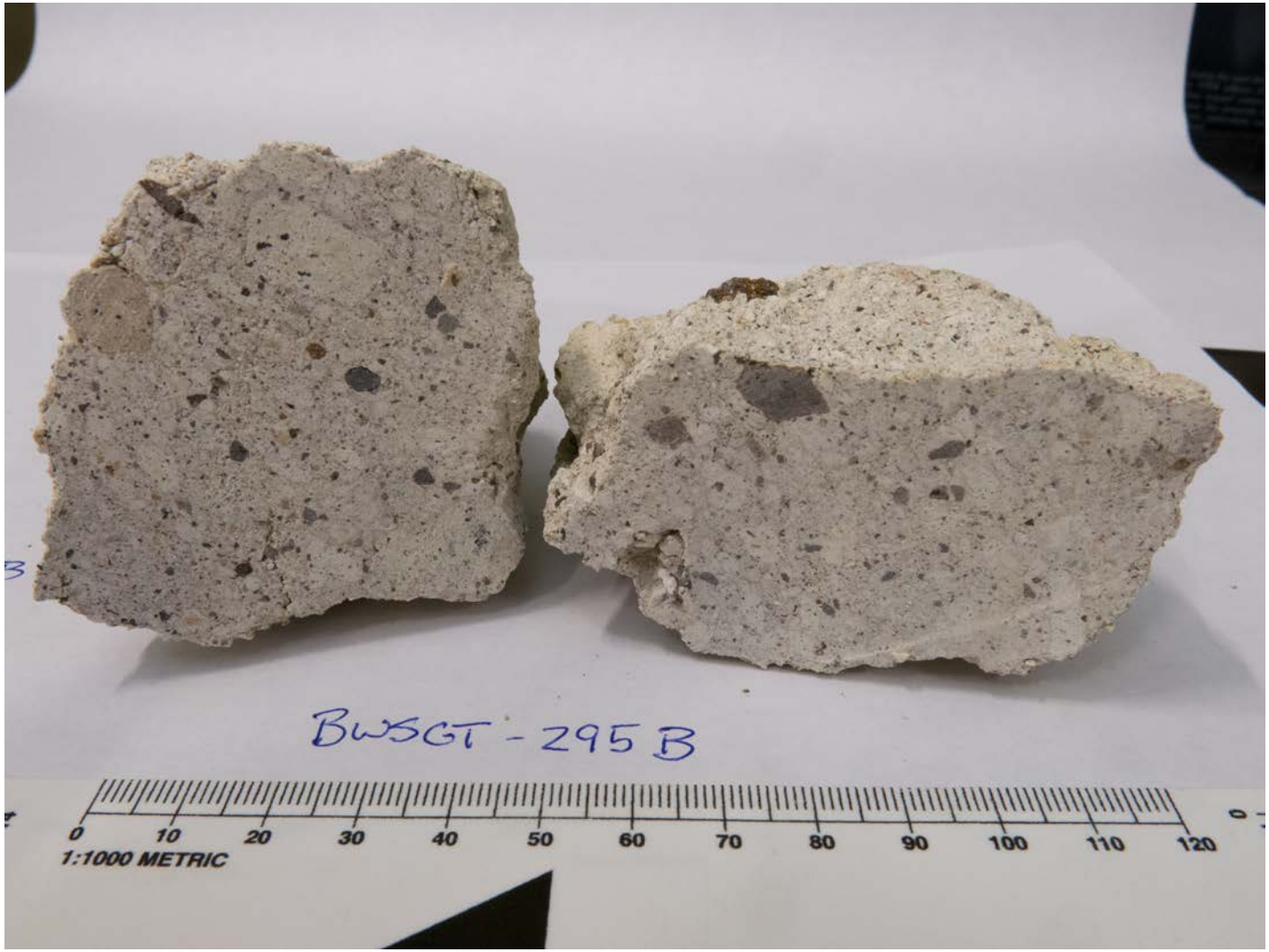

Hand sample of the pyroclastic flow unit above the lowest airfall sequence within SGT1

SGT1 and SGT2 Contact Relations

At the top of SGT1 there is an ash flow unit that contains a matrix composed of concentrated angular crystal fragments, ash, and aligned pumice. This unit is the only one of this type within SGT1 unit (interesting that there is only one of this type within SGT2, at the base of the upper airfall sequence).

SGT1 and SGT2 Contact Relations

Contact between SGT1 ashflow unit and the base of SGT2 cliff forming unit appears to be sharp with no paleosol surface.

SGT1 Ashflow unit (BWSGT-296A)

This is a zoomed in picture of the ash flow unit at the top of SGT1. Pumices appear to show a clear alignment (left-right). Matrix appears to be much more “sandy” than the rest of the tuff within this unit. Upon further investigation using a thin section it seems clear that this is an ashflow based on the angular shapes of the crystal fragments within the unit and the aligned pumices. Pumice within this unit contain ~10-15 % phenocrysts, notably abundant amphibole.

SGT1 Ashflow unit (BWSGT-296A)

This is a zoomed in picture of the ash flow unit at the top of SGT1. Pumices appear to show a clear alignment (left-right). Matrix appears to be much more “sandy” than the rest of the tuff within this unit. Upon further investigation using a thin section it seems clear that this is an ashflow based on the angular shapes of the crystal fragments within the unit and the aligned pumices. Pumice within this unit contain ~10-15 % phenocrysts, notably abundant amphibole.

SGT1 Ashflow unit (BWSGT-296A)

This is a zoomed in picture of the ash flow unit at the top of SGT1. Pumices appear to show a clear alignment (left-right). Matrix appears to be much more “sandy” than the rest of the tuff within this unit. Upon further investigation using a thin section it seems clear that this is an ashflow based on the angular shapes of the crystal fragments within the unit and the aligned pumices. Pumice within this unit contain ~10-15 % phenocrysts, notably abundant amphibole.

SGT1 Ashflow unit (BWSGT-296A)

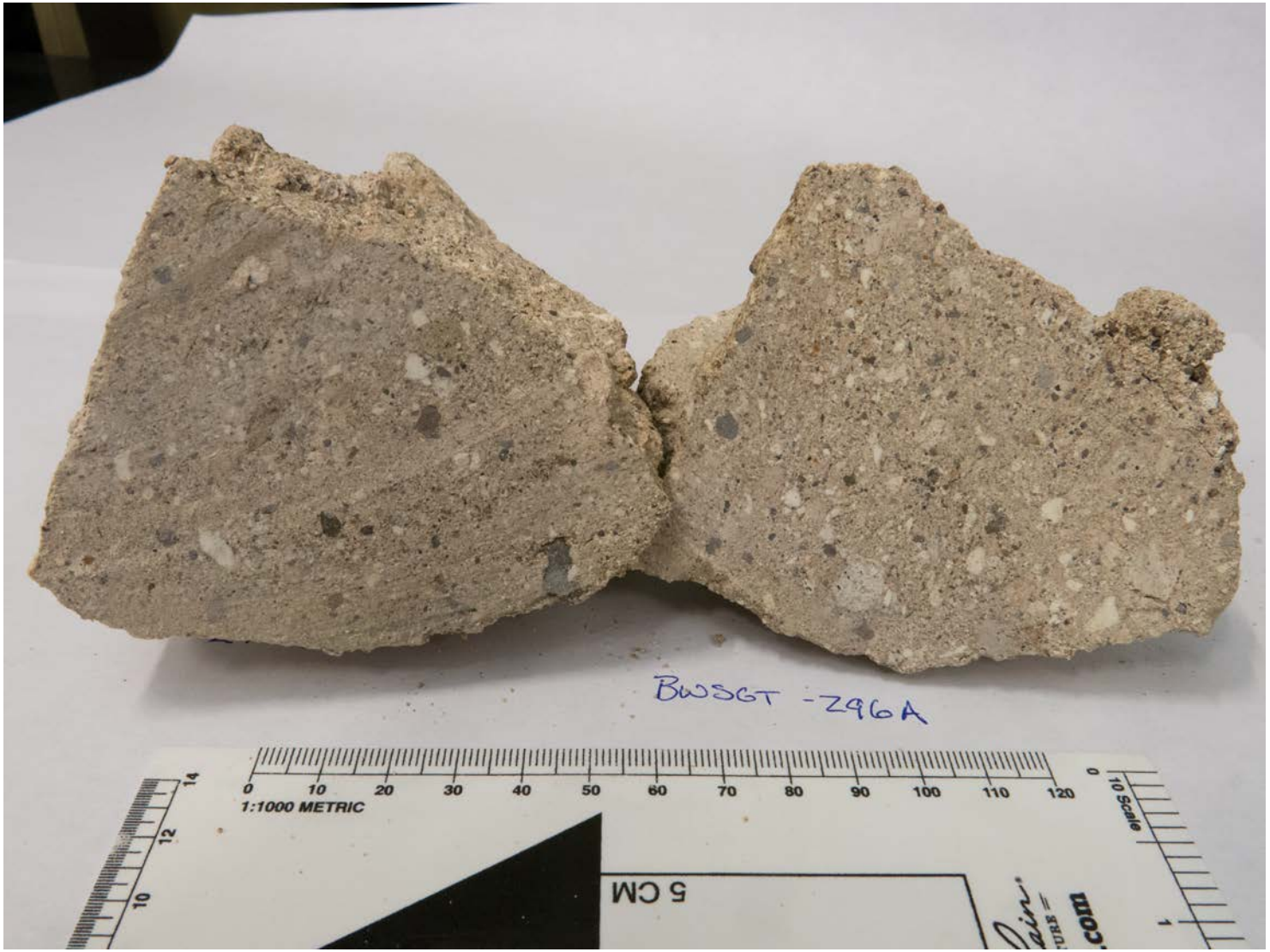

Sample of the ash flow unit at the top of SGT1

SGT2 Base (BWSGT-296B)

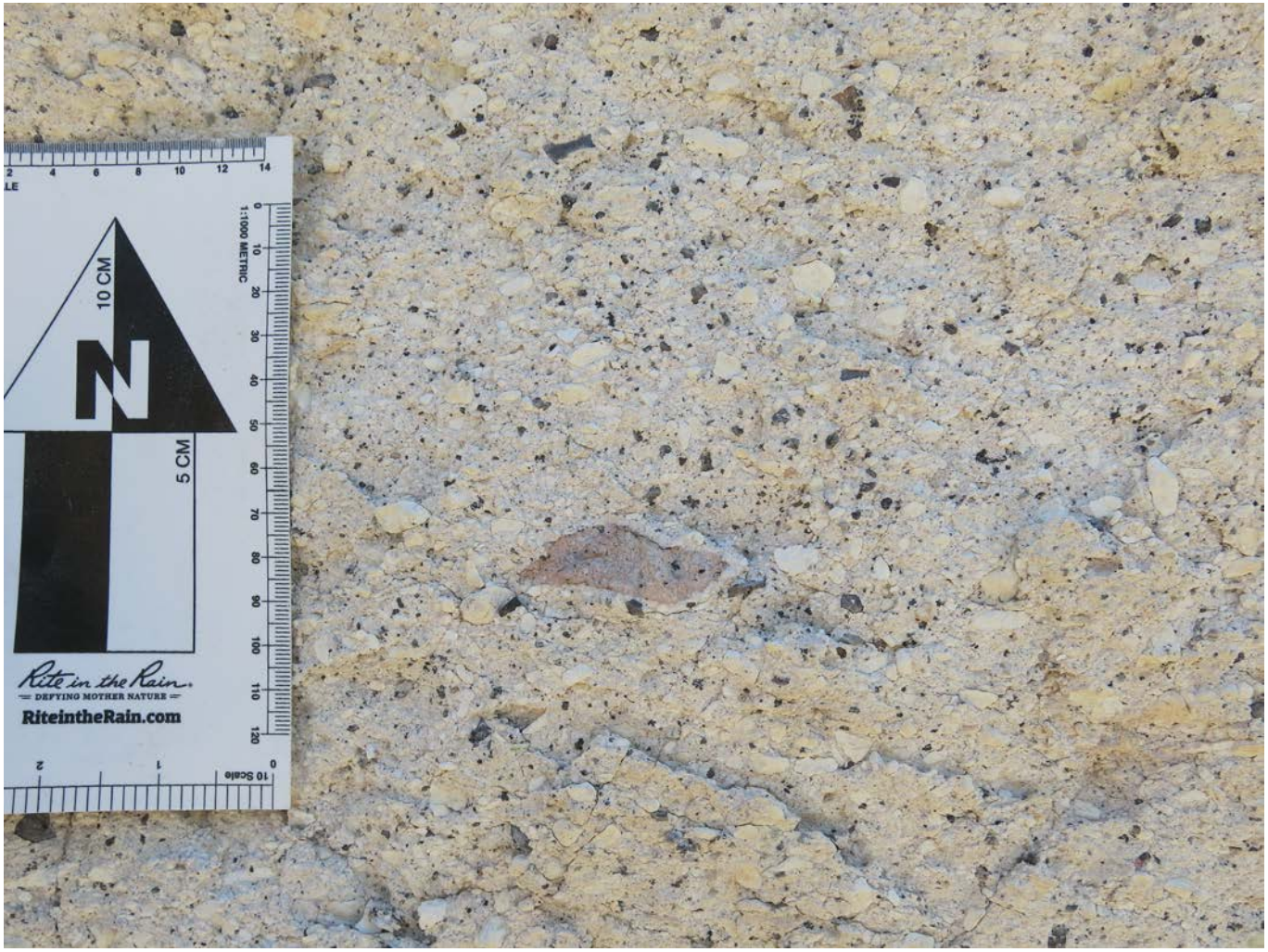

Pumice rich tuff with pea sized lithic fragments. The pumice within this unit are clearly different in hand sample from the ashflow unit. They contain <2% phenocrysts and almost no mafic phase (occasional amphibole).

SGT2 Base (BWSGT-296B)

Pumice rich tuff with pea sized lithic fragments. The pumice within this unit are clearly different in hand sample from the ashflow unit. They contain <2% phenocrysts and almost no mafic phase (occasional amphibole). Red arrow points to large rounded quartz phenocryst.

BWSGT-296B

Sample of the lowest unit within SGT2. Notice the low abundance of phenocrysts (mainly qtz and san) within pumice. Also worth noting is that this is the first appearance of spherulitic rhyolite lithic fragments, which are the dominant lithic fragment within the SGT2 unit.

Complex layering

Outcrop is ~10 m above the base of SGT2, shows complex grading and multiple units within close succession.

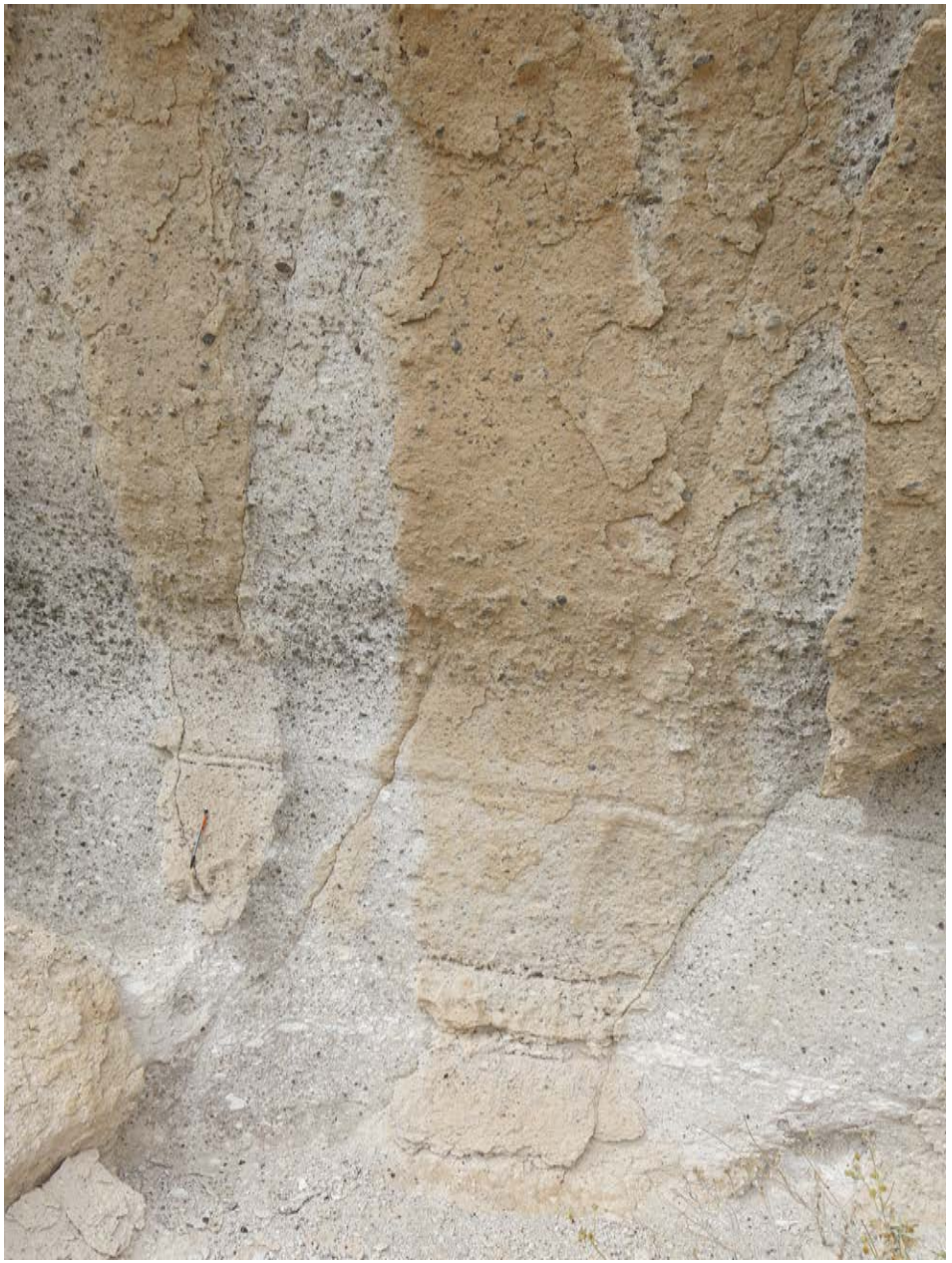

Lithic tuff within SGT2

This is an image from within the large cliff forming SGT2 unit. This is what the average tuff looks like within this section. Our interpretation is that it was emplaced as a pyroclastic flow sheet due to the poor sorting of pumice and lithic fragments. On a larger scale (meters) there is commonly grading within the lithic fragments in the tuff here.

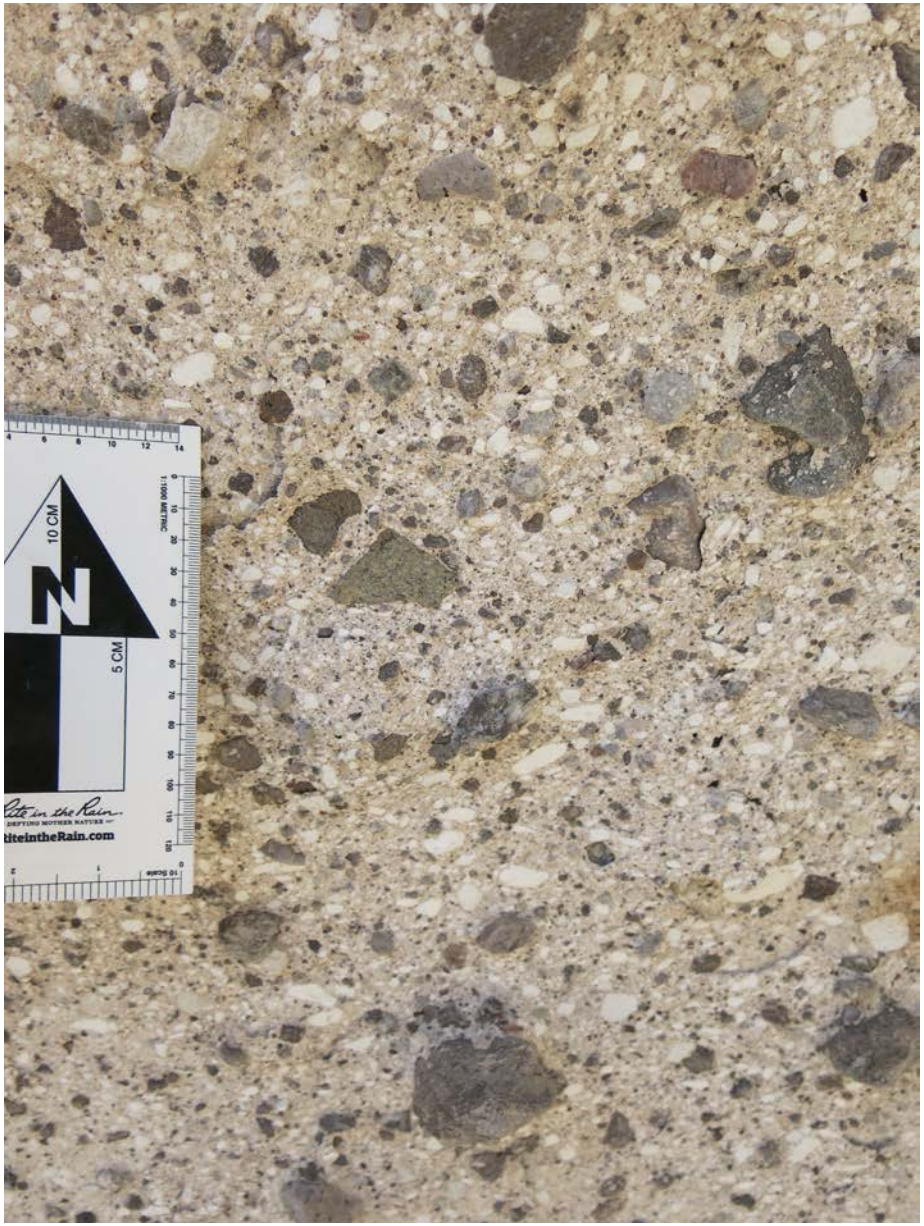

BWSGT-284A

BWSGT-333

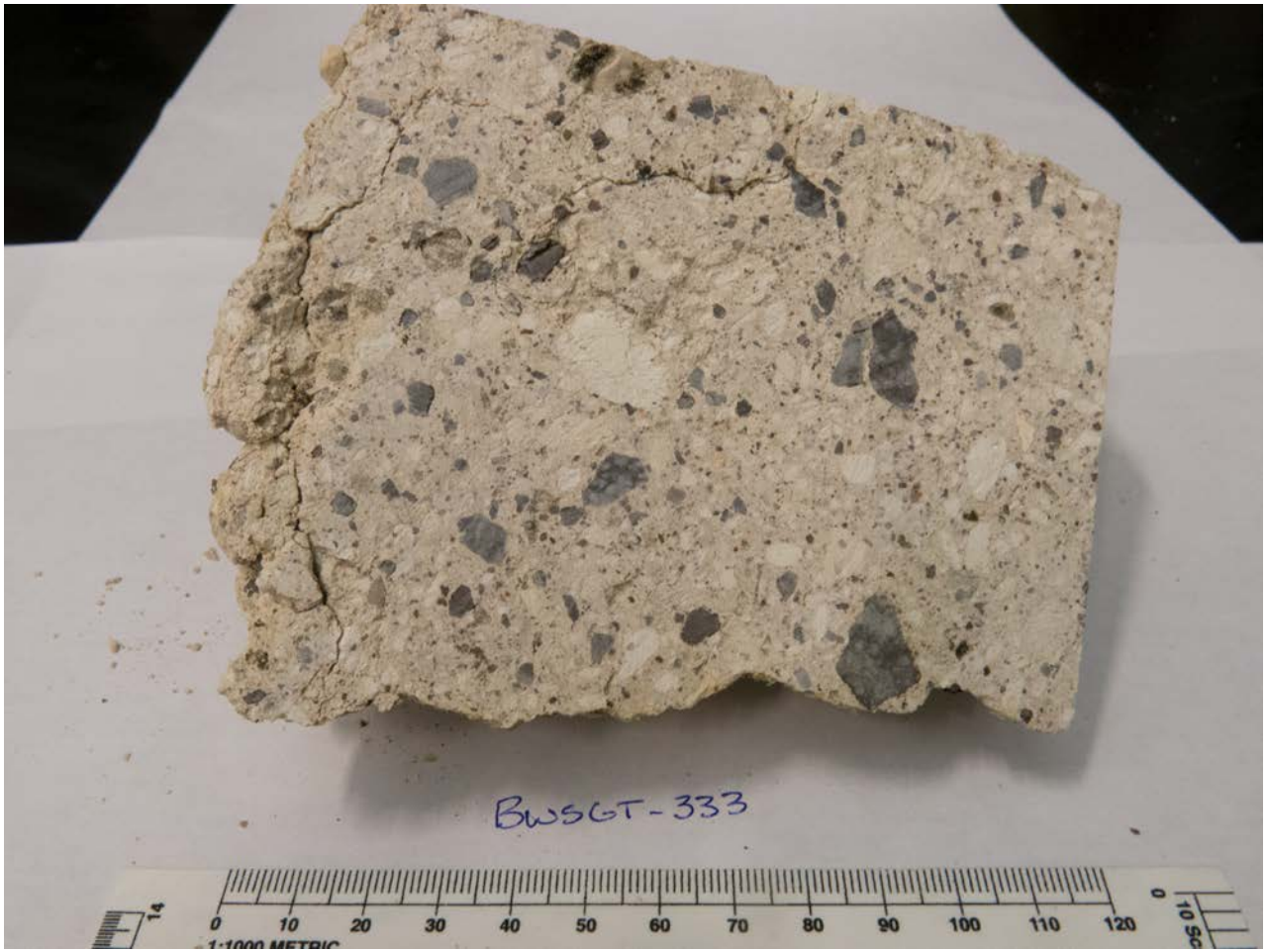

BWSGT-332

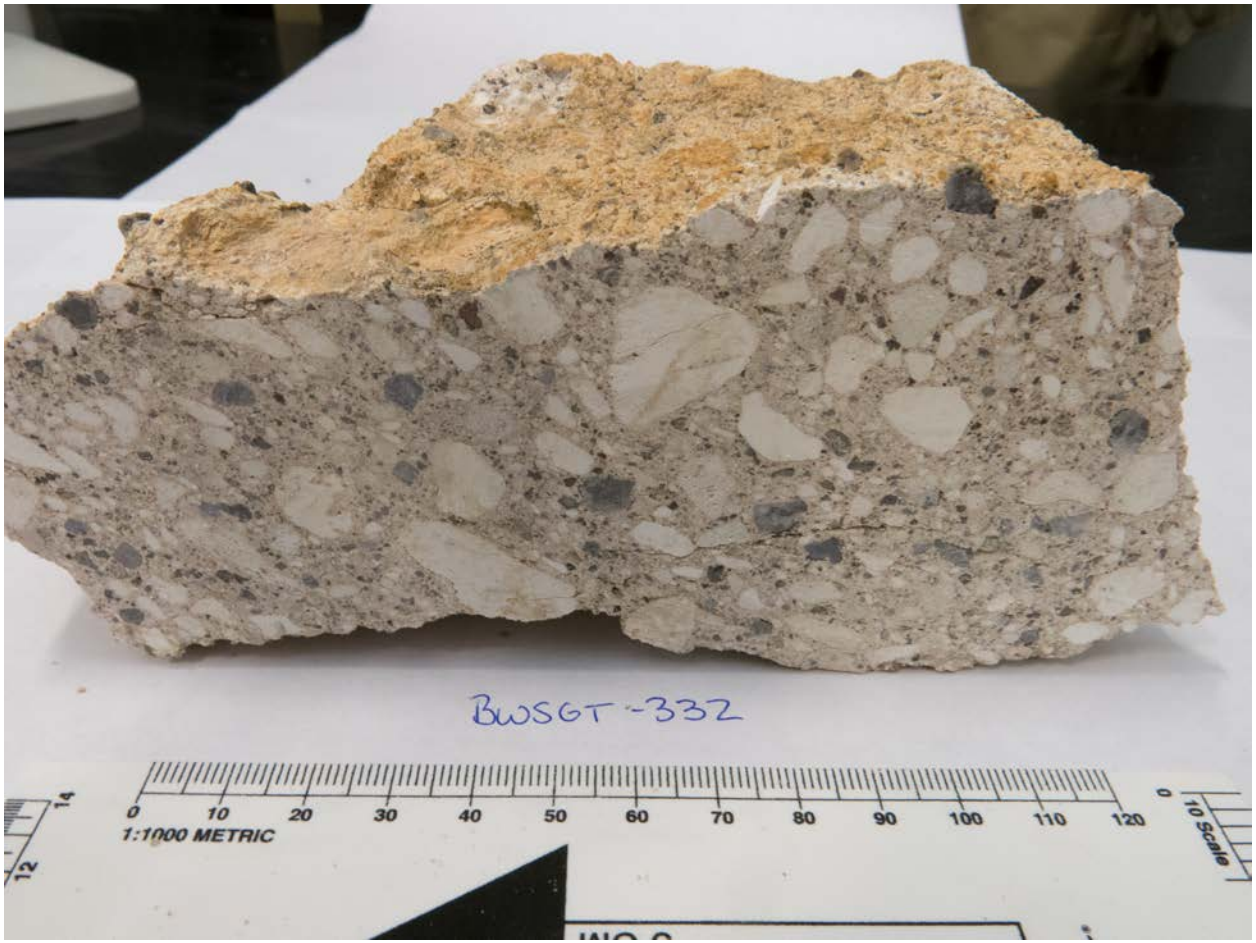
BWSGT-332
0 10 20 30 40 50 60 70 80 90 100 110 120
1:1000 METRIC
10 Scale

Megablock horizon within SGT2

Angular blocks up to 3 m in diameter are concentrated within the “megablock” horizon at about the middle of SGT2. (approx. 110 m above the base of the SGT section in Meadow Creek Basin).

Megablock horizon within SGT2

Angular blocks up to 3 m in diameter are concentrated within the “megablock” horizon at about the middle of SGT2. (approx. 110 m above the base of the SGT section in Meadow Creek Basin).

Upper Airfall Sequence within SGT2

Sample names and horizons are listed on the figure to the right.

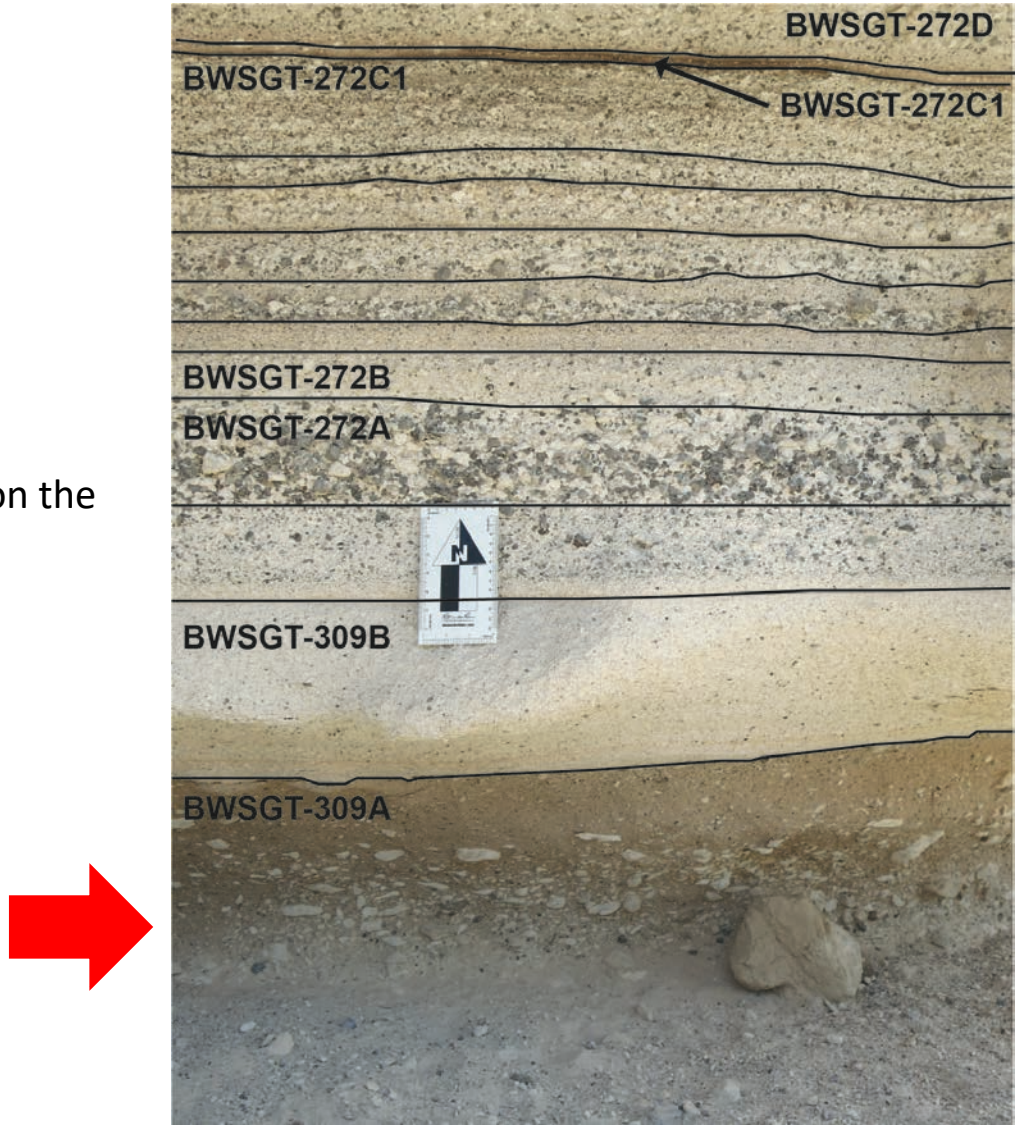

BWSGT-309A


BWSGT-309A
0 10 20 30 40 50 60 70 80 90 100 110 120
1:1000 METRIC
10 Scale

Additional picture of the ash flow unit

Note the abundance of pumice decreases moving upward through this unit and lithic fragments are concentrated toward the base.

Additional picture of the ashflow unit

Note the abundance of pumice decreases moving upward through this unit.

Additional picture of the ashflow unit

Intercalated pumice suggest the flow direction was left to right (from this perspective).

Upper fall Sequence within SGT2

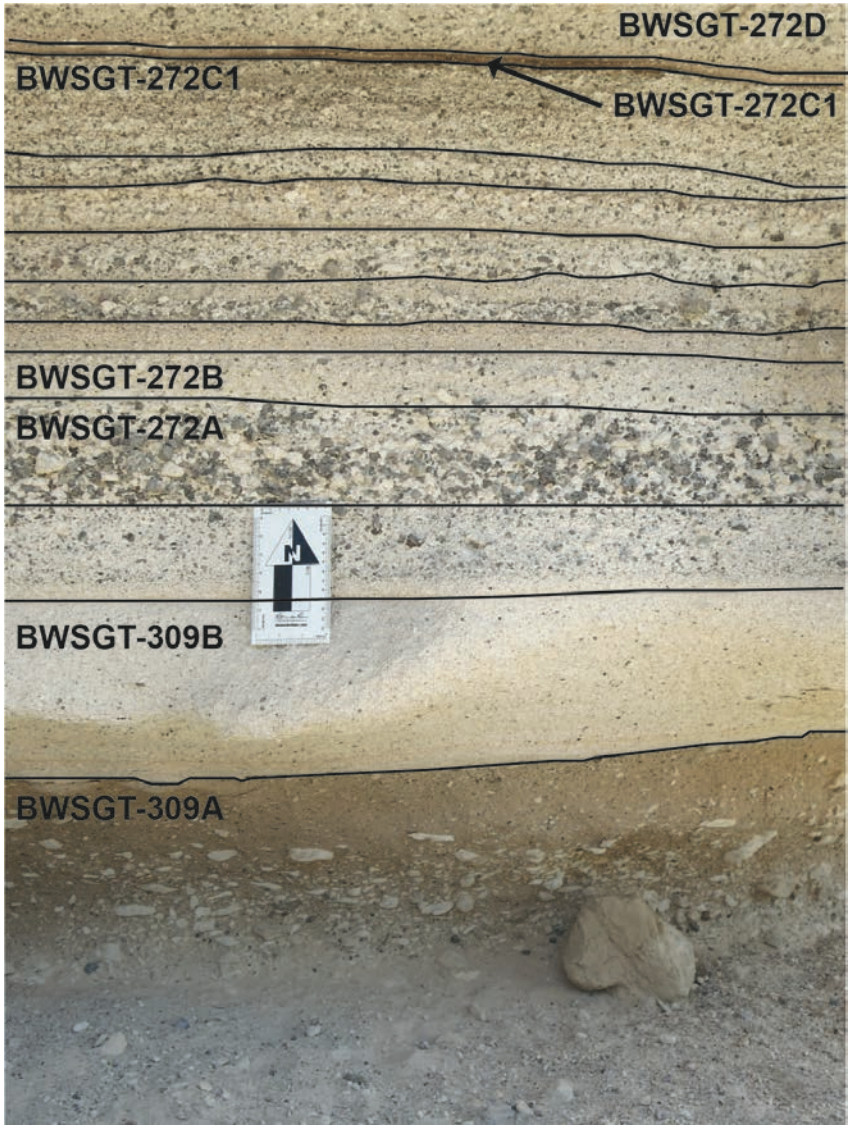

BWSGT-309B

Upper fall Sequence within SGT2

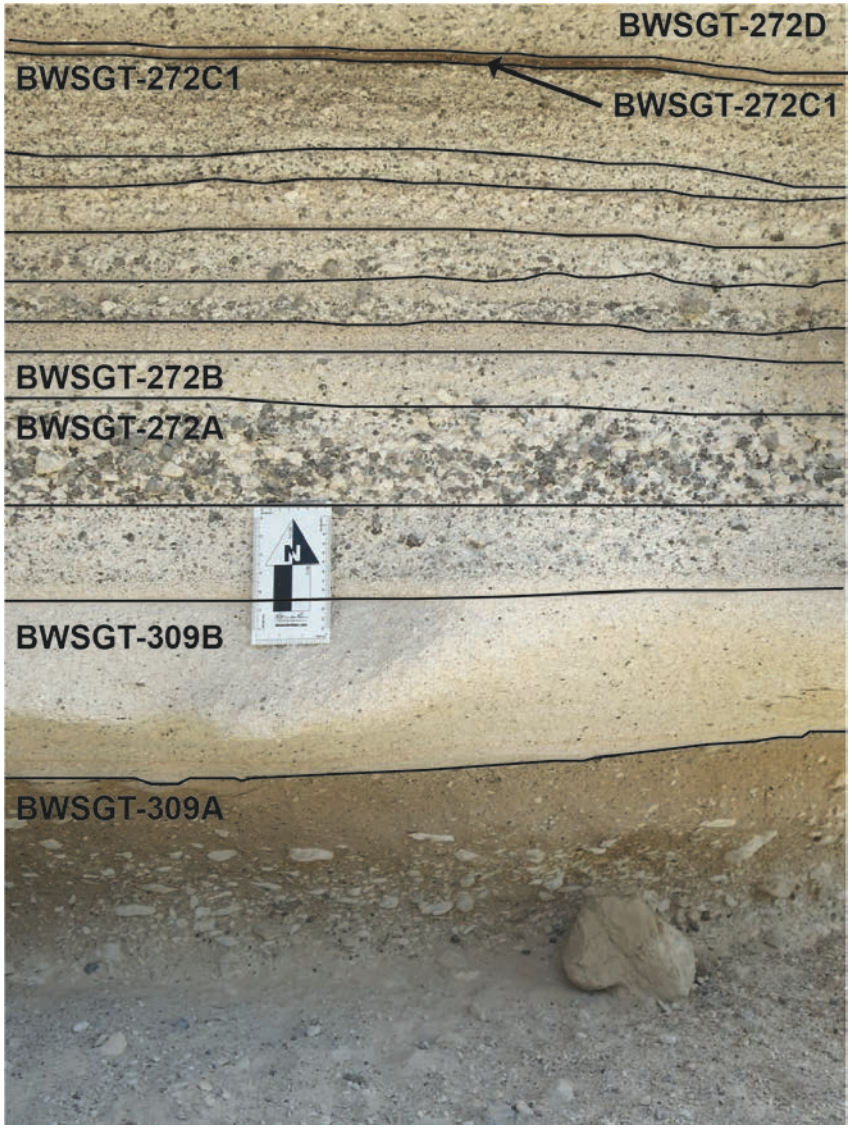

Zoomed in picture of a unit within the upper fall sequence

Clast supported fall deposit within the upper airfall sequence. Notice the grading (reverse within the unit just below the clast supported unit?)

Upper fall Sequence within SGT2

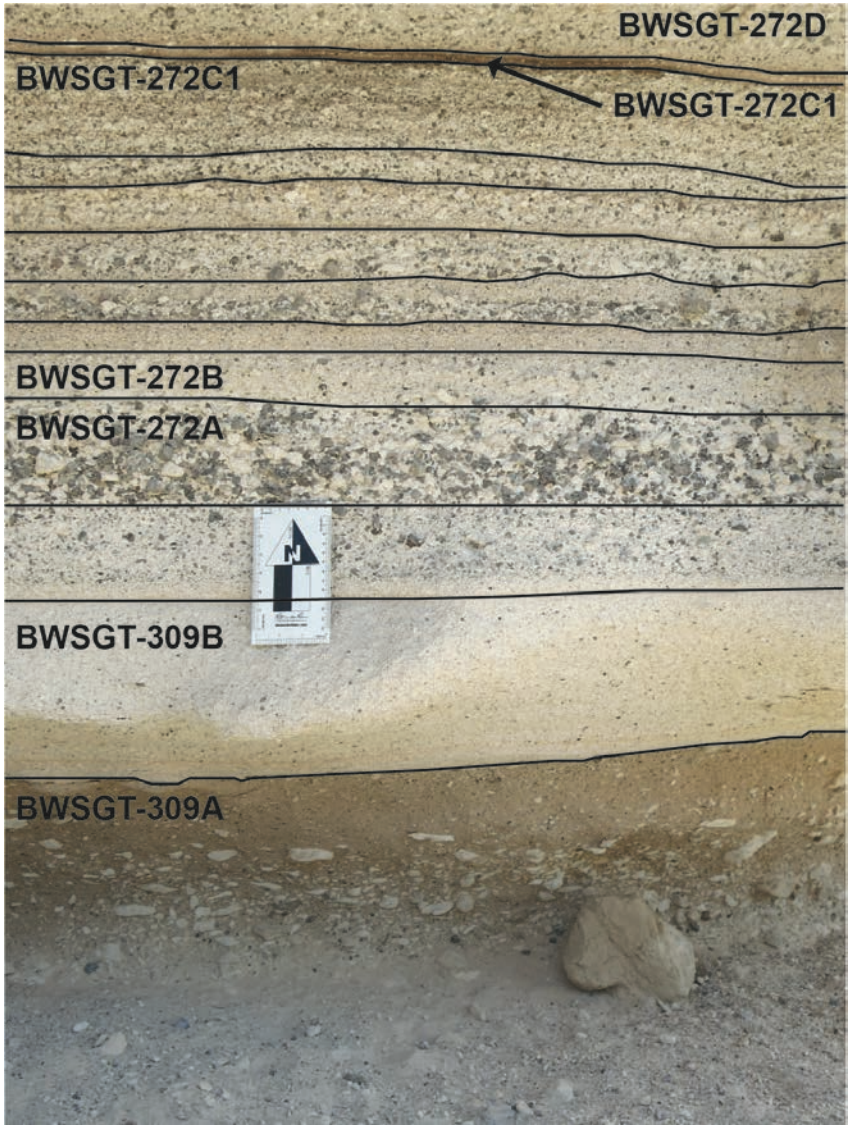

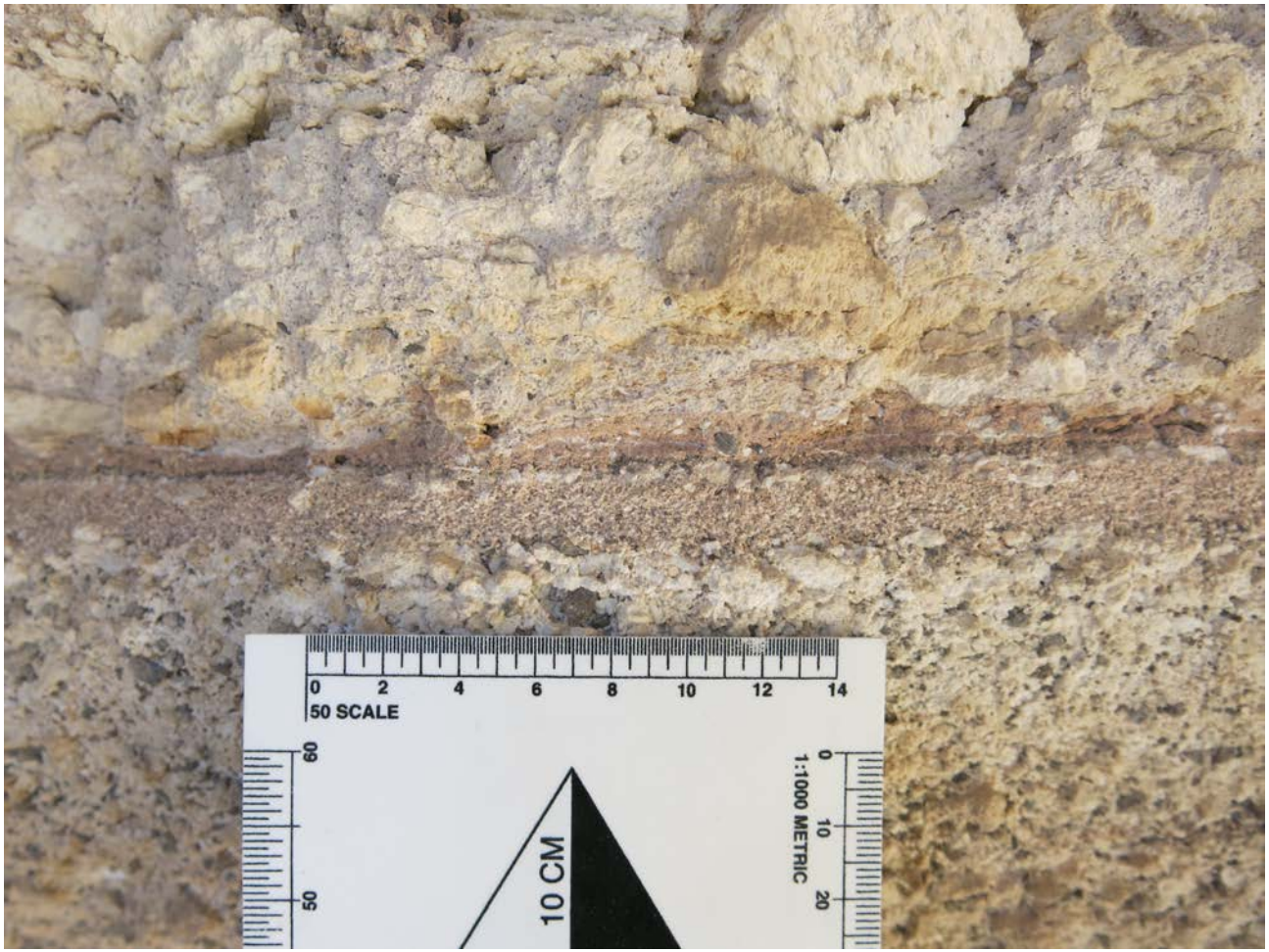

Possible paleosol at the top of the upper fall sequence

Upper Airfall Sequence within SGT2

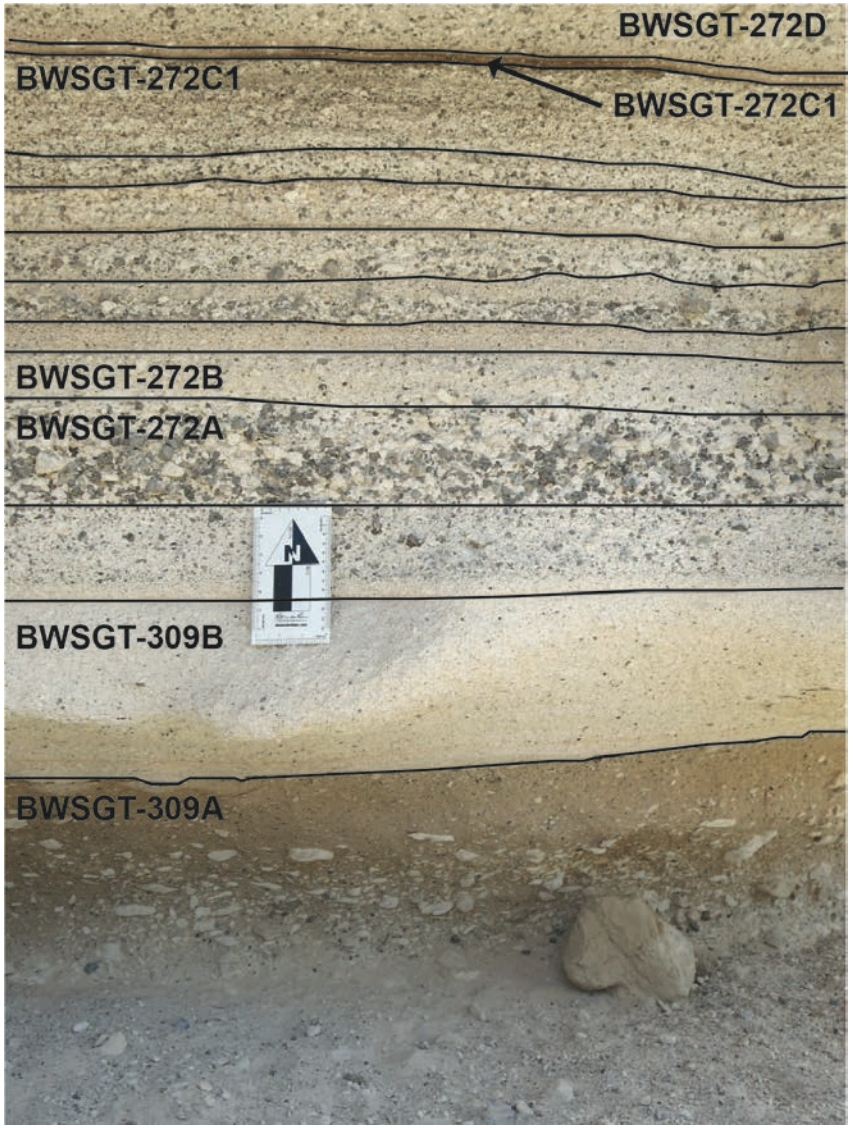

BWSGT-272D

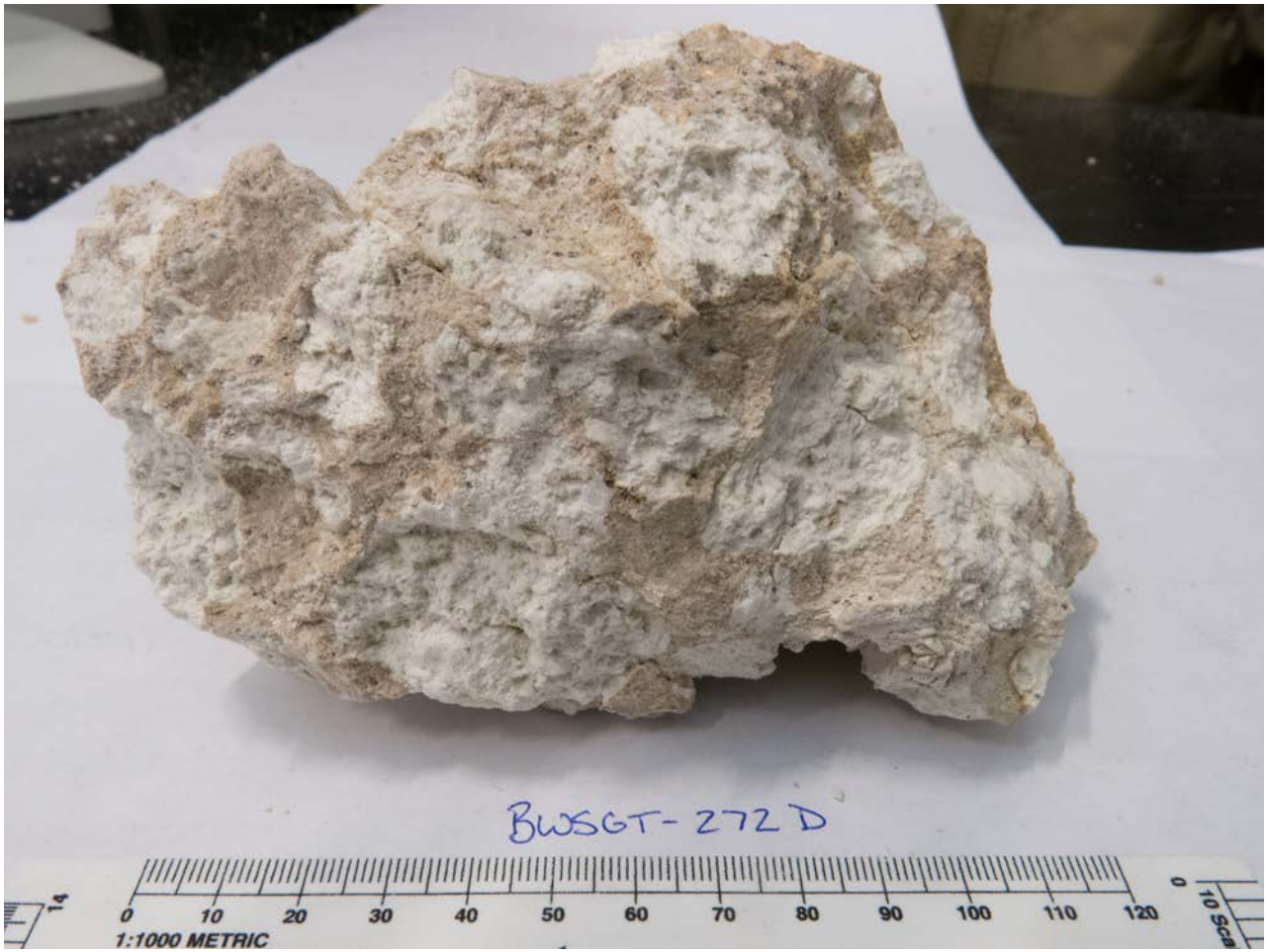

BWSGT-271B

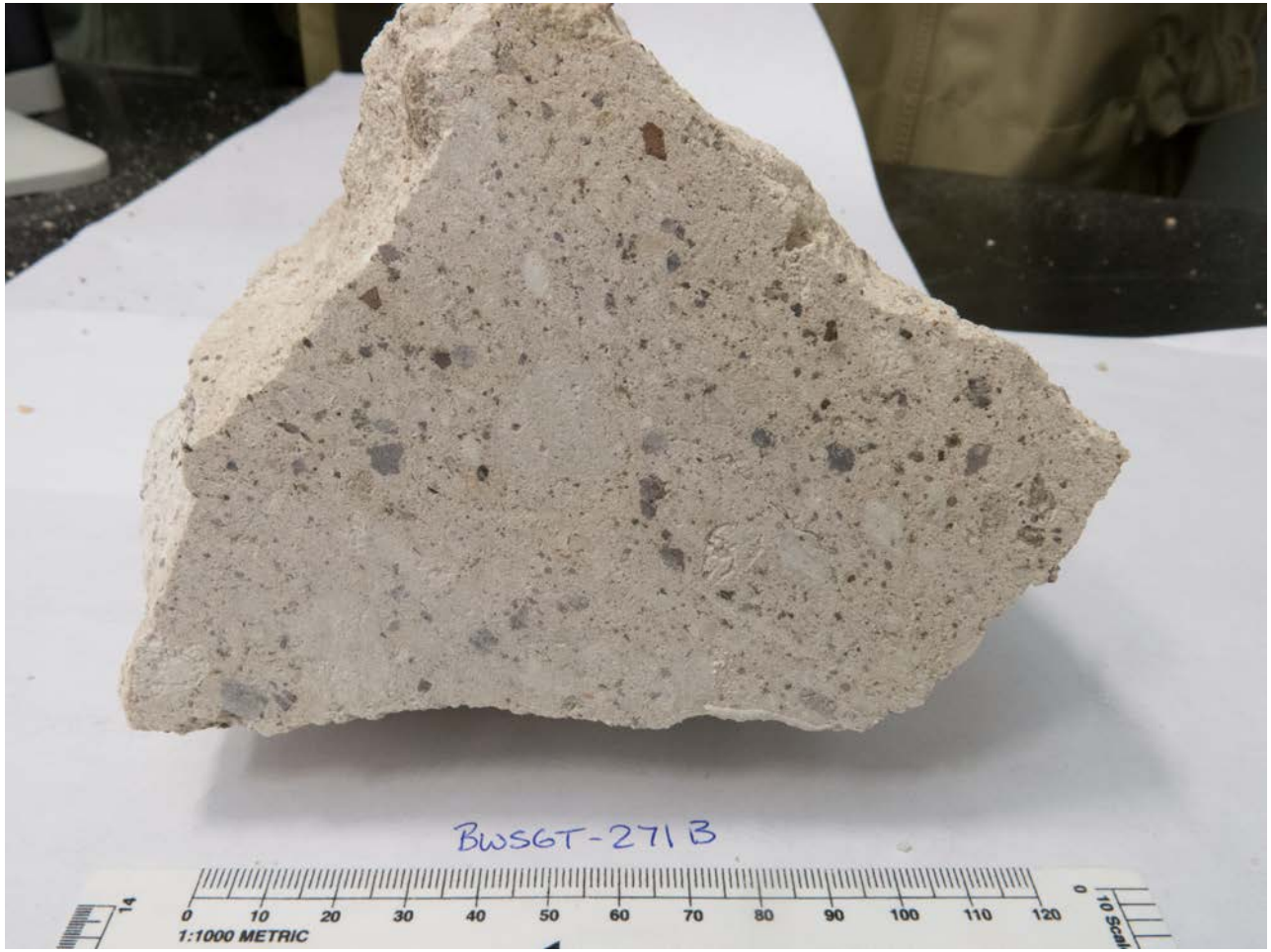

Pumicious lithic at 271B outcrop

BWSGT-307

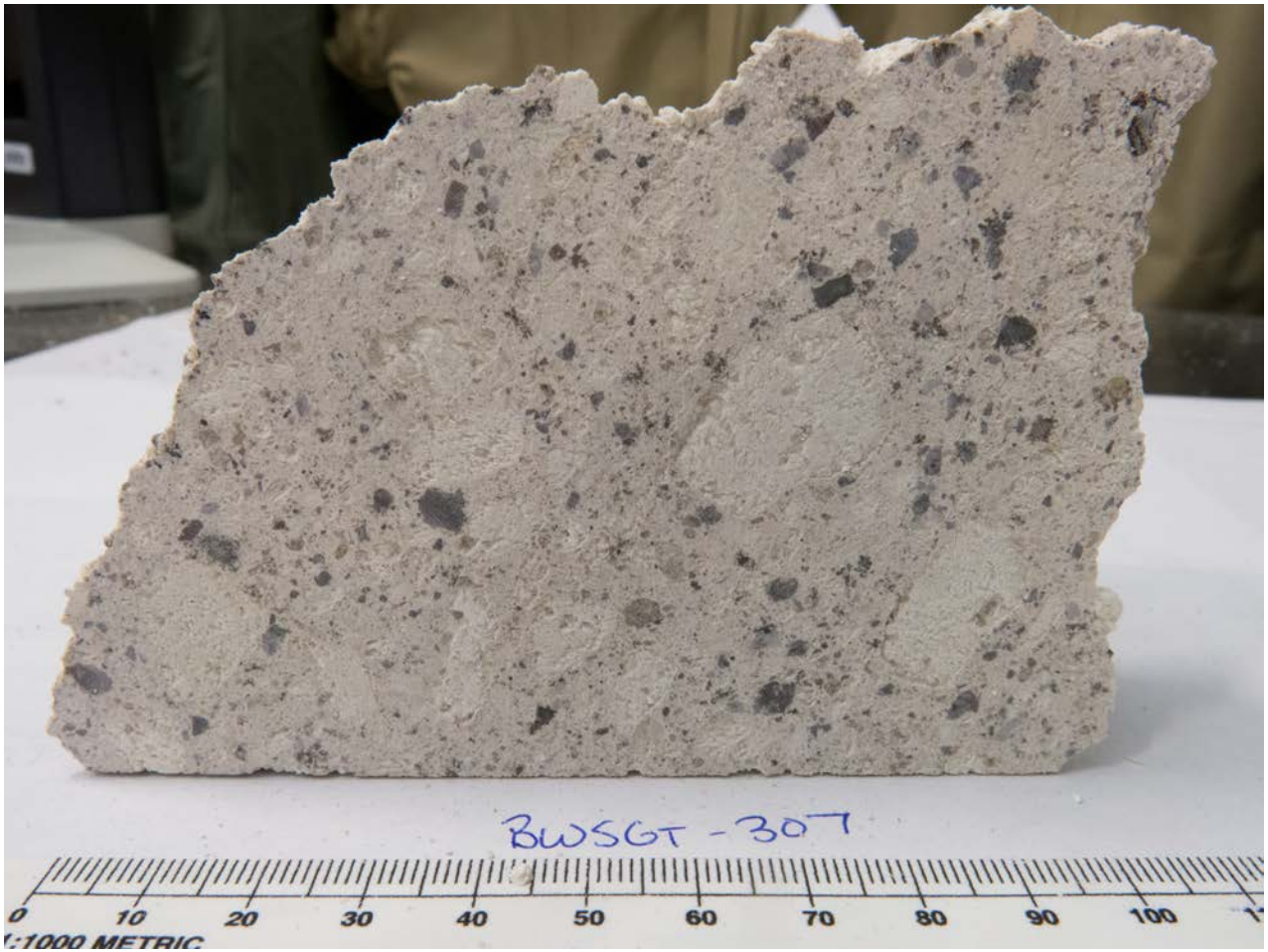

BWSGT-331

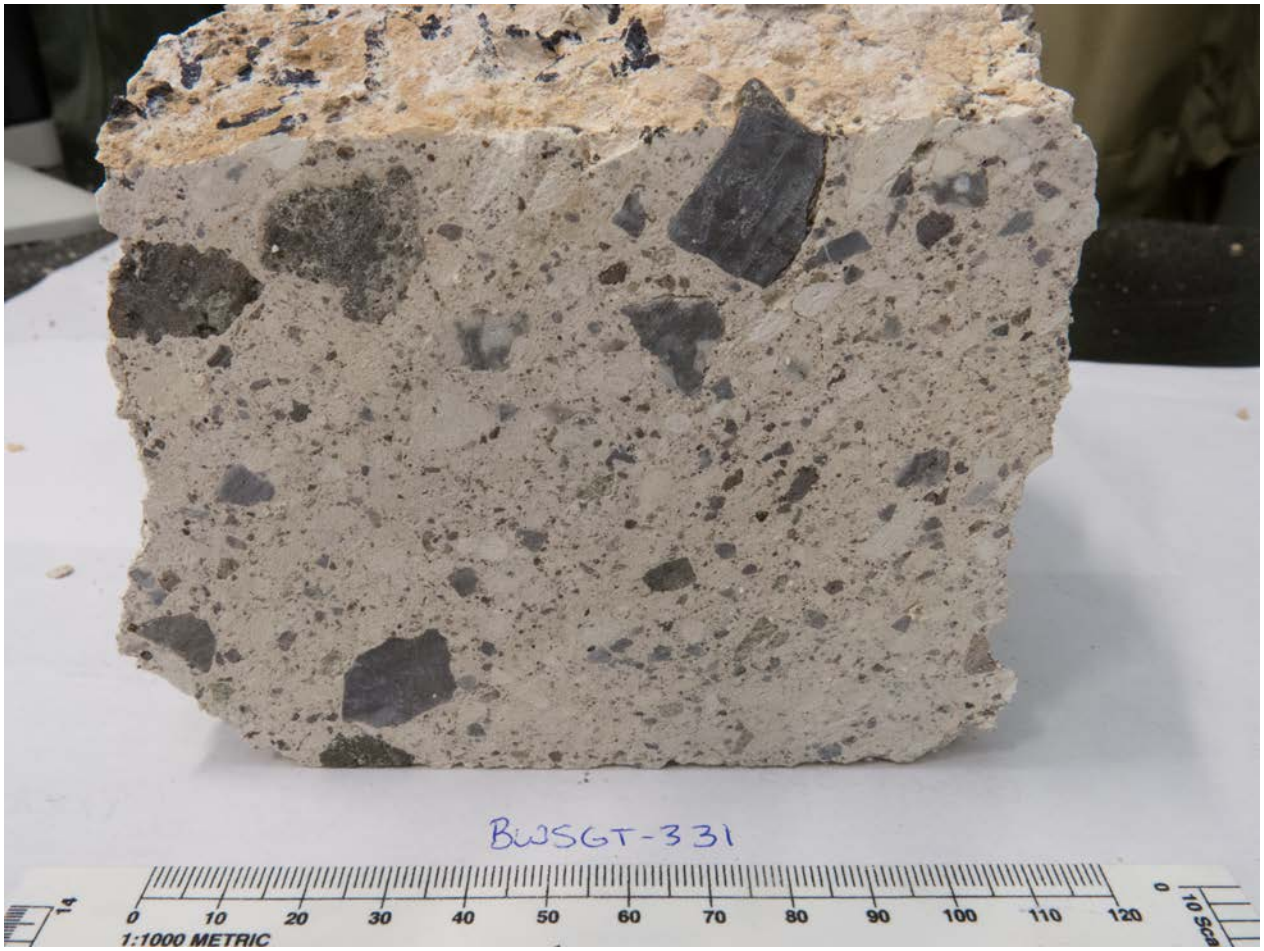

Lithic Fragments from SGT2

Spherulitic rhyolite

Flow banded rhyolite

Amphibole bearing rhyolite

Vesiculated basalt? Composition unknown

Lithic Fragments from SGT2

Perlitic green obsidian with flow banded edges.

Perlitic green obsidian. This is very common in SGT2 and is chemically identical to the pumice glass (phase assemblage is the same as well)

Lithic Fragments from SGT2

Perlitic green obsidian (rind) with fresh black perlitic glass center.

Perlitic black obsidian. Chemically identical to the pumice glass (phase assemblage is the same as well)

Cottonwood lava #3 (dome or flow?)

Chemical similarities to SGT1 (cool-wet signature in REES, titanite saturated)

Dodger peak outcrops

SGT airfall deposit? Seems like it could be very similar to the lower airfall sequence.

Some of the horizons contained ripple marks (wind or water generated?)

Gold Road Latite

Gold road latite outcrop along route 66 within Meadow Creek Basin. This is the basal (or top) breccia within the lava flow.

Meadow Creek Trachyte

Megacryst within the Meadow Creek Trachyte within Grapevine Canyon.

Meadow Creek Trachyte

Megacryst and magma mingling within the Meadow Creek Trachyte within Meadow Creek Basin.

Antelope Lava

Arrow points at the Antelope lava “hat”. This is the pumicious flow top of a silicic lava ~18.5 Ma (McDowell et al. 2016)

Antelope Lava

(Left) overview of the exposure of the Antelope lava below the Sitgreaves Tuff. (Right) Close up of the antelope lava (light gray color) and a mafic magmatic enclave (dark gray color). Hammer for scale.

Overlying basalt

In this picture the overlying tholeiitic basalt is in contact with SGT3 (reworked volcaniclastic sediments), also known as the conglomerate of Sitgreaves Pass (Ferguson et al. Mt Nutt geologic quad.)

Lag Breccia horizons

Cross cutting relations

Cross cutting relations between the trachyandesite dike and the SGT. Note the unusual kink to the left at the arrow

Cross cutting relations

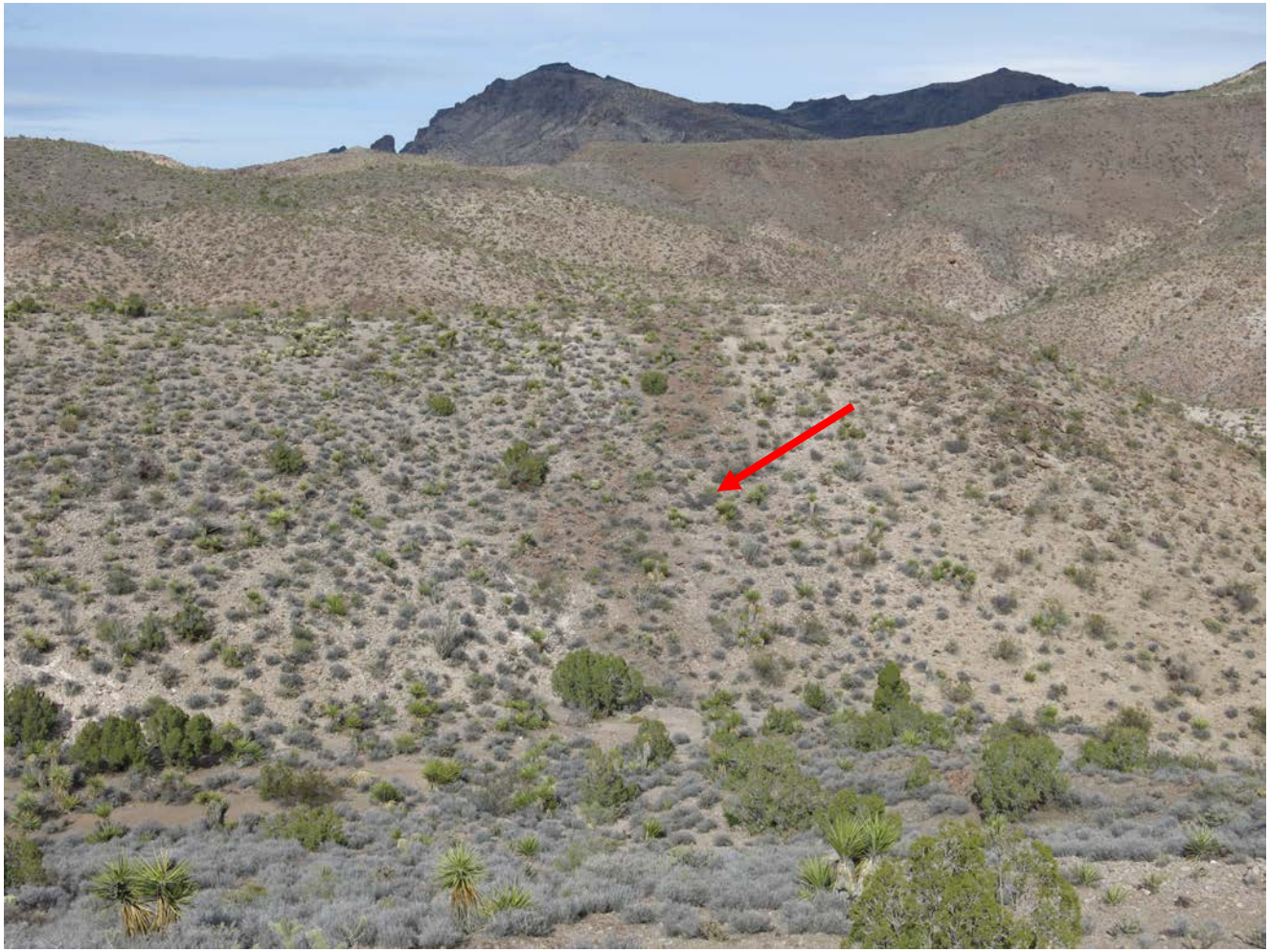

Cross cutting relations between the trachyandesite dike and the Meadow Creek Trachyte.

APPENDIX E

Thin Section Tables for the Sitgreaves Tuff and Cottonwood Lavas:

Sample #	Location (Easting, Northing, Zone) NAD83	Location (Degrees, Decimal	Unit Name	Descriptive Location	Major Phenocrysts	Accessory Minerals	Phenocryst %
BWSGT-295B	742492.25 m E 3880932.97 m N 11S	35° 7'56.13"N 114°23'18.47"W	SGT1	Pyroclastic flow blanketing a fall deposit (BWSGT-295A) and the Antelope lava. At the base of the section within Meadowcreek Basin	Plag> Kspar> Bt> Amp>Qtz>mag> cpx (rare)	Ttn, Zrn, Monazite, apatite	20-25%
BWSGT-296A	742516.77 m E 3881009.78 m N 11S	35° 2'33.69"N 114°20'28.59"W	SGT1	Ash flow at the base of the SGT2 cliff forming unit. Sample was taken approximately 14 m above the base where sample (295A was collected).	Plag> Kspar> Bt> Amp>Qtz>mag	Ttn, Zrn, apatite	20-25%
BWSGT-296B	742516.77 m E 3881009.78 m N 11S	35° 2'33.69"N 114°20'28.59"W	SGT2	Just above (~.25 m) where sample BWSGT-296A was collected. Unit is composed of pumicious tuff (pyroclastic flow deposit).	Kspar > Qtz> Amp >Mag	Ttn, Zrn, apatite	<5%
BWSGT-284A	742869.00 m E 3881072.03 m N 11S	35° 2'35.41"N 114°20'14.64"W	SGT2	In the first canyon to the west the diabase lopolith.	Kspar > Qtz > Amp >Mag	Ttn, Zrn, apatite	<5%
BWSGT-333	742202.56 m E 3881237.54 m N	35° 2'41.33"N 114°20'40.77"W	SGT2	~ 12 m below the megablock horizon within the canyon	Kspar > Qtz > Amp >Mag	Ttn, Zrn, apatite	<5%

	11S			within the canyon.			
BWSGT-332A	742174.45 m E 3881238.67 m N 11S	35° 2'41.39"N 114°20'41.87"W 11S	SGT2	Top of the megablock horizon	Kspar > Qtz > Amp >Mag	Ttn, Zrn, apatite	<5%
BWSGT-309A	741325.67 m E 3881569.59 m N 11S	35° 2'52.86"N 114°21'15.00"W	SGT2	At the upper airfall deposit within SGT2. This sample was collected from the ash flow at the base of the airfall sequence.	Kspar > Qtz > Amp >Mag	Ttn, Zrn, apatite	<5%
BWSGT-309B	741325.67 m E 3881569.59 m N 11S	35° 2'52.86"N 114°21'15.00"W	SGT2	At the upper airfall deposit within SGT2. This sample was collected from the lapelli rich unit just above the base of the airfall sequence.	Kspar > Qtz > Amp >Mag	Ttn, Zrn, apatite	<5%
BWSGT-307	741964.75 m E 3881315.47 m N 11S	35° 2'44.07"N 114°20'50.07"W	SGT2	Just above (first unit, ~ 5 cm) the upper airfall sequence within SGT2. Correlates with BWSGT-272D. From the same horizon but 1 canyon to the west.	Kspar > Qtz > Amp >Mag	Ttn, Zrn, apatite	<5%
BWSGT-271B	741235.13 m E 3881589.28 m N 11S	35° 2'53.58"N 114°21'18.53"W	SGT2	Highest outcrop exposure within MCB, along the powerline road	Kspar > Qtz > Amp >Mag	Ttn, Zrn, apatite	<5%

BWSGT-284B	742869.00 m E 3881072.03 m N 11S	35° 2'35.41"N 114°20'14.64"W	SGT2	In the first canyon to the west the diabase lopolith.	Kspar > Qtz > Amp >Mag	Ttn, Zrn, apatite	<5%
BWSGT-295A	742492.25 m E 3880932.97 m N 11S	35° 7'56.13"N 114°23'18.47"W	SGT1	fall deposit (directly below BWSGT-295B) overlying the Antelope lava. At the base of the section within Meadowcreek Basin	Plag >Kspar > bt > amp > Qtz >Mag > cpx (rare)	Ttn, Zrn, Monazite, apatite	20-25%
BWSGT-384A	741540.30 m E 3881056.14 m N 11S	35° 2'36.04"N 114°21'7.06"W	SGT1	Just to the East of the dike waterfall. At the bottom of the SGT section. Just north of the lower powerline road. Base of outcrop.	Plag > Kspar >Qtz > Bt > Amp	Ttn, Zrn, apatite	20-25%
BWSGT-384B	741540.30 m E 3881056.14 m N 11S	35° 2'36.04"N 114°21'7.06"W	SGT1	Just to the East of the dike waterfall. At the bottom of the SGT section. Just north of the lower powerline road. ~3 m above the base where 384A was collected.	Plag > Kspar >Qtz > Bt > Amp	Ttn, Zrn, apatite	20-25%
LS-111	742361.35 m E 3881116.20 m N 11S	35° 2'37.28"N 114°20'34.61"W	SGT2	Lunch spot from winter REU. ~10 m up the cliff forming SGT2.	Plag > Kspar >Qtz > Bt > Amp	Ttn, Zrn, apatite	<5%

BWSGT-113	742174.19 m E 3881237.94 m N 11S	35° 2'41.36"N 114°20'41.87"W	SGT2	Within Indian Spring Canyon (NW side), at the megablock horizon.	Plag > Kspar >Qtz > Bt > Amp	Ttn, Zrn, apatite	<5%
BWSGT-272D	741321.08 m E 3881573.00 m N 11S	35° 2'52.99"N 114°21'15.15"W	SGT2	Just above (first unit, ~ 5 cm) the upper airfall sequence within SGT2. Correlates with BWSGT-307. From the same horizon but 1 canyon to the west.	Plag > Kspar >Qtz > Bt > Amp	Ttn, Zrn, apatite	<5%
CLW-1	744151.47 m E 3881985.15 m N 11S	35° 3.065'N 114° 19.385'W	Cotton wood Lava #3	Hidden Valley Wash, North of the gun guys house	Kspar> Qtz>Plag> Bt> Amp	Mag, Ttn, Chevkinite, Zrn	25-35%
CLW-2	744236.97 m E 3881975.83 m N 11S	35° 3.058'N 114° 19.328'W	Cotton wood Lava #3	Hidden Valley Wash, North of the gun guys house	Kspar> Qtz>Plag> Bt> Amp	Mag, Ttn, Chevkinite, Zrn	25-35%
CLW-3	744239.75 m E 3881971.34 m N 11S	35° 3.056'N 114° 19.328'W	Cotton wood Lava #3	Hidden Valley Wash, North of the gun guys house	Kspar> Qtz>Plag> Bt> Amp	Mag, Ttn, Chevkinite, Zrn	25-35%
CLW-4	744129.00 m E 3881772.00 m N 11S	35° 2.950'N 114° 19.404'W	Cotton wood Lava #3	Hidden Valley Wash, North of the gun guys house	Kspar> Qtz>Plag> Bt> Amp	Mag, Ttn, Chevkinite, Zrn	25-35%
CLW-5	744129.00 m E 3881772.00 m N 11S	35° 2.950'N 114° 19.404'W	Cotton wood Lava #3	Hidden Valley Wash, North of the gun guys house	Kspar> Qtz>Plag> Bt> Amp	Mag, Ttn, Chevkinite, Zrn	25-35%
CLW-6	741159.52 m E 3883796.71 m N 11S	35° 4.087'N 114° 21.320'W	Cotton wood Lava #6	North of Sitgreaves Pass and East of Battleship Mtn within a spur drainage of Cottonwood Canyon	Kspar> Qtz>Plag> Bt> Amp	Magnetite, Sphene, Chevkinite, Zircon	25-35%

APPENDIX F

Average glass data for post-supereruption silicic lavas and tuffs.

Data for ALHS19 is from Schlaerth et al. 2016.

Sample	BWSGT-309B	BWSGT-284A	BWSGT-307	BWSGT-271	BWSGT-272D	BWSGT-381
Unit	SGT2	SGT2	SGT2	SGT2	SGT2	SGT2
Na	20494.09	25852.18	19379.96	23319.32	21686.87	18854.54
Mg	378.18	451.89	527.61	277.89	230.51	480.72
Al	71890.53	69233.16	69865.84	64003.12	62352.32	64582.71
Si	362265.46	360863.16	361798.02	362265.46	358600.78	361798.03
P	47.88	47.16	52.15	47.75	36.91	60.05
K	55073.76	50885.12	56633.16	51228.98	48947.46	60272.19
Ca	2426.88	2292.67	2705.93	2033.09	2185.19	2342.00
Sc	10.41	10.39	9.99	10.30	5.53	11.24
Ti	516.32	569.63	484.82	495.11	434.87	453.67
V	0.45	0.24	0.52	0.28	0.26	0.24
Mn	735.02	738.08	864.17	703.49	684.39	–
Co	0.29	0.12	0.79	0.18	0.32	–
Ni	0.26	0.35	0.53	0.43	0.73	0.30
Cu	5.12	8.73	3.83	4.76	0.77	–
Zn	61.24	69.19	31.88	58.78	61.90	–
Ga	20.85	20.36	20.20	18.95	19.94	–
Ge	1.67	1.76	1.54	1.48	1.73	–
Rb	332.71	237.85	474.98	240.19	242.80	396.54
Sr	1.44	0.64	2.11	1.04	0.45	3.51
Y	23.45	26.75	23.91	22.05	22.67	23.20
Zr	107.76	108.72	107.82	99.79	113.74	117.34
Nb	52.68	53.69	49.77	49.84	46.13	47.86
Cs	3.91	3.77	3.63	3.67	3.55	#N/A
Ba	2.03	1.18	2.53	2.26	0.46	1.82
La	26.80	28.97	27.09	25.42	29.22	29.64
Ce	53.00	58.25	52.13	48.69	50.24	51.44
Pr	4.28	4.94	4.06	3.92	4.13	4.18
Nd	10.75	12.39	10.32	10.09	10.37	10.49
Sm	1.65	2.31	1.59	1.69	1.75	1.83
Eu	0.04	0.04	0.03	0.03	0.04	0.04
Gd	1.74	2.40	1.78	1.60	1.66	1.76
Tb	0.33	0.44	0.37	0.33	0.36	0.36
Dy	2.87	3.43	2.59	2.53	2.68	2.59
Ho	0.65	0.81	0.64	0.61	0.64	0.65
Er	2.34	2.67	2.26	2.13	2.14	2.21
Tm	0.42	0.45	0.42	0.38	0.38	0.37
Yb	2.96	3.16	2.94	2.84	2.95	2.96
Lu	0.48	0.48	0.48	0.40	0.43	0.45
Hf	5.77	5.58	6.04	5.42	5.64	5.80
Ta	2.97	3.05	2.91	2.87	2.24	2.30

Tl	1.24	1.12	1.41	1.08	1.05	–
Pb	47.13	45.32	56.82	43.27	41.97	46.21
Th	31.09	29.69	29.82	28.83	30.06	30.76
U	6.37	6.25	5.87	5.96	5.87	6.04

Sample	BWSGT-384A (74)	BWSGT-384A (77)	CLW-6	CLW-1	ALHS-19
Unit	SGT1 (Glass 1)	SGT1 (Glass 2)	Cottonwood #6	Cottonwood #3	Antelope Lava
Na	15976.60	15268.54	23551.33	21135.97	22273.79
Mg	1712.30	759.92	302.72	241.87	916.31
Al	67111.61	61619.02	63349.68	63121.13	70339.43
Si	347601.33	358806.49	358339.01	358292.23	356656.36
P	83.56	59.34	46.54	48.42	164.18
K	47951.69	48657.17	47822.56	48746.58	51779.83
Ca	8999.09	6006.27	2709.17	3621.08	4481.05
Sc	8.52	7.91	6.28	7.59	13.26
Ti	737.76	450.97	625.08	445.15	1117.81
V	3.99	2.33	1.52	1.18	8.07
Mn	319.47	242.38	507.40	350.34	271.02
Co	0.57	0.44	–	–	0.55
Ni	0.87	0.80	1.26	–	0.70
Cu	3.18	1.57	0.70	0.58	4.20
Zn	26.71	16.77	42.76	19.26	27.82
Ga	27.45	17.29	17.56	16.26	37.89
Ge	1.37	1.75	1.66	2.03	1.42
Rb	187.46	196.28	197.85	258.45	176.81
Sr	315.28	101.83	11.49	19.30	90.10
Y	8.61	4.13	13.63	5.53	17.59
Zr	157.63	68.64	98.58	52.23	120.23
Nb	13.50	10.32	30.01	18.29	24.80
Cs	2.56	3.02	2.66	5.32	2.61
Ba	675.33	213.56	53.60	15.91	563.29
La	55.50	23.18	34.86	22.45	45.52
Ce	94.43	32.81	59.19	32.55	91.78
Pr	9.42	2.57	5.00	2.34	8.46
Nd	31.93	7.12	14.26	5.85	26.93
Sm	4.46	0.79	1.97	0.65	4.02
Eu	0.78	0.16	0.21	0.08	0.53
Gd	2.57	0.65	1.50	0.58	3.42
Tb	0.32	0.06	0.26	0.08	0.47
Dy	1.63	0.52	1.61	0.54	2.97
Ho	0.28	0.11	0.40	0.14	0.60

Er	0.80	0.38	1.36	0.53	1.88
Tm	0.13	0.07	0.24	0.11	0.29
Yb	0.95	0.69	1.98	1.05	2.03
Lu	0.14	0.13	0.33	0.19	0.32
Hf	4.27	2.40	4.09	2.89	3.69
Ta	0.77	0.67	1.55	1.10	1.72
Tl	0.97	0.84	–	–	0.78
Pb	28.89	28.11	31.99	33.63	28.57
Th	19.50	19.86	22.66	27.85	22.72
U	3.25	4.30	4.10	7.51	4.42